Plasma Instabilities and Turbulence in Non-Abelian Gauge Theories

Vom Fachbereich Physik
der Technischen Universität Darmstadt

zur Erlangung des Grades
eines Doktors der Naturwissenschaften
(Dr. rer. nat.)

genehmigte Dissertation von
Dipl.-Phys. Sebastian Herwig Jürgen Scheffler
aus Hamburg

Darmstadt 2010
D17

Referent:	Prof. Dr. Jürgen Berges
Korreferent:	Prof. Dr. Christian Fischer

Tag der Einreichung:	26. 1. 2010
Tag der Prüfung:	17. 2. 2010

Abstract

Several aspects of the thermalisation process in non-Abelian gauge theories are investigated. Both numerical simulations in the classical statistical approximation and analytical computations in the framework of the two-particle-irreducible effective action are carried out and their results are compared to each other. The physical quantities of central importance are the correlation functions of the gauge field in Coulomb and temporal axial gauge as well as the gauge invariant energy-momentum tensor.

Following a general introduction, the theoretical framework of the ensuing investigations is outlined. In doing so, the range of validity of the employed approximation schemes is discussed as well.

The first main part of the thesis is concerned with the early stage of the thermalisation process where particular emphasis is on the *rôle* of plasma instabilities. These investigations are relevant to the phenomenological understanding of present heavy ion collision experiments. First, an ensemble of initial conditions motivated by the "colour glass condensate" is developed which captures characteristic properties of the plasma created in heavy ion collisions. Here, the strong anisotropy and the large occupation numbers of low-momentum degrees of freedom are to be highlighted. Numerical calculations demonstrate the occurrence of two kinds of instabilities. Primary instabilities result from the specific initial conditions. Secondary instabilities are caused by nonlinear fluctuation effects of the preceding primary instabilities. The time scale associated with the instabilities is of order 1 fm/c. It is shown that the plasma instabilities isotropize the initially strongly anisotropic ensemble in the domain of low momenta ($\lesssim$ 1 GeV). Essential results can be translated from the gauge group SU(2) to SU(3) by a simple rescaling procedure. Finally, the *rôle* of Nielsen-Olesen instabilities in an idealised setup is investigated.

In the second part, the quasi-stationary phase following the saturation of instabilities is studied. Numerical as well as analytical calculations show that the classical time evolution drives the system towards a nonthermal fixed point which exhibits properties of turbulence. The fixed point is characterised by power-law correlation functions of the gauge field. The determined exponents $4/3$ and $5/3$ are identical to those found in scalar field theories, which provides indication for universality out of thermal equilibrium. Taking into account the quantum contributions in the analytical approach it is demonstrated that the full quantum theory does not possess a nonthermal fixed point at large momenta.

Zusammenfassung

Verschiedene Aspekte des Thermalisierungsprozesses in nicht-Abelschen Eichtheorien werden untersucht. Es werden numerische Simulationen in der klassisch-statistischen Näherung wie auch analytische Rechnungen im Rahmen der zwei-Teilchen-irreduziblen effektiven Wirkung durchgeführt und deren Resultate miteinander verglichen. Die physikalischen Größen von zentraler Bedeutung sind einerseits die Korrelationsfunktionen des Eichfeldes in Coulomb- und temporal-axialer Eichung, sowie der eichinvariante Energie-Impuls-Tensor.

Im Anschluss an eine allgemeine Einleitung wird in einem Abschnitt das theoretische Rahmenwerk der nachfolgenden Untersuchungen dargelegt. Dabei wird auch auf den Geltungsbereich der verwendeten Approximationsschemata eingegangen.

Der erste Hauptteil der Arbeit beschäftigt sich mit der frühen Phase des Thermalisierungsprozesses und dabei insbesondere mit der Rolle von Plasma-Instabilitäten. Diese Untersuchungen sind relevant für das phenomenologische Verständnis aktueller Schwerionenexperimente. Zunächst wird ein Ensemble von Anfangsbedingungen entwickelt, welches durch das "colour glass condensate" motiviert ist und wesentliche Aspekte des in Schwerionenkollisionen erzeugten Plasmas wiedergibt. Hierbei sind vor allem die starke Anisotropie sowie die hohe Besetzung von Freiheitsgraden mit kleinen Impulsen hervorzuheben. Numerische Rechnungen zeigen das Auftreten zweier Arten von Instabilitäten. Primäre Instabilitäten resultieren aus den spezifischen Anfangsbedingungen. Sekundäre Instabilitäten werden durch nichtlineare Fluktuationseffekte der vorangegangen primären Instabilitäten hervorgerufen. Die mit den Instabilitäten assoziierte Zeitskala (inverse Wachstumsrate) ist von der Ordnung 1 fm/c. Es wird gezeigt, dass die Plasma-Instabilitäten das anfangs stark anisotrope Ensemble im Bereich kleiner Impulse ($\lesssim$ 1 GeV) isotropisieren. Wesentliche Ergebnisse lassen sich durch einfaches Umskalieren von der Eichgruppe SU(2) zu SU(3) übertragen. Schließlich wird die Rolle von Nielsen-Olesen- Instabilitäten unter idealisierten Bedingungen untersucht.

Im zweiten Teil der Arbeit wird die sich an die Saturierung der Instabilitäten anschließende quasi-stationäre Phase untersucht. Sowohl numerische als auch analytische Rechnungen zeigen, dass die klassische Zeitentwicklung das System zu einem nicht-thermischen Fixpunkt treibt, welcher Eigenschaften von Turbulenz aufweist. Der Fixpunkt wird durch Potenz-Spektren in den Korrelationsfunktionen des Eichfeldes charakterisiert. Die gefundenen Exponenten $4/3$ und $5/3$ weisen dieselben Werte auf wie in skalaren Feldtheorien, was ein Indiz für Universalität fernab des thermischen Gleichgewichts ist. Durch Berücksichtigung der Quantenterme im analytischen Zugang wird gezeigt, dass die volle Quantentheorie keinen nicht-thermischen Fixpunkt bei hohen Impulsen besitzt.

Contents

Chapter 1

Introduction

1.1 General introduction

Today, an overwhelming amount of experimental data confirms the Standard Model as a valid description of nature up to energy scales of the order of about 200 GeV. It is well-known that there are observations (as for instance neutrino oscillations, indications for the existence of dark matter and dark energy and the lack of a quantum theory of gravity) which clearly require that the Standard Model be eventually superseded by a more complete theory. This constitutes one of today's big challenges to high energy theorists. At the same time, a challenge of equivalent importance is posed by the vast number of phenomena lying within the realm of the Standard Model that remain to be explained. Several of these open questions are related to the physics of strong interactions, which is the force governing the structure of protons and neutrons and – indirectly through residual interactions – also the properties of atomic nuclei. Another aspect of Standard Model physics whose understanding cannot be considered satisfactory at present is the topic of quantum fields out of thermal equilibrium. In contrast to field theory in thermal equilibrium or in vacuum there are many open issues that remain to be understood. The motivation for this work arises from questions related to the strong interaction in out-of-equilibrium situations and hence is essentially twofold. This will be outlined briefly in the following paragraphs.

The theory of the strong interaction in the Standard Model is Quantum Chromodynamics (QCD) which has successfully been tested with high precision in collider experiments at high energies ($\gg 1$ GeV). In this regime, the property of asymptotic freedom [83, 132] renders QCD amenable to the methods of perturbation theory. The strong interaction is less well understood at energy scales below approximately 1 GeV, though. One of the particularly demanding aspects of low-energy QCD is to understand the mechanism behind the experimentally observed confinement of quarks and gluons. Related to this is the exploration of the thermodynamics of

strongly interacting matter as temperature and density are varied. It has been established that when increasing the temperature beyond 150 - 200 MeV/k_B ($\sim 2 \cdot 10^{12}$ K) at zero baryon chemical potential the properties of QCD matter are significantly altered in what is referred to as a deconfinement transition[1], ultimately resulting in a new state of matter called the quark gluon plasma. The token problem in this field is to map out the location and the properties of the phase boundaries in the QCD phase diagram, a popular conjecture of which is depicted in Fig. 1.1. It represents what is currently known about *equilibrium* states of strongly interacting matter. Experimentally, this is tackled by heavy ion collision experiments. Such experiments have been carried out in the past at CERN (SPS, "Super Proton Synchrotron") and at Brookhaven National Laboratory (RHIC, "Relativistic Heavy Ion Collider"). Matter under even more extreme conditions will be produced at the LHC ("Large Hadron Collider", CERN) and FAIR ("Facility for Antiproton and Ion Research", GSI) whose scientific operation will commence in the near future. On the theory side, large scale computer simulations in the framework of lattice QCD constitute the main tool to investigate the phase structure of QCD. The QCD phase transition is also relevant for cosmology because the universe has undergone this transition about $10^{-6} - 10^{-5}$ seconds [104] after the big bang, as is also indicated in Fig. 1.1. As an aside, we mention that there is compelling experimental evidence for the creation of a new state of matter with properties attributed to the quark gluon plasma today. For instance, the predicted suppression of heavy quarkonia [110] has indeed been confirmed [54].

A crucial assumption underlying the conclusions drawn from the experimental efforts is that the quark gluon plasma created in a heavy ion collision, as sketched in Fig. 1.2, reaches a state sufficiently close to thermal equilibrium during its short life time of a few fm/c ($\sim 10^{-23}$ seconds). Only then equilibrium states of strongly interacting matter can be probed and predictions from lattice QCD can be tested in a meaningful fashion. It is for this reason that the understanding of *non-equilibrium* processes which can thermalise the plasma is indispensable for experimentally verifying the conjectured structure of the QCD phase diagram.

In fact, several experimental findings have been reported which were originally interpreted as evidence for thermalisation. For several years it was inferred from the success of hydrodynamic computations in describing the pattern of elliptic flow that the plasma produced in heavy ion collisions had to be close to thermal (See [85, 86] and references therein.). However, it has recently become clear [17, 34, 35, 139] that hydrodynamics already works under far milder assumptions than complete equilibration. There are even explicit indications that the medium that has been observed at RHIC is incompletely equilibrated [47]. Thus the question of thermali-

[1] It has emerged from recent studies [14, 60] that this 'transition' is rather a smooth crossover at low baryon chemical potential. See [54] for a review of the quark gluon plasma.

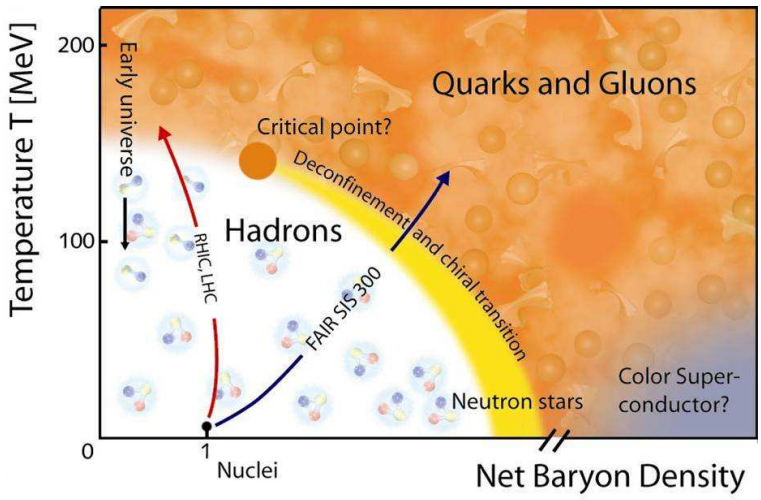

Figure 1.1: The QCD phase diagram as suggested by current research. Confirming its structure and precisely locating the phase transition lines is the subject of ongoing research in both experimental and theoretical physics. Figure taken from the GSI website (www.gsi.de).

sation of the quark gluon plasma has to be regarded as unresolved[2]. On the theory side, it has not been possible yet to reproduce a thermalisation time of the order of 1 fm/c from full QCD, at least in the weak coupling limit which is expected to be applicable at very high collision energies ($\gg$ 1 GeV) due to asymptotic freedom. Some perturbative studies based on Boltzmann equations in fact find very short thermalisation times [158]. Yet, perturbation theory might not be applicable even at weak coupling if particle occupation numbers are sufficiently high. For some years, the picture of the thermalisation process proposed by the "bottom-up scenario" [25] was intensely discussed. However, this scenario turned out to be incomplete when the effects of plasma instabilities where taken into account [16, 50].

The question of whether the quark gluon plasma produced in experiments at RHIC is weakly or strongly coupled – two alternatives commonly referred to as wQGP and sQGP, respectively – is also currently unanswered. It is hoped that the outcome of future experiments at the LHC will resolve this puzzle because they will allow the creation of a plasma at far higher energy scales where the asymptotically free limit should be better realised than at RHIC. Over the last decade, the colour glass condensate (CGC, cf. [84, 87, 95, 96, 111] for instance) has intensively been studied as a possible framework for non-equilibrium initial conditions in collider experiments. It describes a classical ensemble of low-momentum gluons in a weakly coupled, yet nonpertur-

[2]Contrary to what applies to the initial plasma, there are strong indications that the hadronic matter in heavy ion collision experiments after freeze-out is in a thermal state. Hadronic particle yields can be described very well by statistical models based on the assumption of thermal equilibrium [13, 28, 54].

(a) (b)

Figure 1.2: Schematic view of a relativistic heavy ion collision as observed in the laboratory frame. (a) Two approaching heavy nuclei. Their nucleonic constituents are protons and neutrons which are "colourless" (*i.e.* they have a zero net colour-charge). Due to Lorentz contraction, the nuclei appear as flat, pancake shaped objects. (b) With some hadronic debris escaping, an out-of-equilibrium quark gluon plasma is created. The plasma is represented by the yellow-shaded region. Its constituents are deconfined quarks and gluons and they are subject to the strong interaction. In this work we focus on the dynamics of the medium in the centre of the collision indicated by the rectangular box. The parton momenta in the centre of the plasma are preferably aligned perpendicular to the collision axis due to the geometry of the collision.

bative, limit. In summary, a big share of the research presented in this thesis is dedicated to the investigation of the *rôle* of plasma instabilities in the early stages of the thermalisation process in a heavy ion collision.

The second motivation for this thesis is to contribute to the progress of non-equilibrium quantum field theory. The generic task is to compute the time evolution of the density operator ρ starting from an arbitrary initial density matrix ρ_0. This problem can be cast into a functional integral over a closed-time path, which is known as the Schwinger-Keldysh formalism [92, 145]. The latter allows to directly compute the time evolution of Green functions. As in the case of equilibrium or vacuum field theory, it is in general not possible to solve the equations analytically and thus one has to stick to approximations. While there is a set of well-developed techniques and approximation schemes for quantum field theory (QFT) in thermal equilibrium[3], the situation is less satisfactory for non-equilibrium QFT. The latter is inherently more complicated than its equilibrium counterpart, which is exemplified by the categorical failure of perturbation theory (without resummation) due to secular terms in the evolution equations for the correlation functions [31]. Monte Carlo methods based on importance sampling cannot be applied either because the real-time functional integral intrinsically features a complex probability amplitude, which is a particularly difficult example of the sign problem. Regarding the field content of the Standard

[3]This is understood to include vacuum quantum fields in the limit of vanishing temperature and density.

Model the situation is such that methods for scalar and spinor fields out of equilibrium are better developed than for gauge theories, especially non-Abelian ones. The non-equilibrium time evolution of the latter keeps posing serious challenges to theorists and this will be the second piece of motivation for the work at hand.

Over the last ten years important progress has been achieved in the field of non-equilibrium quantum field theory owing to nPI effective action techniques[4] (also known as Φ- derivable approximation). These methods avoid the difficulties caused by secular terms which are encountered in perturbation theory because they imply a resummation of Green functions up to infinite order in the coupling constant of the theory under investigation. Furthermore, they allow for non-perturbative methods such as $1/N$ expansions and corresponding numerical computations. nPI techniques were applied with great success to study systems of scalar and fermionic particles [6, 24,29,32,36,40] and – with certain restrictions – also to gauge fields [22,30,56,135–138,143]. A number of very diverse physical systems has been studied in the nPI effective action approach including early universe cosmology [23,44,81,150], electromagnetic plasmas [12,57,58], and the out-of-equilibrium behaviour of cold atomic gases [37,53,78,79]. Recent works employing nPI effective actions have yielded exciting insights into the physics of non-thermal stationary states suggesting that these display universality akin to (continuous) equilibrium phase transitions [39].

Of course, there are also other approximation schemes to study the out-of-equilibrium time evolution of quantum fields. Mean-field methods [62–64, 67] are plagued by an infinite number of unphysical conserved quantities [31]. Hence they can only be employed to a very restricted set of problems. Over the past few years very promising progress has been made in the field of stochastic quantisation which could turn out to be a way to overcome the sign problem encountered in both real-time QFT and QCD at non-zero chemical potential [1,2,8,33,45,46].

For quantum systems featuring high occupation numbers it has been shown [31,37,87,96] that the time evolution of an initial ensemble in the quantum theory can be computed with high precision from the classical approximation. The latter can be applied in several ways. The most common approach is to sample field configurations from the initial density operator and to subsequently evolve these forward in time by solving the classical field equations. This method can be used firstly to study those systems which are not amenable to nPI- effective action techniques. Secondly, it allows to test and benchmark other methods (See [3,5,6] for examples.). The classical approximation has extensively been employed for gauge theories in the context of sphaleron transitions in the early universe [9–11,82,116,119], electroweak tachyonic preheating [118,146,148,152] and recently also to study the properties of heavy quarks in a thermal medium [99–101]. Given that a quantum system will always evolve towards quantum thermal

[4]These methods were originally proposed for equilibrium field theory in [27,68,90]. See [31,55] for reviews about their application to out-of-equilibrium field theory.

equilibrium (featuring quantum statistical distribution functions) it is obvious that the classical approximation cannot approximate the entire time evolution. Its validity is limited to those stages of the thermalisation process that are governed by high occupation numbers per mode.

From these two motivations, the objective of this work is to study the time evolution of an initial ensemble of non-Abelian gauge fields out of equilibrium. Using initial conditions that establish contact to heavy ion collision experiments we study processes that drive the quark gluon plasma towards an equilibrium state. The central question in this context is to understand what mechanisms are behind the applicability of hydrodynamical computations. At the same time, we want to compare and benchmark results obtained by employing different approaches in order to contribute to the more formal aspects of non-equilibrium gauge fields.

1.2 Outline of this work

In this thesis we make use of both the classical approximation as well as 2PI resummation techniques to study the real-time dynamics of non-Abelian gauge fields. These approaches are applied to investigate the physics of plasma instabilities and of non-thermal fixed points (quasi-stationary states).

In the first part of this work, we numerically investigate plasma instabilities (*i.e.* exponentially growing modes of the classical fields) in non-Abelian gauge theories and their impact on the thermalisation process. Plasma instabilities are a well-known feature of electrodynamic plasmas which are described by Abelian gauge theories. There exist several kinds of instabilities amongst which the Weibel- or two-stream instability [154] is the most relevant one in the context of this work. This kind of instability occurs if the momentum distribution of the plasma's charge carriers is anisotropic. The QCD analogue of this instability is known as the chromo-Weibel instability [120]. Aside from those instabilities, which are common to Abelian and non-Abelian gauge theories, there are also instabilities in the non-Abelian gauge theory which do not possess an Abelian counterpart and are thus genuinely non-Abelian in nature. An example for this is the Nielsen-Olesen instability [59, 129, 147, 151] which occurs in homogeneous chromo-magnetic fields.

In the context of heavy ion collisions, plasma instabilities have been conjectured to play a *rôle* in the early-time dynamics of the quark gluon plasma produced in heavy ion collisions. More specifically, they have been suggested as the mechanism that quickly drives the initial, highly anisotropic system of mainly gluonic degrees of freedom towards an isotropic state [17, 74–76, 121–125]. The central question here is to compute the characteristic time scale (inverse

growth rate) of these instabilities and check if it is short enough to enable these instabilities to have a significant impact before the onset of the hydrodynamic regime. The challenge posed by experiment is to explain isotropization within a time span of 1 to 2 fm/c. Moreover, it is important to study the phenomenology of these instabilities (for instance, which degrees of freedom are the most strongly affected ones) and to make predictions that can be verified in collider experiments.

The second part of this work focuses on nonthermal fixed points. These quasi-stationary states are typically characterised by power-law spectra and have recently attracted a lot of interest [18, 19, 39, 41, 73, 112, 113, 126, 159]. In fact, two kinds of phenomena falling into this category have to be distinguished [39]. First, there are power-law solutions in the limit of vanishing momentum ("infrared") which are non-equilibrium generalisations of the familiar critical phenomena in thermal equilibrium featuring strongly enhanced, long range correlations. Second, there are quasi-stationary solutions manifesting themselves by power-law spectra in the UV[5] which are reminiscent of Kolmogorov wave turbulence. Although an investigation of non-equilibrium critical phenomena in QCD is certainly a very interesting and promising project we will not consider this class of fixed points here in much detail. Instead, we will study the turbulent regime. This we accomplish by comparing the results of numerical simulations to predictions from the 2PI scheme in both the classical limit and the full quantum theory. The investigation of turbulence in the classical theory is interesting in itself. Classical non-Abelian gauge theory with its inherently nonlinear field equations (Yang-Mills equations) has been known to feature turbulence and chaotic dynamics for about two decades [77, 127, 128, 156, 157]. Apart from that, it turns out to be an excellent test case for comparing the results from numerical simulations of the classical-statistical theory to 2PI calculations carried out in the classical limit as well as the full quantum theory. This could also serve to test the proposition of far-from-equilibrium universality when compared to results in scalar theories. Moreover, it would be desirable to carry out comparisons of the classical approximation with other approximation schemes (*e.g.* Hartree, 1PI) as studied in the case of scalar theories in [4, 5, 52].

The outline of this thesis is as follows. In Chapter 2 we briefly review the theoretical background and the numerical techniques that will subsequently be applied. This also serves to fix the notation and to define various quantities of relevance throughout this work.

Chapter 3 is concerned with the numerical study of plasma instabilities in the pure SU(2) gauge theory. We propose a set of initial conditions that capture the physics of heavy ion col-

[5] In agreement with the customary use in the literature, the expressions "infrared" (IR) and "ultraviolet" (UV) are frequently used in this thesis as synonyms for low and high momenta, respectively. Besides analogy, there is no relation to the corresponding parts of the electromagnetic spectrum.

lisions in Section 3.1. Employing these initial conditions in classical-statistical simulations we have confirmed the occurrence of instabilities in an anisotropic, purely gluonic medium. There are two kinds of instabilities. *Primary instabilities* originate from the particular initial conditions under consideration while *secondary instabilities* are induced by nonlinear effects of the primary ones. Furthermore, we compute instability growth rates as a function of spatial momentum. The time scale associated with the plasma instabilities is found to be of order 1 fm/c for realistic choices of the lattice parameters. We find that plasma instabilities drive the field configurations towards an isotropic state. This effect is most pronounced in the modes of long wavelength. For sufficiently low momenta $\lesssim 1$ GeV, an isotropic state is reached by virtue of the instabilities. Higher momentum degrees of freedom do not completely isotropize before the instabilities saturate. All of these findings are presented in Section 3.2. In the ensuing Section 3.3 we show that the results obtained for SU(2) gauge theory can to a big extent be extrapolated to SU(3) in a controlled way. Section 3.4 investigates the question whether the instabilities arising from our initial conditions are of chromo-Weibel or Nielsen-Olesen type. To that end, we numerically study homogeneous magnetic fields in order to investigate the growth rates of Nielsen-Olesen instabilities. It is found that their growth rates can be significantly higher than those of the instabilities arising from the initial conditions employed in the previous analysis. Moreover, we estimate what is the maximum possible growth rate under realistic assumptions for heavy ion collisions. The latter is of particular relevance to draw conclusions about the experiments carried out at present and future accelerator facilities. Section 3.5 is entirely devoted to the discussion of this issue.

The topic of Chapter 4 is the investigation of turbulence-like, nonthermal fixed points. In Section 4.1, we find power laws in numerical computations of equal-time correlation functions and determine their exponent κ. The latter turns out to be in excellent agreement with the value $\kappa = 4/3$. Subsequently, an analytic calculation up to three-loop order in the 2PI effective action is carried out in Section 4.2. In the classical limit, solutions for the propagators are found that feature power-law spectra admitting the exponents $\kappa = 4/3$ and $\kappa = 5/3$. These values are identical to the spectral indices found in scalar field theories and hence these findings provide evidence for the notion of universality far from thermal equilibrium. It is also shown in Section 4.2 that the scaling solutions are purely classical, *i.e.* they are not present in the full quantum theory. Finally, we briefly discuss what can be expected to happen in the IR in Section 4.3.

The appendices contain a summary of the notation and conventions used in the main body of the text, a section on the numerical stability of our simulations and a collection of results from

equilibrium simulations.

Parts of this work have already been published in the following papers and conference proceedings:

1. J. Berges, S. Scheffler and D. Sexty, *"Isotropization times in non-Abelian gauge theory"*, Progress in Particle and Nuclear Physics **61** (2008), p. 86.

2. J. Berges, S. Scheffler and D. Sexty, *"Bottom-up isotropization in classical-statistical lattice gauge theory"*, Physical Review D **77** (2008), p. 034504, arXiv:0712.3514 [hep-ph].

3. S. Scheffler, *"Turbulent spectra in real-time gauge field evolution"*, Nuclear Physics A **820** (2009), p. 127C, arXiv:0812.2344 [hep-ph].

4. J. Berges, D. Gelfand, S. Scheffler and D. Sexty, *"Simulating plasma instabilities in SU(3) gauge theory"*, Physics Letters B **677** (2009), p. 210 - 213, arXiv:0812.3859 [hep-ph].

5. J. Berges, S. Scheffler and D. Sexty, *"Turbulence in nonabelian gauge theory"*, Physics Letters B **681** (2009), p. 362 - 366, arXiv:0811.4293 [hep-ph].

Chapter 2

Theoretical background

This chapter sets the stage for the ensuing study of non-Abelian gauge theories out of thermal equilibrium. In Section 2.1, the formulation of QCD and Yang-Mills theory is briefly reviewed. Section 2.2 summarises the relevant formal aspects of non-equilibrium quantum field theory. In section 2.3, we describe how Yang-Mills theory can be discretised in a way that allows for numerical simulation in real time.

2.1 A brief summary of QCD and pure Yang-Mills theory

In this Section we summarise some basic facts about QCD and pure Yang-Mills theories from standard textbooks [88, 114, 130, 144, 155].

Quantum chromodynamics (QCD) is a non-Abelian gauge theory on Minkowski- spacetime with six kinds of fermions which are referred to as quarks. The quantum number allowing to distinguish the quark species is called "flavour". Besides flavour, each quark carries a charge under the fundamental representation of the gauge group SU(3) which can take three different values ("colours"). The forces between the fundamental fermions are mediated by the exchange of gluons which are massless spin-1 particles. Contrary to Abelian gauge theories like quantum electrodynamics (QED), the exchange bosons carry a colour charge as well (more precisely, a charge which transforms under the adjoint rather than the fundamental representation of the gauge group) and hence interact with each other. This gives rise to a vast number of new phenomena which are not encountered in QED.

To keep the discussion sufficiently general we will generalise to an arbitrary SU(N)- gauge group with integer $N \geq 2$ keeping in mind that the physically relevant case of QCD is $N = 3$. The gauge fields A_μ then define a covariant derivative D_μ whose action on a field ϕ in the fundamental

representation is defined through

$$D_\mu \phi = \partial_\mu \phi - igA_\mu \phi \; . \tag{2.1}$$

It is always possible to choose local coordinates and a local co-moving frame allowing for a decomposition of the fermion fields Ψ_f (with f denoting the flavour index) and the gauge fields A_μ in terms of expansion coefficients $\psi_f^a(x)$ and $A_\mu^a(x)$. The colour index a runs from 1 to N for the fermions in the fundamental representation and from 1 to $N^2 - 1$ for the gauge bosons. A gauge transformation is a change of the basis in the bundle space which is described by an SU(N)- valued function $G(x)$. It has the following effects on the fermion fields and the gauge fields:

$$\begin{aligned} \psi(x) &\mapsto \psi'(x) = G(x)\psi(x) \\ A(x) &\mapsto A'(x) = G(x)A(x)G^\dagger(x) + \frac{i}{g}(dG)(x)G^\dagger(x) \, . \end{aligned} \tag{2.2}$$

Here g is the coupling constant. Writing $A = A_\mu dx^\mu$, the transformation of A in Eq. (2.2) amounts to

$$A_\mu(x) \mapsto A'_\mu(x) = G(x)A_\mu(x)G^\dagger(x) + \frac{i}{g}(\partial_\mu G(x))G^\dagger(x) = G(x)A_\mu(x)G^\dagger(x) - \frac{i}{g}G(x)\partial_\mu G^\dagger(x) \tag{2.3}$$

for the matrix-valued fields A_μ. The gauge fields can be decomposed further in a basis of the SU(N) Lie algebra[1] according to

$$A_\mu = A_\mu^b \, \lambda^b \tag{2.4}$$

where the generators λ^b are normalised such that $\mathrm{Tr}(\lambda^a \lambda^b) = \delta^{ab}/2$ and $a, b \in \{1, ..., N^2 - 1\}$. For SU(2)- gauge theory, $\lambda^b = \sigma^b/2$ where σ^b denotes the Pauli matrices with $b \in \{1, 2, 3\}$.

Generalising the familiar electric and magnetic fields from electrodynamics one is led to the definition of the matrix-valued field strength [2] $\mathcal{F}_{\mu\nu} = \partial_\mu A_\nu - \partial_\nu A_\mu - ig[A_\mu, A_\nu]$, whose local coordinate expression reads

$$\mathcal{F}_{\mu\nu}^a = \partial_\mu A_\nu^a - \partial_\nu A_\mu^a + g f^{abc} A_\mu^b A_\nu^c \tag{2.5}$$

employing the anti-symmetric SU(N) structure constants f^{abc}. For SU(2), f^{abc} is given by the Levi-Civita tensor ϵ^{abc}. Under gauge transformations (2.2) the field strength transforms according to

$$\mathcal{F}_{\mu\nu} \mapsto \mathcal{F}'_{\mu\nu} = U(x)\mathcal{F}_{\mu\nu}U^\dagger(x) \; . \tag{2.6}$$

[1] Strictly speaking, the Lie algebra is spanned by the matrices $i\,\lambda^b$.

[2] We denote the field strength by the symbol $\mathcal{F}$ rather than F. The latter is reserved for the statistical propagator defined in Eq. (2.22).

The decomposition of the field strength is analogous to the one of the gauge field and reads $\mathcal{F}_{\mu\nu} = \mathcal{F}^a_{\mu\nu}\lambda^a$. Electric and magnetic fields can be identified in the same fashion as in electrodynamics [89]. Note though that these are not gauge invariant in the non-Abelian theory but rather transform like a linear map as implied by Eq. (2.6). This implies however that traces of products of products of the field strength are gauge invariant. This is of significance for the definition of a gauge-invariant Lagrangian, which we now turn to.

Employing Feynman's slash notation $\not{D} \equiv \gamma^\mu D_\mu$, the Lagrangian density of QCD [130, 155] is given by

$$\mathcal{L}_{\mathrm{QCD}}(\psi(x), \bar{\psi}(x), A(x)) = -\frac{1}{2}\mathrm{Tr}(\mathcal{F}_{\mu\nu}(x)\mathcal{F}^{\mu\nu}(x)) + \sum_f \bar{\psi}_f(x)(i\not{D} - m_f)\psi_f(x) \,. \tag{2.7}$$

When quantising gauge theories in the framework of the Faddeev-Popov method it turns out that one has to include certain gauge fixing terms. Since this is not of direct relevance to the remainder of this work we will omit these in what follows.

Because the exchange bosons are charged under the adjoint representation of the gauge group they interact with each other. Plugging in Eq. (2.5) into Eq. (2.7) one immediately sees that these intercations arise from cubic and quartic terms in the gauge field. Therefore, a non-Abelian gauge theory without any matter fields already constitutes an interacting theory which deserves being studied itself. Keeping only gluonic degrees of freedom, the above Lagrangian (2.7) reduces to

$$\mathcal{L}_{\mathrm{YM}}(A(x)) = -\frac{1}{2}\mathrm{Tr}(\mathcal{F}_{\mu\nu}(x)\mathcal{F}^{\mu\nu}(x)) = -\frac{1}{4}\mathcal{F}^a_{\mu\nu}\mathcal{F}^{a\mu\nu} \,, \tag{2.8}$$

which is commonly referred to as pure Yang-Mills theory. By construction, both $\mathcal{L}_{\mathrm{QCD}}$ and $\mathcal{L}_{\mathrm{YM}}$ are invariant under gauge transformations (2.2). In both cases the action is given as the spacetime integral

$$S = \int d^4x\, \mathcal{L} \tag{2.9}$$

with $\mathcal{L}$ representing either of the Lagrangians (2.7) or (2.8).

We will focus on the pure Yang-Mills theory defined through Eq. (2.8) in the remainder of this work for several reasons. Firstly, the out-of-equilibrium plasma created in a heavy ion collision is expected to be dominated by gluonic degrees of freedom, as will be outlined in Section 3.1. Bosonic occupation numbers are typically large and thus their effect should dominate over those of the fermions whose occupation numbers are bounded by the Pauli-exclusion principle. It was found in the context of scalar theories that including fermions does not significantly affect the thermalisation process of the bosons, at least at weak couplings [40]. Second, numer-

ical simulations including fermions are far more demanding in terms of computing resources. Finally, it is natural to study the slightly less complicated theory first before tackling full QCD. This will help to disentangle the effects of fermions from the gauge field dynamics in possible later studies.

Apart from neglecting the quark fields, we will make the simplification of using SU(2) as a gauge group rather than the physical SU(3) in most of the work. It has been checked that there are no qualitative differences in many of the results of later chapters [38, 80]. This issue will be discussed in detail in Section 3.3.

We close this short review of non-Abelian gauge theories with a discussion of the classical field equations. They can be derived from (2.7) or (2.8) by applying the Euler-Lagrange equations in a straightforward way. Doing so, one obtains the Yang-Mills equations

$$D_\mu \mathcal{F}^{a\mu\nu} = \partial_\mu \mathcal{F}^{a\mu\nu} + g f^{abc} A^b_\mu \mathcal{F}^{c\mu\nu} = J^{a\nu} \,. \tag{2.10}$$

In the case of full QCD (2.7) the current on the right hand side of the field equation reads $J^{\nu a} = \bar{\psi}\gamma^\nu \lambda^a \psi$, while it vanishes in pure Yang-Mills theory (2.8). In the latter case, the field equations (2.10) can be cast into the form

$$\partial_\mu \partial^\mu A^{a\nu} - \partial_\mu \partial^\nu A^{a\mu} + g f^{abc} A^b_\mu \Big(\partial^\mu A^{c\nu} - \partial^\nu A^{c\mu} + g f^{cde} A^{d\mu} A^{e\nu} \Big) = 0 \tag{2.11}$$

on the level of the gauge fields. This is set of nonlinear, coupled partial differential equations for the $4\,(\mathrm{N}^2 - 1)$ components A^a_μ of the gauge field. For $g = 0$, it reduces to a set of uncoupled Maxwell equations familiar from classical electrodynamics.

Because $F_{00} = 0$ due to anti-symmetry in the Lorentz indices the equation for $\nu = 0$ is a non-dynamical constraint:

$$\partial_j \mathcal{F}^{a\,j0} + g f^{abc} A^b_j \mathcal{F}^{c\,j0} = J^{a0} \,. \tag{2.12}$$

This is known as the Gauss constraint and reduces to the familiar Gauss's law of electrodynamics [89] in the Abelian case $g = 0$. It can be shown easily that the dynamical field equations (*i.e.* Eq. (2.11) for $\mu = 1, 2, 3$)) imply the conservation of the left hand side of Eq. (2.12) in time [88, 155]. Therefore, the Gauss constraint is fulfilled at all times if it is satisfied at an arbitrary instant of time. It can also be written as

$$C(x) := D_j E^a_j(x) = 0 \,. \tag{2.13}$$

Obviously, the stationary points (and hence the solutions to the field equations) of the action computed by integrating (2.8) cannot be unique because the integrand is invariant under gauge transformations (2.3). In order to render the solution unique the system of partial differential

equations (2.11) has to be augmented by a gauge condition. In this work, we will mainly employ two gauges[3], namely the temporal axial gauge (also known as Weyl gauge) defined by

$$A_0 = 0 \tag{2.14}$$

and the Coulomb gauge whose defining equation is

$$\nabla \cdot \mathbf{A} = \sum_j \partial_j A_j = 0 \,. \tag{2.15}$$

The temporal axial gauge is particularly convenient for a numerical treatment of the Yang-Mills equations. The Coulomb gauge on the other hand is a physical gauge in the sense that its spatial components are transverse, as can be seen by Fourier transforming the gauge condition (2.15) to momentum space.

2.2 Non-equilibrium quantum field theory

In this section we will briefly summarise the prerequisites from non-equilibrium quantum field theory that are relevant for this work. We refer to [31, 55, 90, 104] for further details.

In a general quantum theory governed by a Hamiltonian H, the central object of statistical physics is the density operator ρ that is also referred to as density matrix. In the Schrödinger picture its time evolution is determined by the von Neumann- equation

$$\partial_t \rho = \frac{-1}{i\hbar} [\rho, H] \,. \tag{2.16}$$

This time derivative vanishes if H and ρ commute, meaning that ρ describes a stationary ensemble. If ρ is known, ensemble averages of a physical observable O can be computed via $\langle O \rangle = \mathrm{Tr}\,(\rho O)$. The formulation of classical statistical physics proceeds in a completely analogous way. The main differences are that the density operator is replaced by a corresponding phase-space density function and the Liouville equation replaces the von Neumann equation.

Equilibrium statistical mechanics is based on the postulate that the equilibrium density operator is the one that maximises the Gibbs entropy $S = -k_B \mathrm{Tr}\,(\rho \ln \rho)$. Here, k_B is Boltzmann's constant and the logarithm of the density operator is defined through the series expansion of the logarithm. The maximisation has to be carried out under the constraint $\mathrm{Tr}\,(\rho) = 1$ and possible

[3] In fact, the below equations still do not entirely fix the ambiguity in the gauge field. The temporal axial gauge allows for further time-independent gauge transformations while Coulomb gauge suffers from the problem of Gribov copies [155].

further constraints that are suitable to enforce the boundary conditions of the specific ensemble under consideration.

The central problem of non-equilibrium statistical physics is to solve Eq. (2.16) for a given initial density matrix ρ_0. A typical question of interest is then to study how long it takes the ensemble to thermalise or how long relaxation to equilibrium takes in case of a small deviation from thermal equilibrium (The latter question can even be dealt with in terms of the equilibrium formalism by means of the linear response approximation [104].).

In non-equilibrium quantum field theory it turns out that it is more suitable for many purposes to rephrase the initial value problem of the von Neumann equation (2.16) in terms of a path integral. A generating functional[4] is given by [31, 55, 92, 145]

$$Z[J,R,\rho_0] = \int dA^{(1)}dA^{(2)}\langle A^{(1)}|\,\rho_0\,|A^{(2)}\rangle \times \int_{A^{(1)}}^{A^{(2)}} \mathcal{D}A\, \exp\left\{i\Big(S[A] + \int_x J(x)\cdot A(x) + \frac{1}{2}\int_{x,y} A(x)R(x,y)A(y)\Big)\right\} \tag{2.17}$$

from which correlation functions can be computed by functional differentiation with respect to the source terms J and R. ρ_0 is the initial density matrix. The fields appearing in the functional integral are evaluated along a closed time path (Schwinger-Keldysh contour) where the time ordering is such that times on the backward contour are regarded as later than any instant of time on the forward contour and the ordering on the backward contour is anti-chronological in the values of x^0 or y^0, respectively. Functionally differentiating Eq. (2.17) with respect to J or R then yields correlation functions which are time-ordered in terms of the contour parameter. The time-ordering operation along the contour will be denoted by $\mathcal{T}$. In complete analogy to quantum field theory in vacuum or equilibrium, the generating functional for connected correlation functions $W[J,R,\rho_0]$ is defined from Z through

$$Z \equiv \exp(iW)\,. \tag{2.18}$$

The field expectation value is given as a functional derivative w. r. t. to J according to

$$\mathcal{A}^b_\mu = \langle A^b_\mu\rangle = \frac{\delta W}{\delta J^\mu_b}\,. \tag{2.19}$$

For the purposes of this work, the expectation values of all gauge field components $\mathcal{A}^b_\mu = \langle A^b_\mu\rangle$ are

[4] Lorentz- and colour indices are omitted here for the sake of brevity. For QCD or pure Yang-Mills theory the action $S[A]$ in this integral will be the spacetime integral of either (2.7) or (2.8) supplemented by adequate gauge fixing terms.

assumed vanish because we do not consider gauge theories with spontaneous symmetry breaking. Therefore, none of the effective actions depends on $\mathcal{A}$ in the following. The full, connected propagator is defined as

$$G^{ab}_{\mu\nu}(x,y) := \langle\, \mathcal{T} A^a_\mu(x) A^b_\nu(y) \,\rangle - \mathcal{A}^a_\mu(x)\mathcal{A}^b_\nu(y) = 2\frac{\delta W}{\delta R^{\mu\nu}_{ab}(x,y)} - \mathcal{A}^a_\mu(x)\mathcal{A}^b_\nu(y)\,, \tag{2.20}$$

where the terms containing $\mathcal{A}$ are assumed to be zero in the following, as outlined before.

The 2PI effective action Γ_{2PI} is defined as the two-particle irreducible contribution to the Legendre transform Γ of W

$$\Gamma[\mathcal{A}, G] = W - \int_x \frac{\delta W}{\delta J(x)} J(x) - \int_{x,y} \frac{\delta W}{\delta R(x,y)} R(y,x)\,. \tag{2.21}$$

Diagrammatically, Γ_{2PI} is the sum of all closed diagrams that cannot be separated in two disjoint pieces by cutting two propagator lines. The propagator lines appearing in the diagrams for Γ_{2PI} represent the full, resummed propagators which contain contributions up to infinite order in the gauge coupling g. By omitting the dependence of Γ and Γ_{2PI} on the ghost propagator we have tacitly assumed that we will use a ghost-free gauge (such as axial gauges) or have some other justification to neglect the ghosts in the following.

The time-ordered propagator (2.20) can be decomposed into two, generally independent functions. It has proven especially useful to decompose it into a symmetric and an anti-symmetric part. The first is given by the statistical propagator

$$F^{ab}_{\mu\nu}(x,y) \;=\; \frac{1}{2}\langle\, \{A^a_\mu(x), A^b_\nu(y)\} \,\rangle\,. \tag{2.22}$$

The anti-symmetric part is referred to as the spectral function[5] and reads

$$\rho^{ab}_{\mu\nu}(x,y) \;=\; i\langle\, [A^a_\mu(x), A^b_\nu(y)] \,\rangle\,. \tag{2.23}$$

It contains information about the accessible states of the theory while the statistical function is related to the occupation number of those states, at least in the limit of weak coupling. In thermal equilibrium $F^{ab}_{\mu\nu}$ and $\rho^{ab}_{\mu\nu}$ are related by virtue of the Kubo-Marin-Schwinger condition [98, 108] (fluctuation-dissipation relation) and thus there is only one independent correlation function. This does not hold in a generic non-equilibrium situation, though. Therefore, the statistical propagator and the spectral function will be considered as completely independent functions in the remainder. The time-ordered propagator (2.20) can be represented in terms of the spectral

[5] Note that some authors, *e.g.* [49, 55], prefer to define the spectral function without the factor i.

and statistical function as[6]

$$G^{ab}_{\mu\nu}(x,y) = F^{ab}_{\mu\nu}(x,y) - \frac{i}{2}\,\mathrm{sign}(x^0 - y^0)\,\rho^{ab}_{\mu\nu}(x,y)\ . \tag{2.24}$$

Furthermore, we recall the definitions of the advanced and retarded propagators

$$G^{(A)\,ab}_{\mu\nu}(x,y) := -i\,\Theta(y^0 - x^0)\langle\,[A^a_\mu(x), A^b_\nu(y)]\,\rangle \tag{2.25}$$

$$G^{(R)\,ab}_{\mu\nu}(x,y) := i\,\Theta(x^0 - y^0)\langle\,[A^a_\mu(x), A^b_\nu(y)]\,\rangle\,. \tag{2.26}$$

The full propagator is related to the free propagator $G_0(x,y)$ and the gluon self-energy Π through the Dyson-Schwinger equation $G^{-1} = G_0^{-1} - \Pi$. The self-energy can be computed from the 2PI effective action by functional differentiation with respect to the full propagator according to

$$\Pi^{\mu\nu}_{ab}(x,y) = 2i\,\frac{\delta\Gamma_{2PI}}{\delta G^{ab}_{\mu\nu}(x,y)}\ . \tag{2.27}$$

Separating off a local contribution proportional to $\delta^{(4)}(x-y)$ (An example for such a contribution is given by the thermal tadpole mass.), the non-local part of the self-energy can be split up into a symmetric and an anti-symmetric term in a similar way as the propagator

$$\Pi^{\mu\nu}_{ab}(x,y) = -i\Pi^{(0)}\delta^{(4)}(x-y) + \Pi^{\mu\nu}_{(F)\,ab}(x-y) - \frac{i}{2}\mathrm{sign}(x^0 - y^0)\,\Pi^{\mu\nu}_{(\rho)\,ab}(x,y)\ . \tag{2.28}$$

Starting from the Dyson-Schwinger equation one can derive evolution equations for the statistical and spectral functions which represent a set of coupled integro-differential equations for the spectral function and the statistical propagator [30, 31].

From the behaviour of the running coupling in QCD (and also pure Yang-Mills theory) it is clear that low energy phenomena are not amenable to a perturbative treatment. Perturbation theory also breaks down computations of thermodynamic quantities in gauge theories in equilibrium [105]. It is known that the applicability of perturbative methods in non-equilibrium physics is severely limited due to secular terms in the evolution equations of the Green functions [31]. Thus a non-perturbative approach, such as the classical-statistical approximation, is obviously required to investigate non-Abelian gauge theories out of thermal equilibrium.

As mentioned in the Introduction, the time evolution of a quantum-statistical system can be approximated classically, which we now discuss in more detail. For a system which is invariant under spatial translations all Green functions only depend on the displacement $\mathbf{x} - \mathbf{y}$ and thus one

[6] When using the closed-time path effective action the sign- function appearing in (2.24) has to be understood in the way that all times on the backward contour are later than the forward contour.

can compute the Fourier transforms with respect to the latter. One can show that

$$|F(x^0, y^0, \mathbf{p})F(x^0, y^0, \mathbf{q})| \gg \frac{3}{4} |\rho(x^0, y^0, \mathbf{p})\rho(x^0, y^0, \mathbf{q})| \tag{2.29}$$

serves as a sufficient criterion for the applicability of the classical-statistical approximation [3, 31]. Eq. (2.29) is known as the classicality condition which has to hold for arbitrary times x^0, y^0 and for all spatial momenta $\mathbf{p}, \mathbf{q}$. Neglecting contributions of spectral functions whenever they appear in combinations of the form $FF \pm \rho\rho$ one obtains the same evolution equations as for a classical-statistical system [3, 31, 37, 48, 66, 109, 131]. Hence one can approximate the quantum time evolution by solving classical field equations; quantum physics still enters through the initial conditions. Given that the statistical propagator (2.22) can be related to mode occupation number in many situations [31] and that the spectral function (2.23) is typically of order one in natural units, the classicality condition demands that occupation numbers be large compared to one[7]. Note however that Eq. (2.29) does not require to make use of the notion of particle numbers. This is advantageous in situations where the definition of a particle number is ambiguous.

The propagators computed in the classical approximation receive contributions up to infinite order in the gauge coupling g. Hence the classical approximation is a nonperturbative approximation scheme, as required for the purposes of this work.

2.3 Real-time lattice simulations

In order to apply the classical approximation to a non-Abelian gauge theory we need a method to numerically solve the Yang-Mills equations (2.11). Although this can be done directly[8] in terms of A^b_μ it turns out that the most adequate way to implement numerical simulations is to employ a discretisation as in standard lattice QCD [69, 114, 144]. We will follow the Lagrangian approach [9] which - in temporal axial gauge (2.14) - can be shown to be equivalent to the Hamiltonian scheme [93] with discretised time. We refer to [9, 11, 116–118] for further details of the numerical implementation.

The discretisation of Yang-Mills theory as defined by the Lagrangian density (2.8) proceeds along similar lines as in the vacuum or in thermal equilibrium. For obvious reasons it is not possible to analytically continue the fields to imaginary times so that the discretisation needs to be done in Minkowski spacetime. As usual, we consider points x on a hyper-cubic lattice. The points of the discrete spacetime are separated from each other by a distance a_s in spatial directions and a_t in the temporal direction. In order to ensure numerical stability [133] we always use $a_\mathrm{t}/a_s \ll 1$. For a given point x, the neighbours in spatial and temporal directions are denoted by

[7] An instructive discussion of this can be found in [87].

[8] Examples are provided in [77, 156, 157].

$x+\hat{j}$ and $x+\hat{t}$, respectively. We will frequently employ the notation $x \equiv (x^0, \mathbf{x}) \equiv (t, \mathbf{x})$ in order to separate temporal and spatial coordinates. Analogously, $\mathbf{k}, \mathbf{p}, \mathbf{q}, ...$ will denote spatial momenta resulting from Fourier transforming w. r. t. spatial coordinates. We use periodic boundary conditions in numerical computations but this is not of direct relevance at this point. Greek indices are understood to take values in $0, 1, 2, 3$ where 0 represents the time coordinate. Correspondingly, lower case Latin indices run over $1, 2, 3$ and represent the spatial coordinates x, y, z, respectively.

In lattice gauge theory the hermitian gauge fields $A_\mu(x)$ are expressed in terms of link variables $U_\mu(x) \in \mathrm{SU(N)}$ by virtue of the following relation:

$$U_\mu(x) := \exp(iga_\mu A_\mu(x)) = \exp\Big(iga_\mu A^b_\mu(x)\lambda^b\Big) \tag{2.30}$$

where a_μ stands for either the spatial or temporal lattice spacing, depending on the value of μ. This definition is an approximation to the path-ordered, straight Wilson line $\mathcal{P}\exp(ig\int_x^y A)$ connecting adjacent lattice points x and y. The relation becomes exact in the limit of vanishing lattice spacings (the naive continuum limit) $a_\mu \to 0$. It is assumed throughout this work that the lattice spacing is sufficiently small for this approximation to be valid.

A continuum gauge transformation as defined in Eq. (2.2) acts on the links according to

$$U_\mu(x) \mapsto G(x)U_\mu(x)G^\dagger(x+\hat{\mu}) \; . \tag{2.31}$$

Thus it is obvious that gauge-invariant quantities can be constructed by taking the trace of products of link variables around a closed loop. The smallest such product is the plaquette which is defined as

$$U_{\mu\nu}(x) := U_\mu(x)U_\nu(x+\hat{\mu})U^\dagger_\mu(x+\hat{\nu})U^\dagger_\nu(x) \; . \tag{2.32}$$

The plaquette is related to the field strength according to[9]

$$U_{\mu\nu}(x) = \exp(iga_\mu a_\nu(\mathcal{F}_{\mu\nu}(x) + \mathcal{O}(a_s))) \; . \tag{2.33}$$

Using plaquettes a gauge-invariant lattice action approximating the integral over (2.8) is given by the Wilson action

$$S = \frac{2\mathrm{N}}{g^2}\sum_x\Big\{\frac{a_s}{a_\mathrm{t}}\sum_j\Big[1-\frac{1}{2\mathrm{N}}\Big(\mathrm{Tr}U_{0j}(x)+\mathrm{Tr}U^\dagger_{0j}(x)\Big)\Big] \; - \; \frac{a_\mathrm{t}}{a_s}\sum_{j<k}\Big[1-\frac{1}{2\mathrm{N}}\Big(\mathrm{Tr}U_{jk}(x)+\mathrm{Tr}U^\dagger_{jk}(x)\Big)\Big]\Big\} \tag{2.34}$$

for SU(N)- Yang-Mills theory. Note the relative minus sign between the kinetic and potential energy term in Eq. (2.34). This differs from the familiar expression in equilibrium studies because

[9] When estimating the discretisation error in Eq. (2.33) we assume that the ratio a_t/a_s is kept fixed.

we need to consider the action in Minkowski rather than Euclidean spacetime for the present objective of real-time computations. For SU(2) lattice gauge theory the trace of all plaquettes variable is real[10], *i.e.* $\mathrm{Tr}U \in \mathbb{R}$. Thus the lattice action Eq. (2.34) can be written in a slightly simpler way as

$$S = \frac{4}{g^2}\sum_x \Big\{ \frac{a_s}{a_\mathrm{t}} \sum_j \Big[1 - \frac{1}{2}\,\mathrm{Tr}U_{0j}(x)\Big] \;-\; \frac{a_\mathrm{t}}{a_s}\sum_{j<k}\Big[1 - \frac{1}{2}\,\mathrm{Tr}U_{jk}(x)\Big]\Big\} \tag{2.35}$$

in this particular case.

The structure of many equations can be rendered more instructive introducing electric and magnetic fields. In the continuum, the latter can be read off from the field strength tensor as in electrodynamics [89]. In order to establish the notion of electric and magnetic fields on the lattice, one can start from the relation (2.33) between the plaquette and the fields strengths and expand the exponential. This yields

$$\mathcal{F}^a_{\mu\nu}(x) = \frac{-i}{g a_\mu a_\nu}\,\mathrm{Tr}(\sigma^a U_{\mu\nu}(x)) + O(a_\mu) \tag{2.36}$$

and hence at leading order in the lattice spacing

$$\begin{aligned} E^a_j(x) &= \frac{-i}{g a_\mathrm{t} a_s}\,\mathrm{Tr}(\sigma^a U_{0j}(x)) \\ B^a_j(x) &= -\frac{1}{2}\,\epsilon_{jkl}\mathcal{F}^{kl}(x) = \frac{i}{2ga_s^2}\,\epsilon_{jkl}\mathrm{Tr}(\sigma^a U_{kl}(x))\;. \end{aligned} \tag{2.37}$$

The gauge invariant quantities $\mathrm{Tr}(\mathbf{E}^2)$ and $\mathrm{Tr}(\mathbf{B}^2)$ can be computed directly from a plaquette's trace as used in the lattice action (2.34).

Having introduced these pieces of notation, we follow [9] to derive the equations of motion for the discretised theory defined through Eq. (2.35). We specialise to SU(2) Yang-Mills theory but apart from using particular properties of SU(2)- matrices the procedure is completely analogous for higher N [38, 80]. Before we commence the derivation, we fix the gauge by requiring that the gauge field satisfy the temporal axial gauge condition

$$A_0 \equiv 0\;, \tag{2.38}$$

which implies

$$U_0 \equiv \mathbb{1} \tag{2.39}$$

in the lattice formulation by virtue of Eq. (2.30). The lattice action (2.35) can be varied w. r. t. to a

[10]This can be seen easily from the decomposition Eq. (B.3) in the Appendix B.

spatial link $U_j(x)$ by making the replacement $U_j(x) \mapsto (\mathbb{1} + i\epsilon\sigma^a)U_j(x)$ (this implies the variation $U_j^\dagger(x) \mapsto U_j^\dagger(x)(\mathbb{1} - i\epsilon\sigma^a)$). The stationarity requirement

$$\frac{\delta S}{\delta U_j(x)} \stackrel{!}{=} 0 \tag{2.40}$$

then yields the equation of motion

$$\begin{aligned} E_j^a(x) = E_j^a(x - \hat{t}) + \frac{i\,a_\mathrm{t}}{g a_s^3} \sum_{k\neq j} \Big[& \operatorname{Tr}(\sigma^a U_j(x) U_k(x+\hat{j}) U_j^\dagger(x+\hat{k}) U_k^\dagger(x)) \\ & + \operatorname{Tr}(\sigma^a U_j(x) U_k^\dagger(x+\hat{j}-\hat{k}) U_j^\dagger(x-\hat{k}) U_k(x-\hat{k})) \Big] \\ = E_j^a(x - \hat{t}) + \frac{i\,a_\mathrm{t}}{g a_s^3} \sum_{k\neq j} \Big[& \operatorname{Tr}(\sigma^a U_{jk}(x)) + \operatorname{Tr}(\sigma^a U_{j(-k)}(x)) \Big] \end{aligned} \tag{2.41}$$

where we have identified electric fields using Eq. (2.37). Provided a configuration of links on a spatial time-slice and electric fields at time $t - a_\mathrm{t}$, one can propagate the electric field forward in time by one unit of a_t. Applying Eq. (2.33) to a plaquette with time-like links gives

$$U_{0j}(t, \mathbf{x}) = \exp(i g a_\mathrm{t} a_s E_j(t, \mathbf{x})) = U_j(t + a_\mathrm{t}, \mathbf{x}) U_j^\dagger(t, \mathbf{x}) \tag{2.42}$$

in temporal axial gauge. Multiplying the latter identity from the right by $U_j^\dagger(t, \mathbf{x})$ and employing the common representation of SU(2) matrices in Eq. (B.3), the link variables at the subsequent time-slice can be computed according to[11]

$$U_j(t + a_\mathrm{t}, \mathbf{x}) = \left(\sqrt{1 - \frac{1}{2}\operatorname{Tr}(E_j(t, \mathbf{x}) \cdot E_j(t, \mathbf{x}))}\; \mathbb{1} + i g a_\mathrm{t} a_s E_j^a(t, \mathbf{x}) \frac{\sigma^a}{2} \right) U_j(t, \mathbf{x}) \,. \tag{2.43}$$

In deriving Eq. (2.43) we have tacitly opted to take the positive root appearing in (B.4). This is justified if the lattice spacing is sufficiently small to ensure that one is in the proximity of the continuum limit, which in turn implies that all link variables lie in the vicinity of $\mathbb{1} \in \mathrm{SU}(2)$.

Varying the action (2.34) with respect to a temporal link (The variation is not constrained by

[11] Note that there is no approximation involved here in the computation of $U_{0j}(t, \mathbf{x})$. Computing the electric fields from Eq. (2.37) in fact yields the expansion coefficients of the plaquette according to the decomposition (B.3). In Eq. (2.43) we do nothing but rebuilding the plaquette from those coefficients. The symbol E should be understood to denote the 'logarithm' of the plaquette in this context which coincides with the electric field at leading order in the lattice spacing, as stated in (2.37). Also note that there is no summation over the index j in Eq. (2.43).

the gauge condition (2.39).) yields the set of equations

$$\sum_{j=1}^{3}\Big[\mathrm{Tr}\Big(\sigma^a U_{0j}(x)\Big) \;-\; \mathrm{Tr}\Big(\sigma^a U_j^\dagger(x-\hat{j})U_{0j}(x-\hat{j})U_j(x-\hat{j})\Big)\Big] = 0 \tag{2.44}$$

which hold for all x and a. Eq. (2.44) is the discretised version of the Gauss constraint (2.12) in temporal axial gauge. Physically meaningful initial conditions need to satisfy (2.44). Despite being exactly conserved in the continuum theory, the Gauss constraint (2.44) will be violated during the course of a numerical simulation due to rounding and discretisation errors. The magnitude of these departures from the constraint manifold has to be monitored and one has to ensure that they remain sufficiently small.

Equipped with an algorithm to solve the classical equations of motion the classical-statistical approximation requires to solve these field equations for a sample of initial conditions generated from the initial density matrix ρ_0 in Eq. (2.17). We rewrite this in terms of an initial phase-space density[12] $P_0[A, E]$ in the space of all possible field configurations at initial time. The expectation value of a quantity $O(t)$ is computed in the classical-statistical approximation from the functional integral

$$\langle O\rangle_t = \int \mathcal{D}A\mathcal{D}E\, P_0[A,E]\, O(t)\;. \tag{2.45}$$

If not stated otherwise, $\langle \ldots \rangle$ is to be understood in terms of P_0. In practice, the functional integral in (2.45) is rendered finite-dimensional by the lattice discretisation in combination with periodic boundary conditions. The resulting high-dimensional integral is then computed as the average over a finite number of initial configurations which are sampled by a Monte Carlo procedure.

An expression for the energy density in the present discretisation scheme is given by

$$\epsilon(x) = \frac{2N}{g^2 a_s^4}\Big\{\sum_{j<k}\Big[1-\frac{1}{2N}\Big(\mathrm{Tr}\,U_{jk}(x)+\mathrm{Tr}\,U_{jk}^\dagger(x)\Big)\Big] \;+\; \Big(\frac{a_s}{a_t}\Big)^2\;\sum_j\Big[1-\frac{1}{2N}\Big(\mathrm{Tr}\,U_{0j}(x)+\mathrm{Tr}\,U_{0j}^\dagger(x)\Big)\Big]\Big\}\;. \tag{2.46}$$

This can be inferred from the Hamiltonian density [93] corresponding to the discretised Lagrangian in the limit $a_t \to 0$. Note that Eq. (2.46) reduces to the familiar

$$\epsilon(x) = \frac{1}{2}\sum_{j,a}\Big((E_j^a(x))^2 + (B_j^a(x))^2\Big)$$

[12] Note that $\mathbf{E} = -\dot{\mathbf{A}}$ is directly related to the canonical momentum conjugate to $\mathbf{A}$ in temporal axial gauge.

in the continuum limit. We denote the spatial average at a fixed instant of time t by

$$\epsilon(t) := \frac{a_s^3}{V} \sum_{\mathbf{x}} \epsilon(t, \mathbf{x}) \,, \tag{2.47}$$

where V denotes the volume of the system. Of course, $\epsilon(t)$ is a conserved quantity under the time evolution in the limit of $a_t \to 0$, which - together with the preservation of the Gauss constraint (2.44) - provides a stringent test for the numerical implementation.

Because it is natural to store numbers measured in units of the spatial lattice spacing on the computer we introduce an extra notation for dimensionless quantities. The dimensionless lattice gauge field is defined as[13]

$$\hat{A}_j := g a_s A_j \equiv \hat{A}_j^a \lambda^b \tag{2.48}$$

which allows to write link variables (2.30) as $U_j = e^{i\hat{A}_j}$. Similarly, we introduce a dimensionless field strength through

$$\hat{\mathcal{F}}_{\mu\nu} := g a_\mu a_\nu \mathcal{F}_{\mu\nu} \equiv \hat{\mathcal{F}}_{\mu\nu}^a \lambda^b \tag{2.49}$$

implying analogous formulae for dimensionless electric and magnetic fields $\hat{E}_j$ and $\hat{B}_j$, respectively. The energy density (2.46) is represented on the lattice by the dimensionless $\hat{\epsilon}$ defined by virtue of

$$\hat{\epsilon} := g^2 a_s^4 \epsilon \,. \tag{2.50}$$

It is obvious that a given simulation, which is implemented on the computer entirely in terms of $\hat{A}$ and $\hat{E}$, can represent various physical situations depending on the values of g, a_s and a_t. We infer from Eq. (2.48) that we can compensate a global factor in either of g, a_s or $\hat{A}$ by rescaling any of the other quantities with the respectice reciprocal. That is, the same numerical solution can represent different gauge field configurations at correspondingly different couplings or lattice spacings. Fixing this ambiguity (*i.e.* setting the scale) will be discussed in Section 3.1. This is of course a crucial issue when relating the outcome of the numerical simulations to heavy ion collision experiments.

For several applications it is desirable to compute the gauge field A_μ^a from the link variables, that is to invert Eq. (2.30). For instance, this will be required in Chapter 4, where properties of the Green function (2.22) will be investigated by means of the classical-statistical approximation. For general SU(N), Eq. (2.30) cannot be inverted analytically. In general, the definition of gauge fields is ambiguous[14] for finite a_s but all definitions have to agree in the continuum limit. In the

[13] Since we choose to work in temporal axial gauge (2.14) we specialise to spatial gauge field components here.
[14] Recent work on this issue can be found in [153], for instance.

case of SU(2) gauge theory Eq. (2.30) can indeed be inverted exactly yielding[15]

$$\hat{A}^b_\mu = -i\frac{\arccos(\frac{1}{2}\mathrm{Tr}\, U_\mu)}{\sin(\arccos(\frac{1}{2}\mathrm{Tr}\, U_\mu))}\,\mathrm{Tr}\,(\sigma^b U_\mu)\,. \tag{2.51}$$

This can easily be derived using the formula $e^{i\,\mathbf{a}\cdot\sigma} = \cos(|\mathbf{a}|)\mathbb{1} + i\,\mathbf{a}\cdot\sigma\sin(|\mathbf{a}|)/|\mathbf{a}|$. For general SU(N), the relation (2.30) cannot be solved for $\hat{A}^b_\mu$, though. A useful approximation is to compute $\hat{A}^b_\mu$ at leading order according to

$$\hat{A}^b_\mu \simeq -2i\,\mathrm{Tr}\,(\lambda^b U_\mu)\,, \tag{2.52}$$

which reads

$$\hat{A}^b_\mu \simeq -i\,\mathrm{Tr}\,(\sigma^b U_\mu) \tag{2.53}$$

for SU(2). Note from Eq. (2.30) that the approximation (2.53) to Eq. (2.51) becomes exact in either of the three limits $g \to 0$, $a_s \to 0$, and $|A| \to 0$ while keeping the other two quantities fixed. In practice, employing (2.52) does not represent a severe restriction because one needs to take the continuum limit $a_s \to 0$ at the end of the calculation anyway. Moreover, the definition of the link variable (2.30) already involves an approximation, as discussed in that context. Thus the computation of gauge fields from lattice configurations can only be considered meaningful if the difference in the results obtained from Eqns. (2.51) and (2.52) is negligible.

We close this section by mentioning another property of the Yang-Mills equations (2.11). Namely, classical solutions for different values of the gauge coupling $g > 0$ can be obtained once a solution is available for a fixed value which, without loss of generality, can be taken as $g = 1$. This can be seen as follows. Denote the classical Yang-Mills action (2.8) for a certain value of g by $S_g[A]$. The Lagrangian density contains three kinds of terms namely A^2, gA^3 and g^2A^4. Inserting a trivial factor of $1 = g^2/g^2$ shows that $A^2 + gA^3 + g^2A^4 = g^{-2}\{(gA)^2 + (gA)^3 + (gA)^4\}$ and thus pulling out a factor g^{-2} from the action integral directly shows that $S_g[A] = g^{-2}S_1[(gA)]$. The classical solutions are the stationary points (field configurations) of the action and thus $S_g[A]$ is stationary if and only if $S_1[(gA)]$ is so. That is, we can construct a solution for $0 < g \neq 1$ by first solving the Yang-Mills equations for $g = 1$ and than replacing the solution according to $A \mapsto A/g$. We emphasise that the full quantum theory does not possess this property. There, the value of g has an immediate impact on the probability amplitude e^{iS} in the path integral.

[15] This allows for the computation of the physical gauge field via definition (2.48).

Chapter 3

Plasma instabilities

In this chapter we will explore the physics of QCD- plasma instabilities and study their impact on the early stages of the thermalisation process in relativistic heavy ion collisions. As outlined in the Introduction, the central question here is to investigate if plasma instabilities can account for the apparent rapid isotropization of the gluonic medium within a time of $1 - 2$ fm/c.

There are strong arguments that the initial distribution of colour-charge carriers shortly after ($\sim$ 0.2 fm/c) a relativistic heavy ion collision is strongly anisotropic in momentum space (Cf. [16, 18] and references therein). This anisotropy is such that parton momenta in the central collision region are predominantly aligned in the plane perpendicular to the beam axis. In the case of electrodynamic plasmas it has been known for a long time that an anisotropic momentum distribution of charge carriers causes certain modes of the gauge field to be unstable, *i.e.* their amplitude grows exponentially in time [154]. It has been shown in the framework of hard-loop approaches that the same phenomenon occurs in a non-Abelian gauge theory [16, 50, 120, 141]. This has toppled the formerly accepted scenario of bottom-up thermalisation [25]. This kind of instability is referred to as Weibel or chromo-Weibel instability in the electrodynamic case and the QCD case, respectively. Recently, it has been suggested [74–76] that the Nielsen-Olesen instability [59, 129, 147], which does not possess a counterpart in electrodynamics, might also be relevant to the understanding of the quark gluon plasma dynamics. In general, plasma instabilities occur if the dispersion allows for an imaginary part with positive and negative sign.

QCD plasma instabilities of the chromo-Weibel kind and their significance for collider experiments have been investigated in numerous studies by both analytical as well as numerical means. Most works have employed the hard-loop effective action approach [15–21, 51, 134, 141] and in the framework of Wong-Yang-Mills equations [72, 73, 149]. These approaches assume a separation of scales between 'hard' momentum scale of the charge carriers and the 'soft' scale of the unstable gauge field modes. While providing a theoretically clear-cut scenario the sepa-

ration of scales might not be realised very well in an actual heavy ion collision. Moreover, the numerical studies in the hard-loop approach can only reliably follow the time evolution for very short times. They do not include the backreaction from the exponentially growing gauge fields onto the charge carriers and thus energy is not conserved. It has also proven difficult to convert the results into physical numbers and hence to establish contact to experiment. The simulations based on the Wong-Yang-Mills equations have other shortcomings. For instance, they have to distinguish particle- like degrees of freedom with hard momenta from field-like soft ones. The explicit criterion for this distinction is to a large extent arbitrary.

Our approach is to study the real-time evolution of an out-of-equilibrium ensemble of non-Abelian gauge fields in the classical-statistical approximation without further matter fields or external sources. We employ a set of colour-glass like initial conditions. The anisotropy in the initial conditions is realised on the level of the Fourier spectrum of the gauge fields. The initial stress-energy-momentum tensor is strongly anisotropic and features an enhanced transverse and a diminished longitudinal pressure. Due to the self-interactions of the Yang-Mills fields this promises to invoke rich dynamics and intriguing effects. We consider a non-expanding system and for the sake of saving computational efforts we study SU(2) gauge theory in most of this work. Before the results presented in this chapter were published in [42] the authors of [142] have pursued a strategy that is similar in some regards. However, they do take into account the expansion of the system. In contrast to our setup they use colour charges on the light cone as sources for the gauge field and the initial Fourier spectrum of the latter is completely different from the one we employ. While their setup may capture a few aspects of a heavy ion collision slightly more precise we see it as an advantage of our approach that it does not try to incorporate all possible features of the experiment. Therefore it is cleaner to treat theoretically and it is less difficult to establish contact to other field theoretical methods.

In Section 3.1 we will propose Gaussian initial conditions for classical-statistical lattice simulations that are suitable for the study of the early thermalisation process in heavy ion collision experiments. In Section 3.2 we present the results of our numerical simulations. It will turn out that there are two kinds of instabilities. Following the initial exponential growth in low-momentum modes a second kind of instabilities emerges (“secondary instabilities”, as opposed to the initial “primary instabilities”). Employing 2PI methods, we demonstrate that the secondary instabilities are induced by fluctuation effects. Subsequently, we determine the growth rates of both kinds of plasma instabilities. This constitutes a central part of this work because it allows to draw conclusion regarding the significance of instabilities for the thermalisation process in current and future collider experiments, for example at RHIC, LHC, and FAIR. A straightforward and important question is to what extent the present findings can be extrapolated from SU(2)

Yang-Mills theory to the gauge group of QCD, that is SU(3). This has been investigated in an accompanying thesis [38, 80] and we report on the outcome in Section 3.3. It turns out that the restriction to SU(2) is not severe and that the extrapolation to SU(3) can be done by a simple rescaling procedure. In Section 3.4 we investigate whether we are confronted with instabilities of the chromo-Weibel or Nielsen-Olesen type. Finally, we discuss the implications of our results regarding heavy ion collision experiments in Section 3.5.

3.1 Anisotropic initial conditions

In this section we propose the initial conditions that will subsequently be used in our numerical simulations.

We consider a head-on collision of two heavy ions at relativistic energies as sketched in Fig. 1.2. For the sake of definiteness we choose a Cartesian coordinate system such that the collision axis coincides with the z- axis. The x- and y- axes span the plane transverse to the collision axis. We assume that the medium is symmetric (in the ensemble average) under rotations about the z- axis. The partons that remain in the central rapidity region after the collision can be described by a phase-space distribution that is highly anisotropic in momentum space with the majority of momenta lying in the transverse plane [18]. Suitable initial conditions should thus feature a corresponding anisotropy.

Because we intend to phrase our initial conditions in momentum space we need to summarise some basic relations. For a cubic lattice with periodic boundary conditions of N^3 sites the discrete momentum[1] can take the N^3- many values $\mathbf{p} = 2\pi N^{-1}(n_1, n_2, n_3)\cdot a_s^{-1}$ with each $n_j \in \{0, 1, ...N-1\}$. In line with our conventions from Section 2.3 we reserve the notation $\hat{\mathbf{p}} = a_s\cdot\mathbf{p}$ for the momentum as measured in units of the inverse spatial lattice spacing. The absolute value of a Fourier mode's discrete momentum is given as the square root of

$$\mathbf{p}^2 = \frac{4}{a_s^2}\sum_j \sin^2\Big(\frac{\pi n_j}{N}\Big)\,. \tag{3.1}$$

Working in temporal axial gauge (2.14) we initialise the gauge fields in momentum space by sampling from a distribution of the following shape:

$$\langle\, A_j^a(0,\mathbf{p})A_k^b(0,-\mathbf{p})\,\rangle \sim C\delta^{ab}\delta_{jk}\exp\Big\{-\frac{p_x^2+p_y^2}{2\Delta_x^2}-\frac{p_z^2}{2\Delta_z^2}\Big\}\,\delta(\dot{A}(t_0)) \tag{3.2}$$

[1] We do not distinguish between vectorial momentum and the wavevector of a mode, which is justified in natural units.

The δ- function in Eq. (3.2) implies that the derivatives of A^b_μ w. r. t. time vanish at initial time, *i.e.*

$$\frac{dA^b_j}{dt}\Big|_{t=0} = 0 \tag{3.3}$$

for all $\mathbf{x}$, j and b. In the temporal axial gauge this can be equivalently phrased as setting all electric fields to zero or setting all plaquettes involving a temporal links to $\mathbb{1} \in \mathrm{SU}(2)$. From Eq. (2.44) it is thus immediate that this choice of initial conditions satisfies the Gauss constraint. The initial phase space probability distribution appearing in Eq. (2.45) thus is of the form

$$P_0[A,E] \propto \delta^{ab}\delta_{jk} \exp\Big\{-\frac{p_x^2+p_y^2}{2\Delta_x^2} - \frac{p_z^2}{2\Delta_z^2}\Big\}\,\delta(E)\ . \tag{3.4}$$

Unless otherwise stated, all expectation values $\langle\,...\,\rangle$ in this work are defined as the classical-statistical average (2.45) with repsect to this initial distribution of classical field configurations.

Some additional specifications are required at this stage. The constants Δ_x and Δ_x allow to control the anisotropy and we will typically use $\Delta_x \gg \Delta_z$. In fact we will take Δ_z much smaller than the smallest lattice momentum so that our initial conditions are basically $\delta(p_z)-$ like in momentum space. We define

$$\hat{\Delta}_x := a_s \cdot \Delta_x \tag{3.5}$$

and we choose it to be much smaller than two. The latter represents the highest attainable value for a momentum aligned along one of the coordinate axes, as can be seen from Eq. (3.1). In this way it is ensured that at least at early times the high-momentum modes close to the lattice cutoff do not affect the dynamics. This is different from classical thermal equilibrium which is plagued by the Rayleigh-Jeans divergence. Of course, we will nevertheless ascertain that our numerical results are not invalidated by discretisation artefacts. This will be demonstrated in Section C.

Provided an initial gauge field configuration $A^b_j(t=0,\mathbf{p})$ we Fourier transform to position space and initialise the link variables according to (2.30). In using the latter relation we set $g=1$ and understand the gauge field as measured in units of a_s. The choice of g is further commented upon below.

Eq. (3.2) specifies the average absolute value of each of the gauge field's Fourier coefficients. However, this average value can be realised in infinitely many ways. We opt for a straightforward implementation of the average value by generating a real-valued $A^a_j(\mathbf{p})$ from a Gaussian centred about zero with the width

$$\exp\Big\{-\frac{1}{2}\Big(\frac{p_x^2+p_y^2}{2\Delta_x^2}+\frac{p_z^2}{2\Delta_z^2}\Big)\Big\}$$

(Note that there are two Gaussian functions involved which are *a priori* completely unrelated.). This is done for all j and a independently and then results in the desired, uncorrelated expectation values (3.2) of $|A^a_j(\mathbf{p})|^2$. We multiply the value of A^a_j generated in this way by a phase factor $e^{i\varphi}$

with φ sampled from the homogeneous distribution on $[0, 2\pi]$, however respecting the relation $A_j^a(-\mathbf{p}) = A_j(\mathbf{p})^*$. This ensures that $A(t, \mathbf{x})$ takes real values as required for obvious physical reasons. We note in passing that this procedure yields an ensemble which does not break the global colour symmetry, that is

$$\langle A_j^a \rangle = 0 \tag{3.6}$$

for all j and a. This follows from the homogeneous distribution of phases which implies $\langle A_j^b(t = 0, \mathbf{p}) \rangle = 0$ for all momenta $\mathbf{p}$. As a technical aside, we initialise modes whose average amplitude according to Eq. (3.2) would be below a certain, small numerical value by a noise whose amplitude is of the form $|A_{\text{noise}}|^2 \propto 1/|\mathbf{p}|$. The functional dependence is chosen such that it mimics the "quantum half" occurring in the relation between the occupation number and the gauge field propagator in the quantum theory [148] in the limit of high momenta. The purpose of this plateau is to avoid numerical artefacts that could arise if the initial value of a given mode $|A_j^b(\mathbf{p})|$ is so small that it is below machine precision. The noise plateau allows to prevent difficulties of this kind. We demonstrate in the Appendix C that physical results are not affected by the explicit value of the noise amplitude.

The constant of proportionality C appearing in Eq. (3.2) is fixed by the requirement that the average energy density (2.47) be the same in all initial ensemble members. In practice, this can only be implemented with finite precision. We deal with this issue in the following way. At the start of each simulation we generate a random gauge field configuration following the method described above. Generically, this configuration will produce an arbitrary value for the average energy density. We then multiply the gauge field at all $\mathbf{x}$ by a global factor[2] and again compute the energy. This we repeat iteratively until the average energy density agrees with the prescribed value within some small tolerance (Typically, we require the mismatch be less than one or two per cent.). In this way, we sample an out-of-equilibrium ensemble of fixed energy to a good precision.

A further remark needs to be made on the average energy density. Given that we phrase our initial conditions in continuum gauge fields (which also facilitates to establish a connection to continuum formalisms such as the colour glass condensate and the 2PI effective action) we need to be in a regime where the discretisation is close to the continuum limit. From Eq. (2.30), it can be seen that it is the limit of small lattice gauge fields and thus low energy densities (in lattice units) where this is realised [3]. Thus we choose the overall lattice energy density of the initial

[2]This is facilitated by the fact that the average energy density scales like $\epsilon \propto |A|^2$ in the regime that we analyse here. This relation does not hold for the initial conditions in Section (3.4) where the field strength is dominated by the commutator rather than the derivative terms.

[3]This is also discussed in [128].

conditions small (as compared to the saturation value of the magnetic contribution of $24\, g^{-2} a_s^{-4}$), typically of order $0.05\, g^{-2} a_s^{-4}$. Of course, the possibility to relate links and gauge fields is not only important when setting up initial conditions. Many computations that we are interested in will require to compute gauge fields from the links via Eq. (2.51) and thus rely on the proximity to the continuum limit.

Having described the functional form and the numerical implementation of our initial conditions we now turn to their physical interpretation and discuss to what extent they can be related to heavy ion collisions.

First, the convolution theorem implies that the gauge field spectrum in Eq. (3.2) is proportional to the Fourier representation of the equal-time correlation function $\langle\, A_j^a(t = 0, \mathbf{x})\, A_k^b(t = 0, \mathbf{0})\,\rangle$. From Eq. (3.6) it follows that this is equal to the connected correlation function for the initial conditions at hand and thus to the classical-statistical approximation for the statistical propagator (2.22). Due to the Gaussian nature of our initial conditions it is clear that all connected n- point functions vanish for $n > 2$. This facilitates to establish contact with other analytic schemes such as the hard-loop or 2PI effective action methods.

As stated in Eq. (3.2) in terms of the gauge fields in temporal axial gauge it is not immediately clear that our initial conditions indeed correspond to a situation that features a physical anisotropy for $\Delta_x \neq \Delta_z$. It is conceivable that no such anisotropy is present or that the gauge fields can be rendered isotropic by applying a suitable gauge transformation to (3.2). A numerical proof that there actually is a physical anisotropy introduced by the initial conditions (3.2) will be given in Section 3.2. There, it is explicitly shown that the stress-energy-momentum tensor at initial time is of the shape $T_{11} = T_{22} > 0$ while $T_{33} \simeq 0$ (Cf. Fig. 3.6). That is, the longitudinal pressure[4] vanishes while the transverse pressure is non-zero. Note that this is what one would naively attribute to a distribution of particles whose velocities are almost exclusively aligned perpendicular to the z- axis. Moreover, the vanishing longitudinal pressure is a typical feature of the colour glass condensate [94, 103] which inspires our initial conditions. In fact, the following argument easily shows that T_{33} should vanish when evaluated on the initial conditions Eq. (3.2). First, note from Eq. (3.3) that $\mathbf{E}(t = 0) \equiv 0$ so that only magnetic fields contribute to the energy-momentum tensor at at initial time. Since we set Δ_x to an intermediate lattice momentum and work in a regime where the amplitude of $\hat{A}$ is small, the main contribution to the field strength will arise from derivative terms associated with transverse momenta around Δ_x. $\Delta_z \to 0$ implies that derivatives w. r. t. z vanish. Then, for an arbitrary colour index a, $\langle\, |\, B_x^a\, |\,\rangle \simeq \langle\, |\, \partial_y A_z^a - \partial_z A_y^a\, |\,\rangle \simeq \langle\, |\, \partial_y A_z^a\, |\,\rangle$ and analogously $\langle\, |\, B_y^a\, |\,\rangle \simeq \langle\, |-\partial_x A_z^a\, |\,\rangle$ so that $\langle\, |B_y^a|\,\rangle \simeq \langle\, |B_x^a|\,\rangle$. On average, the magnetic

[4] We use the expressions 'longitudinal pressure' and 'transverse pressure as synonyms for T_{zz} and $(T_{xx} + T_{yy})/2$, respectively, as commonly done in the relevant literature.

field in z- direction takes the value $\langle\, |B_z^a| \,\rangle \simeq \langle\, |\partial_x A_y^a - \partial_y A_x^a| \,\rangle \simeq \langle\, |\sqrt{2} B_x^a| \,\rangle$ where the latter follows from the fact that the all A_j^a are sampled from independent but equal distributions. Hence we expect that at initial time

$$\begin{aligned}
\langle\, T_{11} \,\rangle &= \frac{1}{2} \sum_a \langle\, -(B_x^a)^2 + (B_y^a)^2 + (B_z^a)^2 \,\rangle \simeq \frac{1}{2} \langle\, \mathrm{Tr}\,((B_z)^2) \,\rangle \\
\langle\, T_{22} \,\rangle &= \frac{1}{2} \sum_a \langle\, +(B_x^a)^2 - (B_y^a)^2 + (B_z^a)^2 \,\rangle \simeq \frac{1}{2} \langle\, \mathrm{Tr}\,((B_z)^2) \,\rangle \\
&\text{while} \\
\langle\, T_{33} \,\rangle &= \frac{1}{2} \sum_a \langle\, +(B_x^a)^2 + (B_y^a)^2 - (B_z^a)^2 \,\rangle \simeq 0 \,.
\end{aligned} \tag{3.7}$$

Using Eq. (3.2) is also motivated by a quasi-particle picture. In the case of a weakly interacting scalar field φ it can easily be shown that the occupation number in momentum space is related to the field amplitude by $n(\mathbf{p}) \propto \omega(\mathbf{p})\,|\,\varphi(\mathbf{p})\,|^2$ where $\omega(\mathbf{p})$ is the dispersion relation of the theory (See *e.g.* [31].). In the case of interacting gauge theories the definition of particle numbers from A_μ is in general ambiguous [5] due to the possible gauge dependence of both $\omega(\mathbf{p})$ and $A_j(\mathbf{p})$. Thus, at least at high momentum where the perturbative picture is valid, the initial conditions in Eq. (3.2) can be thought of as representing a situation governed by particle-like degrees of freedom (partons) that predominantly populate the transverse degrees of freedom.

As outlined in Section 2.2 the classical-statistical approximation allows to follow the early time evolution of the full quantum system provided one starts from quantum initial configurations. Now, the canonical momentum conjugate to A_j is simply $E_j = -\dot{A}_j$ in the temporal axial gauge. Therefore, setting the time derivatives at $t = 0$ to zero as done in Eq. (3.3) seems to contradict the uncertainty relation. Therefore, it might appear that Eqns. (3.2) and (3.3) do not represent a valid set of quantum initial conditions. In a thesis related to the present work [26] initial conditions with $\dot{A} \neq 0$ were employed. No discernable differences were observed in the time evolution of physical quantities, which confirms the validity of the use of the initial conditions (3.2).

We now turn to discuss under which assumptions the above initial conditions can be related to collider experiments. The initial conditions (3.2) have been motivated to a large extent from the colour glass condensate. As discussed for instance in [87], the latter assumes weak coupling and high occupation numbers of the dominant low-momentum gluons that are hence subject to classical dynamics. Therefore, it is reasonable to neglect the quark degrees of freedom. All these

[5] A discussion of this issue can be found in [18].

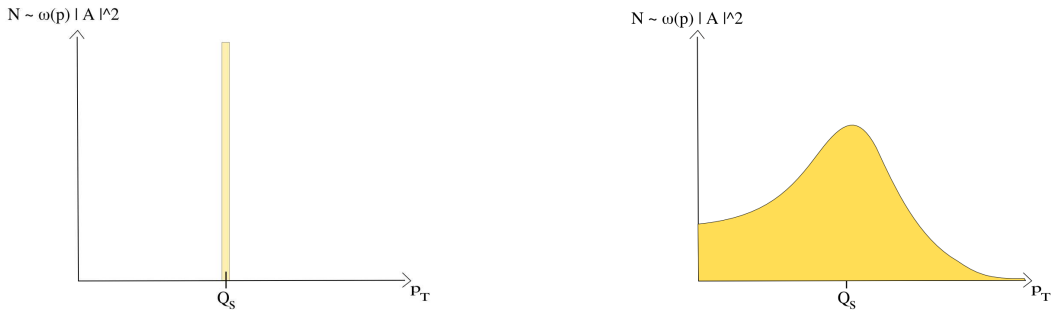

(a) (b)

Figure 3.1: Schematic comparison of the types of initial conditions (a) commonly used in simulations in the hard-loop framework and (b) in this work. The plot sketches the initial occupation numbers in both setups as a function of the transverse momentum p_T under the assumption of a generic dispersion relation $\omega^2(\mathbf{p}) = m_T^2 + \mathbf{p}^2$. Occupation numbers of longitudinal modes are small in both settings at initial time.

properties are consistent with our setup. The transverse width Δ_x in Eq. (3.2) corresponds to the saturation scale Q_s of the colour glass condensate.

On top of the assumptions made in the literature for the colour glass condensate, the interpretation of our results on plasma instabilities in the context of heavy ion collisions is based on two further prerequisites. First, we neglect the expansion of the system. This simplification is justified if the expansion rate is sufficiently small compared to the growth rate of the instabilities [16]. Since we have to determine the growth rates numerically first we can only check afterwards if they are compatible with this requirement. In any case, we cannot analyse the entire medium created in a heavy ion collision. Rather, we study the out-of-equilibrium plasma in a small box situated in the central region of the collision, as indicated by the rectangle in Fig. 1.2(b).

The second approximation that our approach is based upon is that the dynamics of QCD with its gauge group SU(3) can be well approximated by SU(2)- simulations. This was investigated in a related thesis employing SU(3) and it turned out that the only relevant difference is a controlled change in the time scale [38, 80]. These findings will be briefly summarised in Section 3.3.

In Fig. 3.1 we schematically compare our initial conditions for the transverse modes to the ones employed in simulations based on hard-loop simulations. Both approaches are characterised by a hard scale which is implemented in different ways, however. In the hard-loop approach sketched in Fig. 3.1(a) a clear separation of momentum scales is assumed. This is incorporated by the sharp, δ- like peak of the distribution containing the source of 'hard', particle-like degrees of freedom. Numerical simulations then allow to investigate possible instabilities in the 'soft', field-like modes for both transverse and longitudinal momenta. The hard particles are static in

Quantity	RHIC	LHC
ϵ	2 - 30 GeV/fm^3	$\gg \epsilon_{\mathrm{RHIC}}$
Q_s	1 - 2 GeV	2 - 3 GeV
g	1 - 2	1 - 2

Table 3.1: Estimates for the energy density ϵ, the saturation scale Q_S and the gauge coupling g in heavy ion collision experiments. The values of g have been computed from $\alpha_s = g^2/(4\pi)$ with the momentum scale set by Q_S. Note that $\alpha_s \sim 0.1$ for $g = 1$ which is therefore still in the weak-coupling regime. The values are taken from [84, 87, 130].

time, that is, the backreaction on them is neglected. In particular, the total energy is not conserved. Our setup, which is visualised in the right hand panel of Fig. 3.1, does not necessitate such a clear separation of scales. The hard scale is implemented as the width Δ_x of the Gaussian in Eq. (3.2). There are only field-like degrees of freedom as implied by the classical-statistical approximation. The backreaction is fully taken into account by the field equations in a natural way and energy is conserved up to controlled numerical errors. In contrast to the hard-loop setup our approach does not allow to study the behaviour of the purely transverse low-momentum modes because their Fourier coefficients are already large at the beginning. However, this is not too big a disadvantage because analytical studies predict the instabilities to affect mainly longitudinal modes [16, 76, 141] which are not (or only weakly) populated in either setup.

We now turn to the important issue on how results from the lattice computation are converted into predictions in physical units. The parameters that need to be fixed are the gauge coupling g and the spatial lattice spacing a_s. If these are known, all physical quantities can be computed from the configuration at hand. In our approach we consider the ensemble defined by Eq. (3.2) as the fundamental entity. Therefore, it is desirable to relate its free parameters to physical observables. These are the overall amplitude C, which we have traded for the average energy density ϵ, and the width Δ_x (Δ_z drops off the list of adjustable parameters because we are interested in the extreme anisotropy limit $\Delta_z \to 0$.). Together with g there are thus three free parameters in the simulation, two of which are dimensionful. From these we need to infer the physical values of g and a_s in order to make predictions in physical units. Obviously, this problem is over-determined so that there is some redundancy.

In thermal equilibrium lattice QCD there are well-established prescriptions to set the scale in a simulation. The basic approach is to compute a dimensionful quantity (*e.g.* the string tension, the Sommer radius or a pion or kaon decay constant) and match this to experimental input. Then high precision predictions for all other dimensionful observables can be made, provided the simulation is sufficiently close to the continuum limit.

	$g = 1$	$g = 2$
$\epsilon = 2\,\mathrm{GeV\,fm}^{-3}$	$a_s = 0.27$ fm $Q_S = 0.38$ GeV	$a_s = 0.19$ fm $Q_S = 0.53$ GeV
$\epsilon = 30\,\mathrm{GeV\,fm}^{-3}$	$a_s = 0.14$ fm $\Delta = 0.74$ GeV	$a_s = 0.10$ fm $Q_S = 1.05$ GeV

Table 3.2: Conversion of the lattice spacing to physical units for typical simulation parameters $\hat{\Delta}_x = 0.5$ and $\hat{\epsilon} = 0.05$ used in this work. g is taken from the running coupling and the energy density is matched to the extremal values quoted in [84].

For the out-of-equilibrium ensemble at hand we will pursue a similar strategy. However, we are faced with a few complications as compared to the equilibrium case. First, our initial conditions involve two dimensionful quantities (the energy density and the width) and there is no clear preference which one should be used to fix a_s. In contrast to the observables employed to set the scale in equilibrium lattice simulations, the available physical input for both ϵ and Δ_x is known only within rather larger error bands. Table 3.1 summarises data from the literature that can be used to set the scale for our initial conditions. Before doing so, some comments on the data are due. The low precision has already been mentioned. The values for the gauge coupling g are also problematic in another regard. They are taken from the one-loop running coupling as in standard textbooks for the case of QCD [130]. If this is to be employed to the present non-equilibrium initial conditions several uncertainties are introduced. Besides the fact that we deal with pure SU(2) gauge theory rather than with full QCD the scale at which the running coupling has to be evaluated is only known as an order of magnitude and given by either Q_s or $\epsilon^{1/4}$.

Due to these uncertainties we decide to fix the scale as follows. Reading off the value of g for the typical values of Q_s in Table 3.1 from [130] we assume a value for the gauge coupling in the range from 1 to 2. We then fix the lattice spacing by matching the (approximately fixed) lattice energy density $\hat{\epsilon}$ to input for ϵ from the literature as implied by Eq. (2.50), *i.e.*

$$a_s = \sqrt[4]{\frac{\hat{\epsilon}}{g^2\epsilon}}\,. \tag{3.8}$$

Note however that a_s depends only mildly on the exact value of ϵ because of the appearance of the fourth root. Obtaining a_s in this way we can compute the physical value of the width Δ_x from $\hat{\Delta}_x$ which should turn out be consistent with the colour glass condensate saturation scale Q_s that was assumed when estimating g. In Table 3.2 the resulting values for the lattice spacing are compiled together with Δ_x in physical units for the extremal choices of g and ϵ. By default, we will quote results for dimensionful quantities measured in units of appropriate powers of $\epsilon^{1/4}$

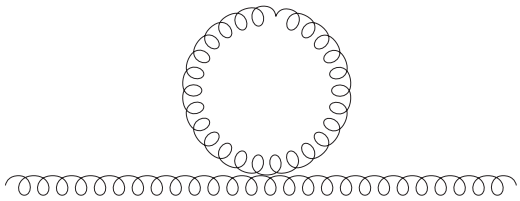

Figure 3.2: The tadpole diagram from which the mass scale in Eq. (3.9) can be computed.

using Eq. (3.8) in this work.

As explained above, our initial conditions (3.2) define the equal-time two-point function at $t = 0$. A mass scale is associated with this correlation function in a natural way through

$$m_T^2 := g^2 \int \frac{d^3p}{(2\pi)^3} \sum_{j,a} \langle\, |A_j^a(t=0,\mathbf{p})|^2 \,\rangle \,. \tag{3.9}$$

Diagrammatically, this corresponds to the contribution to the gluon self-energy from the tadpole diagram (Cf. Fig. 3.2.). Recalling that an occupation number can be introduced as $N(\mathbf{p}) \propto \omega(\mathbf{p}) \langle\, |A(\mathbf{p})|^2 \,\rangle$, one finds that Eq. (3.9) reproduces the familiar hard-loop result (cf. for instance [16, 49, 141]) whose integrand reads $N(\mathbf{p})/|\mathbf{p}|$ under the assumption that $\omega(\mathbf{p}) = |\mathbf{p}|$. There are a few caveats when comparing m_T to the mass scale of the hard-loop approach. First, the quantity defined in Eq. (3.9) will be gauge dependent[6]. The same is true for the dispersion relation and the presence of such a mass should invalidate the above assumption that $\omega(\mathbf{p}) = |\mathbf{p}|$ at least at low momentum. In this context it is important to emphasise that the occupation number for the hard, particle like degrees of freedom appears in the corresponding hard-loop definition of the mass scale. However, no clear distinction between hard and soft scales exists in our setup and Eq. (3.9) also receives contributions from the soft modes. Thus the analogy to the hard-loop scenario has to be taken with a grain of salt.

Because relating m_T to experimentally accessible quantities is problematic it cannot be used in a straightforward way to set the scale in the simulations, which is a disadvantage of the hard-loop approach. In spite of all this, m_T encodes viable information about the physics of the medium. It is directly proportional to g and together with the energy density ϵ - whose continuum expression would be given by a similar integral with an extra factor of $\omega(\mathbf{p})^2$ - it is sensitive to Δ_x. m_T turns out to be useful when relating simulations of SU(2)- and SU(3)- Yang-Mills theory [38, 80].

[6]The hard-thermal-loop self-energy however is gauge-invariant to one-loop order [49].

3.2 Dynamics of non-Abelian plasma instabilities

We now present numerical results of classical-statistical simulations solving the equations of motion (2.41) and (2.43) for the initial conditions (3.2). A summary of the simulation parameters and some technical details is given in Table 3.3.

Analytical studies predict the occurrence of instabilities from poles in the gluon propagator [16, 141]. Thus the instabilities should show up as exponential growth in the spatial Fourier transform $A^a_j(t, \mathbf{p})$ of the gauge field. The latter is straightforward to compute in our numerical simulations from Eq. (2.51) and subsequent Fourier transformation[7]. Actually, we compute the squared absolute value $|A^a_j(t, \mathbf{p})|^2 = A^a_j(t, \mathbf{p})A^a_j(t, -\mathbf{p})$ which is directly related to the equal-time statistical propagator (2.22) in the classical-statistical approximation by virtue of the convolution-/correlation theorem [133]. We choose the index j to correspond to a transverse direction. Fig. 3.3 shows the ratios

$$\frac{\langle \sum_a |A^a_j(t, \mathbf{p})|^2 \rangle}{\langle \sum_b |A^b_j(t = 0, \mathbf{p})|^2 \rangle} \text{ with } \hat{j} \perp \hat{z} \, , \mathbf{p} \parallel \hat{z} \tag{3.10}$$

plotted versus time. The quantity ξ indicated at the top of Fig. 3.3 is a measure for the bulk anisotropy of the configuration and it is defined as the ensemble average of

$$\xi(t) \equiv \log_{10} \left\{ \frac{\frac{1}{2} \sum_{\mathbf{p}} (p_x^2 + p_y^2) \left(\sum_{j=1}^3 \sum_{a=1}^3 |A^a_j(t, \mathbf{p})|^2 \right)}{\sum_{\mathbf{q}} q_z^2 \left(\sum_{k=1}^3 \sum_{b=1}^3 |A^b_k(t, \mathbf{q})|^2 \right)} \right\} . \tag{3.11}$$

The squared momenta appearing in this definition are computed from Eq. (3.1). The times when ξ takes particular values are indicated in Fig. 3.3 by dashed vertical lines. ξ vanishes when computed for an isotropic ensemble of gauge field configurations[8].

Now we turn to the physics content that can be inferred from Fig. 3.3. Plotted there is the ratio (3.10) as a function of time for three different momenta which exemplifying the typical behaviour of modes in the IR, intermediate and UV domain of the spectrum. All these momenta are aligned along the z- axis, which is the axis of anisotropy singled out by the initial conditions (3.2). Since the ordinate in Fig. 3.3 is logarithmic it is immediately obvious that there are low-momentum modes which grow exponentially from the beginning of the simulation thus confirming the occurrence of plasma instabilities. The zero mode, whose time evolution is not

[7] We have numerically checked that there is no discernible difference between gauge fields computed from Eqns. (2.51) and (2.52) for the initial configurations employed here.

[8] Note that $\xi(t)$ is gauge-dependent although we do not expect this dependency to be pronounced in a generic setup.

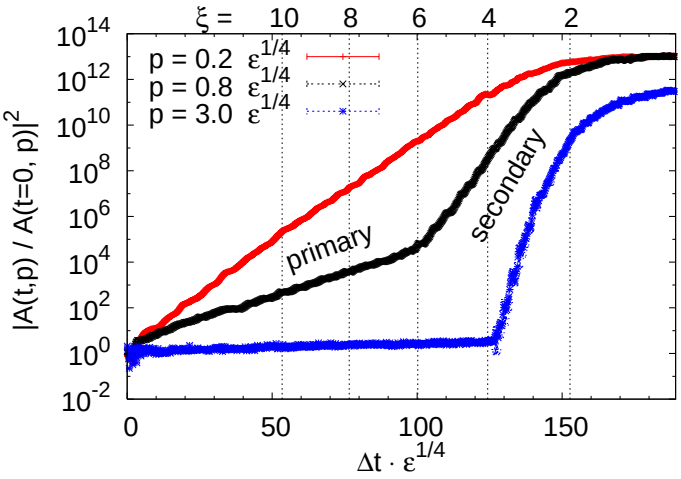

Figure 3.3: Exponential growth in the equal-time gauge field correlation function, *i.e.* $|A(t, \mathbf{p})|^2$. The curves correspond to the momenta from top to bottom. Confer the text for further explanation.

displayed in Fig. 3.3, does not exhibit exponential growth. Even if it featured an instability this would be disguised in our setup because the initial conditions (3.2) render the zero modes strongly populated in the beginning. We can infer that at least for non-zero p_z the growth rate is a decreasing function of the wave number. This will be analysed quantitatively at a later point.

Fig. 3.3 also shows that no exponential growth occurs in high-momentum modes at initial time, as exemplified by the blue, lowermost curve. However, the dynamics change qualitatively at a time $\Delta t \simeq 100\,\epsilon^{-1/4}$. Some of the low-momentum modes speed up their growth and also Fourier coefficients with higher wave numbers exhibit fast exponential growth. In order to distinguish this phenomenon from the initial instabilities we will refer to the latter as *primary* instabilities while the faster instabilities setting in at $\Delta t \simeq 100\,\epsilon^{-1/4}$ will be referred to as *secondary* instabilities henceforth. We note that the presence of two qualitatively different processes in the initial phase of violent growth is highly reminiscent to the case of parametric resonance in a scalar field investigated in [44] in the context of early universe preheating. This seems to be particularly surprising inasmuch as that both the dynamics (as encoded in the respective Lagrangians) as well as the initial conditions are completely different in these two cases.

Inspecting the values of the anisotropy parameter ξ as a function of time one sees that a substantial degree of anisotropy persists until shortly before saturation. Therefore, the use of field configurations up to times of approximately $100\,\epsilon^{-1/4}$ as initial conditions can be justified since there is no precise estimate available for the numerical value of ξ in a heavy ion collision. Hence we conclude that the simulation time Δt plotted on the abscissa is of no immediate physical

Quantity	Symbol	Value/setting
Lattice volume	N^3	64^3
Number of initial configurations/ensemble size	-	100
Transverse width	$\hat{\Delta}_x$	0.5
Longitudinal width	$\hat{\Delta}_z$	0.01
Average energy density	$\hat{\epsilon}$	0.05
Time step	a_t	$0.05\, a_s$
Gauge coupling	g	1

Table 3.3: Summary of the parameters of the numerical simulations presented in Chapter 3.

significance. The growth rates of the instabilities however do not change under shifting the initial time up to $\Delta t \simeq 100\,\epsilon^{-1/4}$. For this reason, the inverse growth rates have to be considered as the physically meaningful time scale that can be extracted from Fig. 3.3 and this is what we will focus upon in the following.

We learn from Fig. 3.3 that primary and secondary instabilities saturate at a time of approximately $150\,\epsilon^{-1/4}$. For the above reasons the this number has to be considered as physically meaningless without further specifications. The relevant time scale is given by the typical inverse growth rate of the plasma instabilities and we will present data for this below. At saturation time, the bulk anisotropy measure ξ is still non-zero and in fact testifies of a significant degree of anisotropy. This issue will also be elaborated upon later in the context of Fig. 3.7.

There are two obvious findings that are in disagreement with the results of hard-loop calculations. First, the hard-loop approximation predicts that in the limit of infinite anisotropy all modes aligned along the z- axis exhibit exponential growth from initial time on. Second, it is expected that the growth rate should monotonously increase with $|\mathbf{p}|$ rather than decrease. The authors of [76] have suggested that the instabilities arising from initial conditions of the kind (3.2) could be of the Nielsen-Olesen type rather than chromo-Weibel instabilities. This question will be addressed in Section 3.4.

In the hard-loop formalism, the gluon self-energy is gauge invariant in one-loop approximation and so are the predictions for dispersion relations and growth rates. Given that the hard-loop results are not in complete accordance with the above findings it has to be considered as unresolved at this point whether any effects in gauge invariant, physical quantities pertain to the instabilities observed in Fig. 3.3. The answer to this question is yes, as we demonstrate now. In analogy to [142] we compute the component T_{33} of the stress-energy-momentum tensor as a

function of t and $\mathbf{x}$. The equations for the spatial, diagonal components of $T_{\mu\nu}$ are given by

$$\begin{aligned}
T_{11}(x) &= \frac{1}{2}\sum_a \Big(-(E_1^a(x))^2 + (E_2^a(x))^2 + (E_3^a(x))^2\Big) \\
&\quad + \frac{4}{g^2 a_s^4}\Big[1 - \frac{1}{2}\Big(-\mathrm{Tr}\, U_{23}(x) + \mathrm{Tr}\, U_{13}(x) + \mathrm{Tr}\, U_{12}(x)\Big)\Big] \\
T_{22}(x) &= \frac{1}{2}\sum_a \Big(+(E_1^a(x))^2 - (E_2^a(x))^2 + (E_3^a(x))^2\Big) \\
&\quad + \frac{4}{g^2 a_s^4}\Big[1 - \frac{1}{2}\Big(+\mathrm{Tr}\, U_{23}(x) - \mathrm{Tr}\, U_{13}(x) + \mathrm{Tr}\, U_{12}(x)\Big)\Big] \\
T_{33}(x) &= \frac{1}{2}\sum_a \Big(+(E_1^a(x))^2 + (E_2^a(x))^2 - (E_3^a(x))^2\Big) \\
&\quad + \frac{4}{g^2 a_s^4}\Big[1 - \frac{1}{2}\Big(+\mathrm{Tr}\, U_{23}(x) + \mathrm{Tr}\, U_{13}(x) - \mathrm{Tr}\, U_{12}(x)\Big)\Big]\,,
\end{aligned} \tag{3.12}$$

where we have included the transverse components as well for future reference. This represents a straightforward adaption of the corresponding equations for Euclidean lattice simulations from [91] to Minkowski spacetime. Note that Eq. (3.12) coincides with the familiar result from electrodynamics [89] to leading order in ga^2 when electric and magnetic fields are identified according to Eq. (2.37). From Eqns. (3.12) and (2.37) it is immediately clear that the values of $T_{jj}(t, \mathbf{x})$ (no summation over j) are gauge invariant because they are computed from traces of plaquette variables. This also implies that the Fourier coefficients $T_{jj}(t, \mathbf{p})$ of these functions must be gauge invariant.

In thermal equilibrium, the expectation value of each T_{jj}, j fixed, would be equal to the thermodynamic pressure. Therefore, we will loosely refer to the diagonal components of T_{ij} as "the pressure" in the following even although this identification is valid only in thermal equilibrium, strictly speaking. Because the initial conditions (3.2) single out the z- axis, we will distinguish the "longitudinal pressure"

$$P_L(t, \mathbf{x}) := T_{33}(t, \mathbf{x}) \tag{3.13}$$

from the "transverse pressure"

$$P_T(t, \mathbf{x}) := \frac{1}{2}\Big(\, T_{11}(t, \mathbf{x}) + T_{22}(t, \mathbf{x})\,\Big)\,. \tag{3.14}$$

We have omitted the brackets $\langle ... \rangle$ for the expectation value on purpose in these definitions for the reason that we will frequently compute spatial Fourier transforms of these quantities. Since $\langle T_{ij}(t, \mathbf{x})\rangle$ cannot depend on $\mathbf{x}$ in a homogeneous system as considered here, this would produce trivial, vanishing results for all modes with non-zero momentum. On the contrary, the ensemble average of Fourier coefficients (or the absolute value thereof) with $\mathbf{p} \neq 0$ will generically be

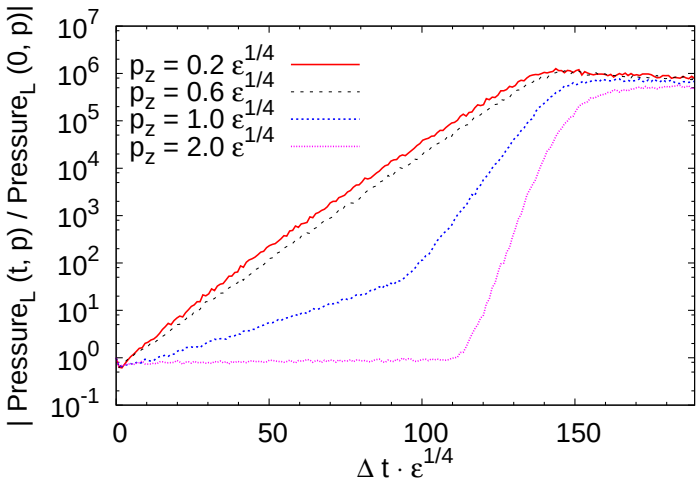

Figure 3.4: Plasma instabilities in a gauge invariant quantity. The order of the curves from top to bottom corresponds to the order of the momenta in the legend. The error bars are not shown because their size is too small to be resolved in this plot.

non-zero, reflecting the fact that the individual members of an ensemble need not be constant in space each. Hence, these quantities can serve as a measure for the average size of fluctuations in individual configurations and therefore they contain vital physical information.

Fig. 3.4 shows the time evolution of the ensemble-averaged Fourier coefficients of (3.13) for various spatial momenta of different modulus along the z- axis. Obviously, the emerging picture is very similar to the gauge field dynamics in Fig. 3.3. In particular, it proves that the instabilities observed in the level of the gauge field are not just a mere gauge artefact.

A different perspective on the physics of plasma instabilities is provided by Fig. 3.5. It shows the same quantity as Fig. 3.4 but instead of plotting T_{33} as a function of t for fixed wave vector snapshots of the T_{33}- spectrum as a function of p_z are shown for various instants of time. A band of low-momentum modes shows exponential growth at early times, reflecting the primary instabilities present in Figs. 3.3 and 3.4. At intermediate times, secondary instabilities occur in a broad range of modes. This is in qualitative agreement with the "UV cascade" or "avalanche" found in other approaches [18, 73].

Next, we focus on the issue of (overall) isotropization of the system. As discussed in the introduction, this is highly relevant to our understanding of the early stages of the thermalisation process in relativistic heavy ion collisions. It has already been revealed in Fig. 3.3 that the bulk anisotropy at the time of instability saturation is still substantial. Now we scrutinise this in more detail on the level of gauge invariant observables.

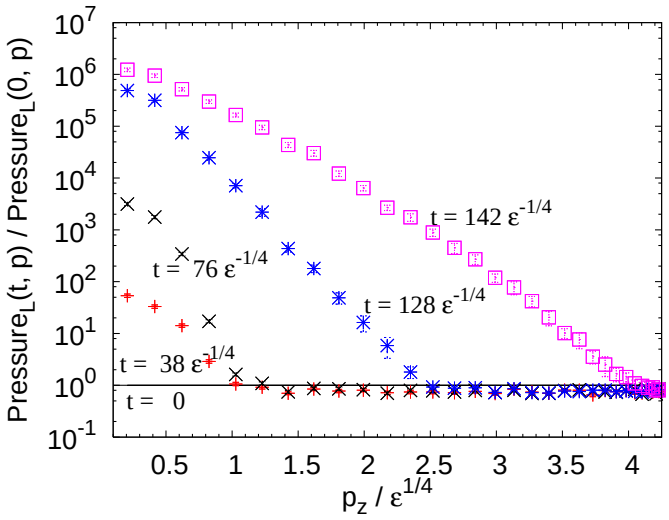

Figure 3.5: Snapshots of p_z- spectra of T_{33} at fixed time normalised to the respective values at $t = 0$.

First, we consider the time evolution of the longitudinal and transverse pressure. Their time evolution is shown in Fig. 3.6. Their values are normalised to the (spatial) trace of the stress-energy-momentum tensor so that both curves would be equal to $1/3$ in an isotropic situation[9]. Several things can be observed immediately. First, we note that the longitudinal pressure is close to zero at initial time. This proves that our initial conditions (3.2) formulated in terms of the gauge field indeed render the initial state anisotropic in a physically detectable way. Furthermore, with P_L approximately vanishing at $t = 0$ the initial ensemble (3.2) incorporates an important property of the colour glass condensate, as outlined in Section 3.1. The properties of the pressure at $t = 0$ are precisely those that one would intuitively expect for a system of particles whose momenta are aligned perpendicular to the z- axis.

Next, it is apparent from Fig. 3.6 that this anisotropy remains undiminished during the phase of exponential growth. It is only at the time of saturation of the plasma instabilities that a significant build-up of longitudinal pressure occurs. This can be understood on a qualitative level as follows. The field strength entering the expressions (3.12) for T_{ij} is dominated by derivative terms. The dominating contributions stem from Fourier modes with wave numbers of order $\Delta_x \simeq 1\,\epsilon^{1/4}$ and higher. These modes however either grow slowly or remain stable until the onset of the secondary instabilities. The quickly growing low-momentum modes on the other hand make only very small contributions to the derivatives of the gauge field. Hence the primary instabilities have almost no effect on the isotropization of the bulk pressure.

It is interesting to ask how long it takes the system to completely isotropize. The answer is

[9] We have checked that off-diagonal elements of T_{ij} are numerically small compared to the diagonal components.

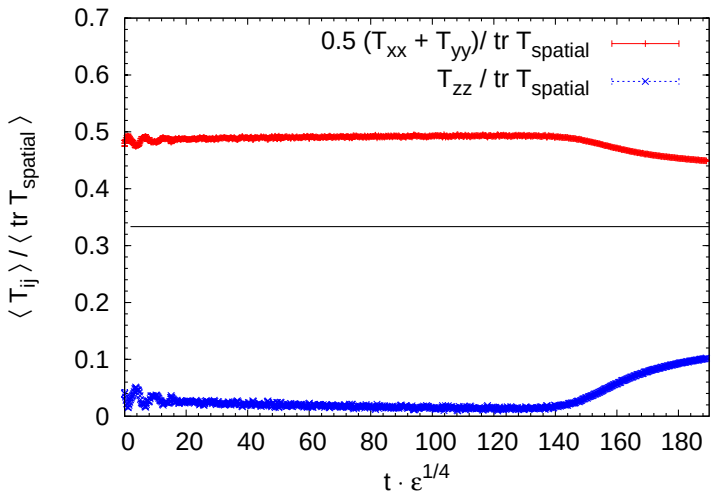

Figure 3.6: Time evolution of transverse and longitudinal pressure. The longitudinal pressure remains negligible compared to the transverse one for a long time. Since the pressure is gauge invariant this also demonstrates that the initial conditions (3.2) introduce a physically meaningful anisotropy at $t = 0$.

that P_L and P_T approach their equilibrium values only in an asymptotically slow fashion. From a single run (rather than a sample of initial conditions) on a smaller lattice we have found that this happens only at times of the order $5 \cdot 10^4 \, \epsilon^{-1/4}$. An isotropization within a margin of ten per cent occurs at times of the order of a few thousand $\epsilon^{-1/4}$ though. The quasi-stationary dynamics of this slow regime will be the subject matter of Chapter 4.

We have seen that instabilities cannot account for a quick overall isotropization of the plasma. The momentum dependence of the growth rates and the different behaviour of IR- and UV- modes suggests to study this issue in a more detailed way, however. To this aim, we consider ratios of Fourier coefficients which allow to measure the deviation from an isotropic state. In particular, we consider the expectation value of the ratio

$$\left| \frac{2\, T_{33}(t, \mathbf{p}_\parallel)}{T_{11}(t, \mathbf{p}_\perp) + T_{22}(t, \mathbf{p}_\perp)} \right| , \; |\mathbf{p}_\parallel| = |\mathbf{p}_\perp| = p \; . \tag{3.15}$$

It is intuitively clear that this ratio is one for all momenta in an isotropic state as *e.g.* thermal equilibrium[10]. That this is indeed the case is demonstrated by equilibrium calculations in

[10]Note that the order of the Fourier transformation and the ensemble average is crucial and cannot be interchanged. The ensemble average is translation invariant and hence all Fourier coefficients but the zero mode vanish. The ensemble average of the Fourier spectrum of ϵ or T_{33} provides a measure for the average amount of spatial fluctuation in those quantities.

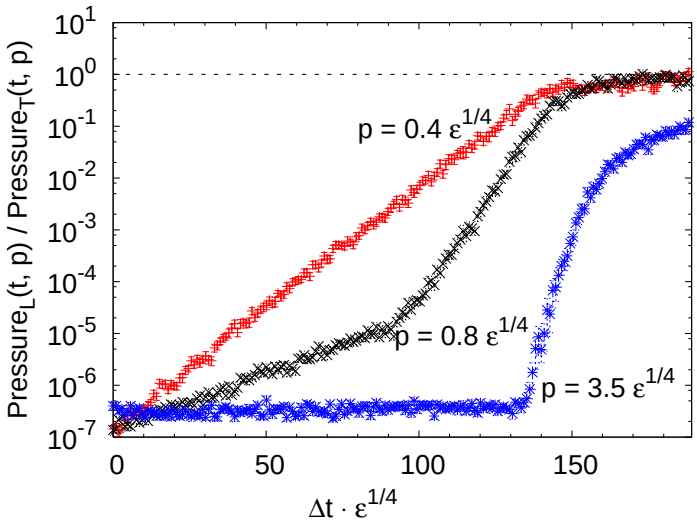

Figure 3.7: "Bottom-up isotropization": The ratio defined in Eq. (3.15) versus time for three different values of $|\mathbf{p}|$.

Appendix D. Alternatively, we can use a similar ratio constructed from the average Fourier transform of the local energy density (2.46),

$$\left|\frac{\epsilon(t,\mathbf{p}_{\parallel})}{\epsilon(t,\mathbf{p}_{\perp})}\right| = \left|\frac{\int d^3x\, e^{-i\mathbf{p}_{\parallel}\cdot\mathbf{x}}\,\epsilon(t,\mathbf{x})}{\int d^3x\, e^{-i\mathbf{p}_{\perp}\cdot\mathbf{x}}\,\epsilon(t,\mathbf{x})}\right| \quad , \; |\mathbf{p}_{\parallel}| = |\mathbf{p}_{\perp}| \,, \tag{3.16}$$

which has been employed in [38]. Results for (3.16) are compared to equilibrium simulations in Fig. D.3. We emphasise that both ratios are gauge invariant and thus probe the isotropization process in a physically meaningful fashion.

Fig. 3.7 shows the time evolution of the ratio (3.15) for three representative choices of p. We deduce from this figure that the instabilities do isotropize the low-momentum degrees of freedom. For not too big a momentum, the ratio (3.15) reaches its equilibrium value at the time of saturation. In contrast, the high-momentum modes do not isotropize as anticipated from the before discussion of Fig. 3.6. Actually, Fig. 3.7 is quite similar to Fig. 3.4 at first sight. This is because the time evolution of the ratio (3.15) is dominated by the fast exponential growth of the longitudinal modes in the numerator. The transverse Fourier coefficient in the denominator vary only slowly in time and thus do not have a perceivable effect on the time evolution.

We further quantify this observation by introducing the following criterion. We consider the system as isotropized for a momentum p if the ratio (3.15) is greater than 0.6 at $t = 160\,\epsilon^{-1/4}$ which corresponds approximately to the saturation time of the primary instabilities. Although these two numbers are chosen in a somewhat arbitrary way, they convey information about the

impact of the plasma instabilities nevertheless. Closely inspecting the data from our simulations we find that modes with momenta

$$p \lesssim 1.4\,\epsilon^{1/4} \tag{3.17}$$

fulfil the above isotropization criterion, which translates into

$$p \lesssim 1.0 \text{ GeV} \qquad (\epsilon_{\text{RHIC}} = 30 \text{ GeV/fm}^3\,,\ g = 1) \tag{3.18}$$

$$p \lesssim 0.4 \text{ GeV} \qquad (\epsilon_{\text{RHIC}} = 1 \text{ GeV/fm}^3\,,\ g = 1) \tag{3.19}$$

for the lower and upper bound on the energy density expected at RHIC. We remark that for $g = 2$ these values would be further increased by a factor of $\sqrt{2}$. Viscous hydrodynamics [106,139,140] provides an excellent description of elliptic flow as measured at RHIC up to transverse momenta of $2 - 2.5$ GeV. We note that this is in the same ballpark as (3.18).

The picture of isotropization on long length scales is further completed by the behaviour of spatial Wilson loops. A Wilson loop $W(R, \tilde{R})$ is the trace of a path-ordered product of links around a closed loop on the lattice which we assume to be a rectangle of size $R \times \tilde{R}$ here. In the vacuum the Wilson loop obeys an area law which means that

$$W(R, \tilde{R}) \sim e^{-\kappa R \tilde{R}} \tag{3.20}$$

for $R, \tilde{R} \to \infty$. κ is known as the string tension and governs the asymptotic decay of W for large areas. At non-zero temperature Wilson loops extending into a spatial and the temporal direction serve as an order parameter for the deconfinement phase transition. An area law of the kind (3.20) is obeyed in the confining phase. In the deconfining phase however, the asymptotic behaviour is given by a perimeter law instead. Spatial Wilson loops also follow an area law of the kind (3.20) up to temperatures well above the deconfinement transition [61, 107]. The coefficient κ is then referred to as the spatial string tension.

There is no obvious reason why spatial Wilson loops should obey an area law in our initial configurations. Due to the anisotropy it is to be expected that spatial Wilson loops with links in z- direction are qualitatively very different from purely transverse loops. In our simulations we have monitored the behaviour of these two kinds of spatial Wilson loops. The results are shown in Fig. 3.8 for three different times $0\,\epsilon^{-1/4}, 20\,\epsilon^{-1/4}$ and $160\,\epsilon^{-1/4}$ from left to right. The lower panel shows purely transverse Wilson loops as a function of area while the corresponding curves for Wilson loops involving longitudinal links are plotted in upper panels. Only the transverse loops follow an area law at early times while the longitudinal ones do not. At the time of saturation however, both kinds of loops exhibit an area law with the same spatial string tension to a very good accuracy. Since the asymptotic behaviour of the Wilson loop probes long range

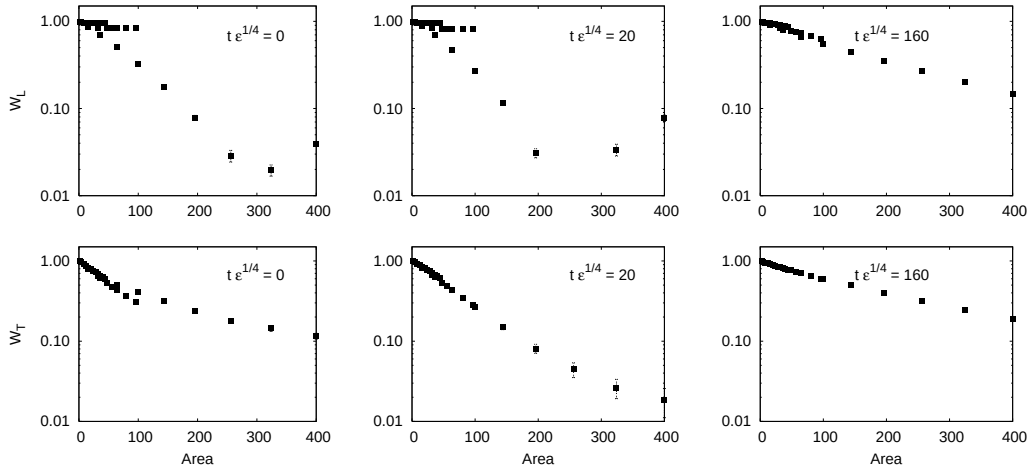

Figure 3.8: Values of spatial Wilson loops in the transverse plane (W_T) and Wilson loops including the longitudinal direction (W_L) as a function of the loop area in units of a_s. Shown are snapshots at increasing time going to the right. Initially, W_L exhibits no area law, while the transverse Wilson loop is characterised by a non-vanishing spatial string tension κ as explained in the text. One observes $W_L/W_T \simeq 1$ at the time of saturation of the exponential growth of gauge field fluctuations and the anisotropy is removed.

physics this result nicely supplements the before findings of isotropization on long length scales.

Particularly important for the issue of isotropization in the context of relativistic heavy ion collisions is the question of the time that is needed to reach an isotropic state. In order to answer this we determine the instability growth rates[11]. From the single-logarithmic plots in Figs. 3.3 and 3.4 it is clear that the unstable modes indeed grow exponentially with very high precision. We define $\gamma(p_z)$ as the growth rate of $|A(t,\mathbf{p})|^2\,, \mathbf{p} \parallel \hat{z}\,, |\mathbf{p}| = p_z$, *i.e.* $\mathbf{p} = (0,0,p_z)$. The motivation why we use $|A|^2$ rather than P_L is that the former can be related to the mode's occupation number, at least in a perturbative limit, which allows for a more direct comparison to earlier work [44] on parametric resonance in scalar fields.

We numerically determine $\gamma(p_z)$ by fitting a straight line to the logarithm of $|A(t,(0,0,p_z)|^2$ as a function of time for the corresponding value of p_z. For modes displaying both primary and secondary instabilities we fit both regimes individually, of course. We estimate the errors of γ by fitting the growth rate on a slightly smaller range. The difference between the two results is then used as an error estimate.

The results of fitting the data for $|A(t,\mathbf{p})|^2$ underlying Fig. 3.3 are presented in Fig. 3.9. In

[11] We recall that the amount of simulation time elapsed at saturation cannot be interpreted without further knowledge about the initial conditions in an actual heavy ion collision. Cf. the discussion on p. 41.

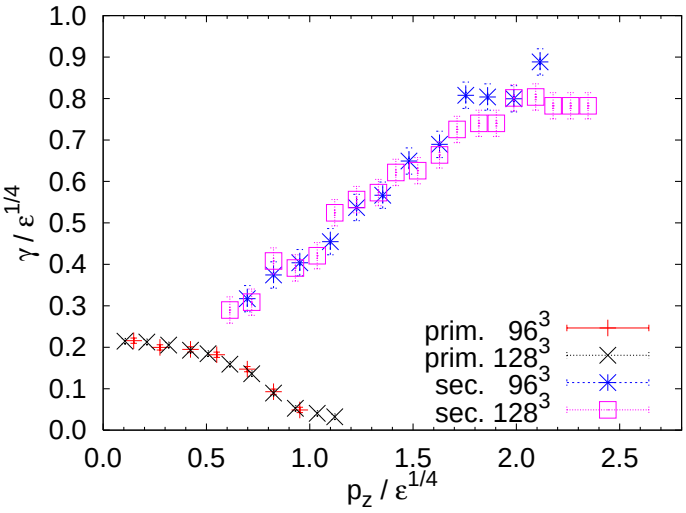

Figure 3.9: Growth rates of primary and secondary instabilities.

order to allow for a finer resolution of γ as a function of p_z we have also included results from simulations on 96^3 lattices but with otherwise identical simulation parameters. Several comments are due. First, the data for the primary growth rates looks qualitatively different from predictions of hard-loop calculations. In contrast to the latter, only a finite band of modes at low momenta is unstable. Moreover, $\gamma(p_z)$ does not vanish as $p_z \to 0$. When comparing the maximum primary to the maximum secondary growth rates the latter turns out to be three to four times as high as the former. In spite of this, the impact of the secondary instabilities on the dynamics could be reduced in a heavy ion collision because they set in much later than the primary instabilities.

In order to judge the impact that instabilities might have on the isotropization process we convert the maximum primary growth rate into physical units. Doing so as outlined in Section 3.1 for the same choices of parameters as used in Eq. (3.18) we obtain the inverse growth rates

$$\gamma^{-1}_{\text{max. pr.}} \simeq 1.1\,\text{fm/c} \qquad (\epsilon = 30\ \text{GeV/fm}^3 \quad , \quad g = 1) \tag{3.21}$$

$$\gamma^{-1}_{\text{max. pr.}} \simeq 2.7\text{fm/c} \qquad (\epsilon = 1\ \text{GeV/fm}^3 \quad , \quad g = 1)\,. \tag{3.22}$$

These are the relevant time scales for the isotropization process. For $g = 2$, which can still be considered as realistic, the growth rates would turn out faster by a factor of $\sqrt{2}$ and their inverses would be accordingly lower. In order for the instability to have a perceivable effect a time of multiple inverse growth rates has to elapse so that a few e- foldings can take place. Comparing this to the constraint set by the onset of hydrodynamical evolution, $\tau \sim 1 - 2\,\text{fm/c}$, we infer that plasma instabilities can potentially have an effect if the initial energy density is close to the upper estimate from the literature. Furthermore, we conclude that the effects of plasma instabilities may

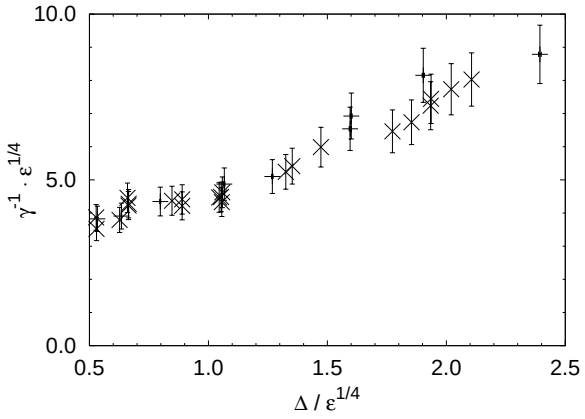

Figure 3.10: Fastest primary growth rates as a function of $\Delta_x/\epsilon^{1/4}$ for $g = 1$.

be more pronounced at the future LHC experiments which ought to create a quark gluon plasma at higher energy densities than RHIC.

When fitting growth rates to $P_L(t, \mathbf{p})$ it turns out that the results for identical momenta are exactly half as large. This can be understood from the momentum space structure of our initial conditions (3.2). Focusing on the magnetic contributions we see that the dominant contributions to T_{33} are of the kind $T_{33} \sim B^2 \sim (\partial A)^2$. Being a product of two ∂A's in $\mathbf{x}$- space, the Fourier transform of T_{33} can be obtained by a convolution in momentum space and thus is of the shape $T_{33}(t, \mathbf{p}) \sim \sum_{\mathbf{q}} A(t, \mathbf{q})A(t, \mathbf{p} - \mathbf{q})$, where we have ignored the derivatives for the sake of clarity. In the above analysis (and in particular for Fig. (3.4)) we have computed this for $\mathbf{p}$ parallel to the z-axis. Now, the initial conditions (3.2) are dominated by purely transverse modes $\mathbf{k} \perp \hat{z}$ due to the narrow width Δ_z. Despite the instabilities, the initial shape of the gauge field's Fourier transform is prevalent for some time. Thus those contributions dominate the above convolution for which $\mathbf{p} - \mathbf{q}$ is transverse. However, these modes are already strongly populated in the beginning and so do not exhibit exponential growth. Therefore, $T_{33}(t, \mathbf{p})$ is dominated by terms containing exactly one unstable factor. Thus the corresponding growth rate is exactly half the growth rate of the respective mode of A_j. This completes the argument.

In Fig. 3.10 we have plotted the inverse of maximum primary growth rate for simulations carried out with different ϵ and/or Δ_x. We note that also for different realisations of the same $\Delta_x/\epsilon^{1/4}$ the associated time scales are found to agree within the margins of error and that their dependence on the simulation parameters is rather simple.

Fig. 3.11 shows the outcome of a simulation employing initial conditions different from the ones that have been underlying the data presented thus far. Instead of choosing the longitudinal

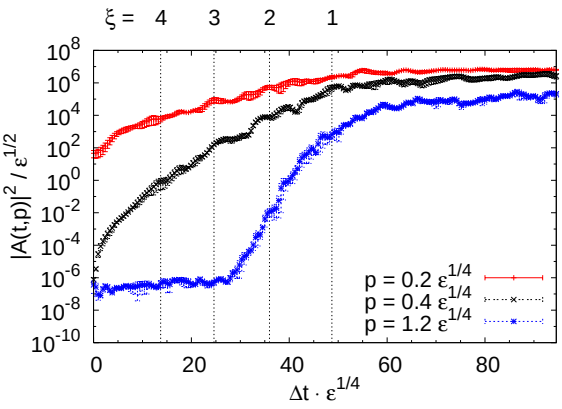

Figure 3.11: Time evolution of $|A(t,\mathbf{p})|^2$ from initial conditions with a slightly broadened distribution in the longitudinal direction with $\Delta/\Delta_z = 25$. The curves correspond to the momenta in the legend from top to bottom in the same order.

width Δ_z to be effectively $\delta(p_z)$- like a bigger value has been used. Aside from that, the initial conditions are of the same functional shape as Eq. (3.2). Plotted in Fig. 3.11 is the analogue of the curves in Fig. 3.3. The purpose of this is to check how restrictive the use of the $\delta(p_z)$- like distribution actually is. Several things can be deduced. First, we observe that the primary growth in the low-momentum modes is not purely exponential anymore. However, the growth is a bit faster than in the case of the $\delta(p_z)$- like initial conditions. Comparing the times when the bulk anisotropy ξ takes specific values one sees that the difference is not tremendous. The degree of anisotropy remaining at the time of saturation turns out to be almost equal to the one found in Fig. 3.3, which confirms the robustness of the above results. We will not consider this scenario any further in the following.

As noted in the above discussion, the phenomenological picture of primary and secondary instabilities is highly reminiscent of parametric resonance in scalar inflaton dynamics [44]. In that context, secondary instabilities can readily be explained in terms of higher loop contributions to the self-energy in the 2PI effective action framework. Therefore, it is straightforward to ask if an analogous analysis can be carried out for the secondary instabilities in the gauge theory.

The argumentation in the scalar theory is based on the diagrams depicted in Fig. 3.12. Their contribution to the self-energy Π can parametrically be estimated as follows. Each propagator line can be either a spectral function (2.23) of the scalar theory or the statistical propagator analogous to (2.22). While the spectral function for a generic mode with a given momentum cannot grow arbitrarily large [12] the statistical propagator is proportional to the occupation number

[12] We assume that there is no pole in ρ in the mode under consideration.

(a) (b)

Figure 3.12: Self-energy diagrams dominating the nonlinear, source-induced amplification regime in parametric resonance [44]. The left hand diagram involves interactions of the fluctuating field with the external field as indicated by the dashed line and the cross. Due to Eq. (3.6) this does not have a direct analogue in the work at hand.

and can attain arbitrarily large values. Therefore, we focus on the case that all propagator lines in Fig. 3.12 represent statistical propagators F. For small initial occupation number these are suppressed by factors of the coupling constant[13] g (which is assumed to be small) from the vertices. For each diagram one can then figure out how large F has to grow in order to cancel the factors g from the vertices. For the case of the loop-diagram in Fig. 3.12 one finds that for $F \sim 1/g$ the factor g^2 arising from the vertices is cancelled its contribution to the self-energy becomes $O(1)$. The "setting-sun diagram" in panel (b) makes a $O(1)$- contribution for $F \sim g^{4/3}$. Since the modes under consideration initially feature small occupation numbers, the former diagram's contribution becomes relevant at an earlier instant of time. By analysing the dynamics in terms of the dominating diagrams while neglecting the higher order diagrams it is possible to reproduce the full time evolution of the secondary instabilities during the enhanced fluctuation period [44]. In particular, the growth rates of the secondary instabilities can be computed and they turn out to be integer multiples of the primary growth rates.

Unfortunately, this analysis cannot be translated directly to non-Abelian gauge theories for the following reason. In parametric resonance only a very narrow band of momenta of the field's Fourier modes is unstable and grows exponentially. This allows for a saddle-point expansion of the self-energy. The growth rates of the secondary instabilities are predicted to be integer multiples of the growth rate of the (single) primary rate. This is confirmed by numerical simulations with high precision. In the present case however, a broad domain of low-momentum modes is unstable and the growth rate has a pronounced dependence on p_z. Therefore, the approach that proved successful in parametric resonance cannot be applied here directly. This is corroborated by the failure of the secondary growth rates to take integer multiples of primary growth rates.

In spite of these complications a diagrammatic analysis can be carried out to a certain extent. The strategy is as follows. We compute the self-energy contributions from Fig. 3.13 numerically,

[13]The coupling constant in the O(N)- scalar field theory is usually denoted by λ which corresponds to g^2 in the present discussion. For the sake of clarity we summarise the discussion from [44] renaming λ as g.

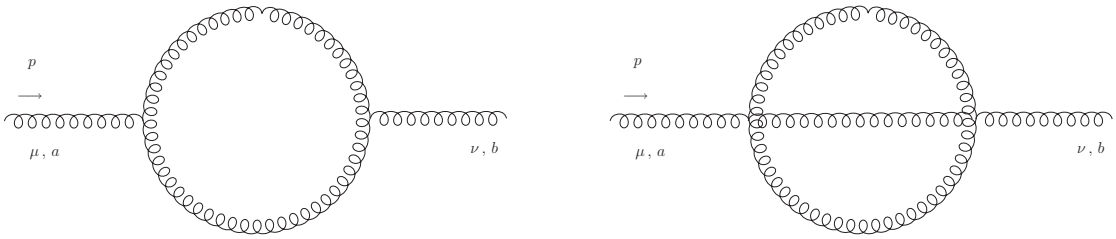

(a) (b)

Figure 3.13: Loop diagrams (a) $\Pi^{\mu\nu\,(1)}_{ab}(t,\mathbf{p})$ given in Eq. (3.26) and (b) $\Pi^{\mu\nu\,(2)}_{ab}(t,\mathbf{p})$ given in Eq. (3.27). The propagator lines correspond to the exact classical-statistical propagator (3.23), while the vertices are the perturbative ones from Eqns. (3.24) and (3.25).

using the classical-statistical approximation to F from our simulations. If their contribution to the self-energy becomes $O(1)$ at a time coinciding with the onset of the secondaries it would provide a strong piece of evidence for the secondaries being driven by enhanced fluctuations.

The equal-time statistical propagator

$$F^{ab}_{\mu\nu}(t,\mathbf{x}-\mathbf{y}) = \langle\, A^a_\mu(t,\mathbf{x}) A^b_\nu(t,\mathbf{y})\,\rangle\,. \tag{3.23}$$

is easily accessible in our numerical simulations from the Fourier transform of the gauge field and constitutes the main input into our analysis. We emphasise that the statistical propagator obtained from the classical-statistical lattice simulations is exact in the sense that it contains contributions from all orders in the coupling[14]. Since we work in temporal axial gauge (2.14) it follows immediately that $F^{ab}_{00} = F^{ab}_{0\mu} = F^{ab}_{\mu 0} = 0$. The perturbative three- and four-gluon vertices [130] are given as

$$V^{\mu\nu\rho}_{3\,abc}(\mathbf{k},\mathbf{p},\mathbf{q}) = g\epsilon_{abc}\,\{g^{\mu\nu}(\mathbf{k}-\mathbf{p})^\rho + g^{\nu\rho}(\mathbf{p}-\mathbf{q})^\mu + g^{\rho\mu}(\mathbf{q}-\mathbf{k})^\nu\} \tag{3.24}$$

and

$$\begin{aligned} V^{\mu\nu\rho\sigma}_{4\,abcd} = -ig^2\{&\epsilon_{abf}\epsilon_{cdf}(g^{\mu\rho}g^{\nu\sigma} - g^{\mu\sigma}g^{\nu\rho}) \\ &+ \epsilon_{acf}\epsilon_{bdf}(g^{\mu\nu}g^{\rho\sigma} - g^{\mu\sigma}g^{\nu\rho}) + \epsilon_{adf}\epsilon_{bcf}(g^{\mu\nu}g^{\rho\sigma} - g^{\mu\rho}g^{\nu\sigma})\}\,. \end{aligned} \tag{3.25}$$

In the ensuing computations we can think of the the Lorentz indices in these vertices being restricted to run over spatial directions only (i. e. $\mu \in \{1,2,3\}$) because temporal components only appear together with vanishing $F^{ab}_{0\mu}$ and F^{ab}_{00}. The self-energy contribution of the one-loop

[14]Of course, the numerical data will inevitably have statistical errors which arise from computing the correlation function from a finite sample of the initial conditions (3.2).

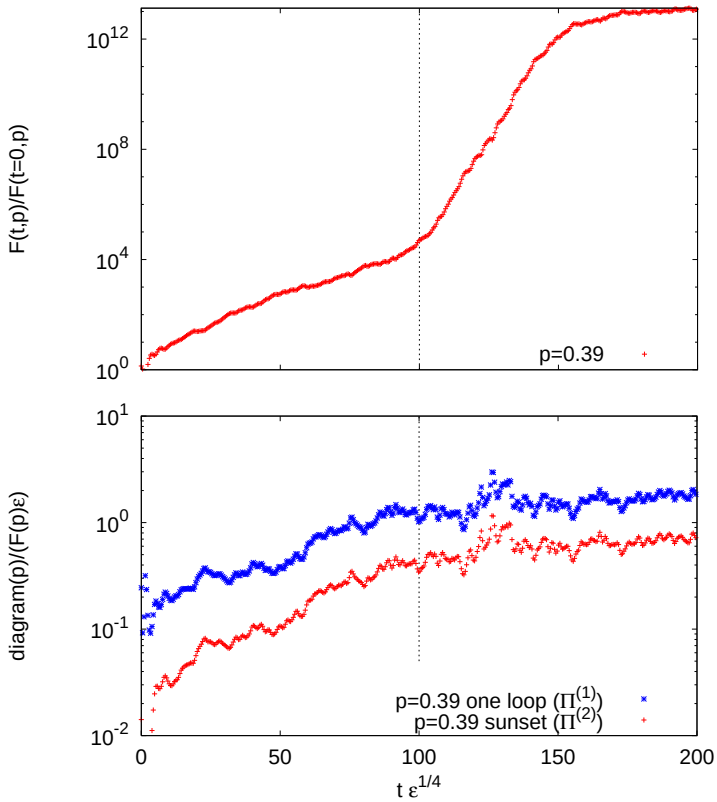

Figure 3.14: The upper graph displays the correlation function $F(t, \mathbf{p})$ from Eq. (3.23) as a function of time for given momentum $p_z/\epsilon^{1/4} = 1$. The lower graph shows for the corresponding momentum the relative contributions of the diagrams $\Pi^{(1)}(t, \mathbf{p})/F(t, \mathbf{p})$ and $\Pi^{(2)}(t, \mathbf{p})/F(t, \mathbf{p})$ to the correlation function. The upper, blue curve gives the one-loop contribution while the lower, red one is the setting-sun contribution.

diagram from Fig. 3.13(a) reads

$$\Pi^{\nu\sigma\,(1)}_{bf}(t, \mathbf{p}) = \frac{1}{2} \int \frac{d^3q}{(2\pi)^3} \left\{ V^{\mu\nu\rho}_{3\,abc}(-\mathbf{p}-\mathbf{q}, \mathbf{p}, \mathbf{q}) V^{\kappa\sigma\lambda}_{3\,dfe}(\mathbf{p}+\mathbf{q}, -\mathbf{p}, -\mathbf{q})\, F^{da}_{\kappa\mu}(t, \mathbf{p}+\mathbf{q}) F^{ec}_{\lambda\rho}(t, -\mathbf{q}) \right\}. \tag{3.26}$$

The two-loop diagram Fig. 3.13(b) is evaluated in coordinate space according to

$$\Pi^{\mu\nu\,(2)}_{mn}(t, \mathbf{x}-\mathbf{y}) = \frac{1}{6} V^{\mu\alpha\beta\gamma}_{4\,mabc} V^{\nu\kappa\lambda\rho}_{4\,nklr} F^{\kappa\alpha}_{ka}(t, \mathbf{x}-\mathbf{y}) F^{\lambda\beta}_{lb}(t, \mathbf{x}-\mathbf{y}) F^{\rho\gamma}_{rc}(t, \mathbf{x}-\mathbf{y}) \tag{3.27}$$

and then Fourier transformed.

Fig. 3.14 shows the results of such a calculation where all external colour indices have been set to one and Lorentz indices were chosen in the transverse plane, *i.e.* perpendicular to the

axis of anisotropy. The upper graph displays $F_{11}^{11}(t, \mathbf{p})$ for a given momentum as a function of time, similar to Fig. 3.3. We have chosen the momentum $p_z/\epsilon^{1/4} = 1$ such that the mode exhibits a primary instability which suddenly changes to a secondary instability at a later time of about $100\,\epsilon^{-1/4}$. The lower graph of Fig. 3.14 gives the absolute values of the loop diagrams Eqns. (3.26) and (3.27) normalised to the correlation function Eq. (3.23). The diagrams are evaluated for the same momentum as the gauge fields in the upper graph. One observes that initially these loop corrections are small compared to the size of the correlator (3.23) in units of ϵ. Accordingly, their contribution to the time evolution of the correlator may be neglected and primary instabilities dominate the dynamics. However, due to these instabilities loop corrections grow exponentially and faster than the correlator itself. The fast growth ceases at a time of $100\,\epsilon^{-1/4}$. This is precisely when the secondary instability sets in. Loop corrections grow faster due to the fact that exponentially growing modes $F(t, \mathbf{p})$ appear multiple times as propagators in the loop diagrams displayed in Fig. 3.13. For the reasons outlined before, we do not find that secondary growth rates correspond to integer multiples of primary ones here.

3.3 Plasma instabilities in SU(3) Yang-Mills theory

As has been discussed in Section 3.1, our analysis of QCD- plasma instabilities is to a big extent based on the assumption that there are no significant differences between instabilities in SU(2) and SU(3) Yang-Mills theory. That this indeed the case has been checked explicitly in a thesis related to this work [38, 80]. We will briefly report on these results in this section. Moreover, we describe how the primary growth rates of SU(3) plasma instabilities can be obtained from the corresponding SU(2) results which was found out in the context of this work.

The simulations of SU(3) gauge theory in [38, 80] employed initial conditions of the same kind as Eq. (3.2) in this work. The same value for the average energy density was prescribed which is distributed over degrees of freedom of eight colours instead of three as in the case of SU(2). This renders the overall gauge field amplitude smaller than in the SU(2) case and will be of importance in the below discussion. Solving the classical field equations for a sample of these initial conditions similar computations as for SU(2) were carried out. Most findings were almost identical to the SU(2) case. This applies in particular to the occurrence of primary and secondary instabilities and the isotropization on large length scales. Especially, similar values as in Eq. (3.18) for the momentum range that becomes isotropic at saturation time were obtained. The main difference that was found is that the primary growth rates turned out to be slower by ca. 25 per cent when measured in $\epsilon^{1/4}$ than in the case of SU(2). However, as we will show now, there is a simple way how the primary growth rates for SU(3) can be obtained by those found for SU(2). With this knowledge, the conclusion of our work for heavy ion collision experiments can be put on an even more solid foundation.

The central quantity for the following procedure is the mass scale defined in Eq. (3.9) which can be visualised by the tadpole diagram displayed in Fig. 3.2. More precisely, we obtain the non-vacuum part when inserting the classical-statistical approximation for the statistical propagator (2.22) of the gauge field. From the contraction of colour indices at the four-gluon-vertex it is immediate that for this diagram scales like

$$m^2_{T,\,\mathrm{SU(N)}} \sim N\,\tilde{A}^2_{\mathrm{SU(N)}} \tag{3.28}$$

for pure SU(N) gauge theory with a fixed overall gauge field amplitude $\tilde{A}$. In the initial conditions Eq. (3.2) employed for the SU(2) as well as the SU(3) simulation we have fixed the overall gauge field amplitude $C \propto \tilde{A}^2$ by demanding that the average lattice energy density $\hat{\epsilon}$ have a prescribed value. In the limits of either small field amplitudes of weak coupling the energy in SU(N) gauge theory scales with N as

$$\hat{\epsilon} \simeq \frac{a_s^4}{2} \sum_j \sum_{a=1}^{\mathrm{N}^2-1} \left\{ (E_j^a)^2 + (B_j^a)^2 \right\} \sim (\mathrm{N}^2-1)\,\tilde{A}^2 \,. \tag{3.29}$$

When comparing these initial conditions with identical $\hat{\epsilon}$ for the gauge groups $\mathrm{SU(N_1)}$ and $\mathrm{SU(N_2)}$ one finds

$$(\mathrm{N}_1^2-1)\,\tilde{A}^2_{\mathrm{SU(N_1)}} = (\mathrm{N}_2^2-1)\,\tilde{A}^2_{\mathrm{SU(N_2)}} \,. \tag{3.30}$$

For the specific gauge groups considered here this implies

$$\tilde{A}^2_{\mathrm{SU(3)}} = \frac{3}{8}\,\tilde{A}^2_{\mathrm{SU(2)}} \,. \tag{3.31}$$

Comparing the tadpole self-energies m_T^2 for two gauge groups then yields in consideration of Eq. (3.28)

$$\frac{m^2_{T,\,\mathrm{SU(N_1)}}}{m^2_{T,\,\mathrm{SU(N_2)}}} = \frac{\mathrm{N}_1}{\mathrm{N}_2}\,\frac{\tilde{A}^2_{\mathrm{SU(N_1)}}}{\tilde{A}^2_{\mathrm{SU(N_2)}}} \tag{3.32}$$

and thus

$$m_{T,\,\mathrm{SU(3)}} = \frac{3}{4}\,m_{T,\,\mathrm{SU(2)}} \,. \tag{3.33}$$

Therefore, the mismatch of 25 per cent between the SU(2) and SU(3) growth rates found in the numerical study [80] can be accounted for by a corresponding change in m_T. Phrased differently, both simulations yield identical growth rates measured in units of m_T, which is demonstrated in Fig. 3.15. There the growth rates as determined numerically in the SU(2) and SU(3) simulations are plotted measured in units of the respective value of m_T. The latter have also been computed

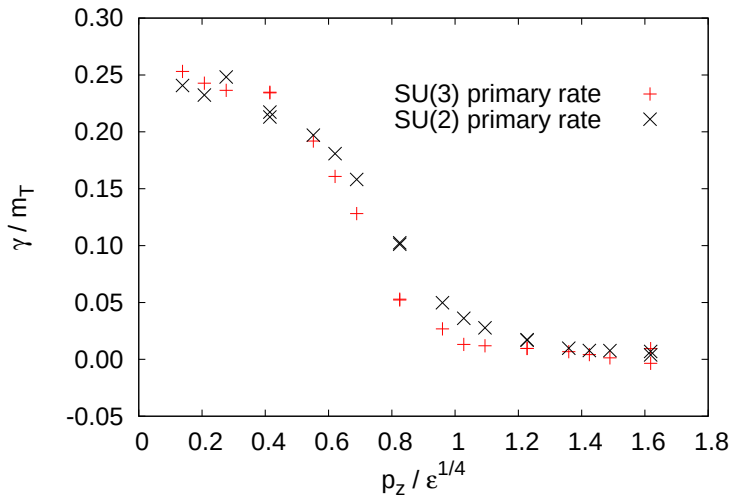

Figure 3.15: Growth rates as obtained from simulations of SU(2) and SU(3) Yang-Mills theory, measured in the respective value of m_T.

numerically from the initial conditions and their ratio is found to to be in excellent agreement with Eq. (3.33). Being the leading (local) contribution to the self-energy at early times m_T affects all dispersion relations $\omega(\mathbf{p})$ and thus provides a natural inverse time scale inherent in the initial conditions.

For the growth rates of the secondaries the above rescaling does not result in a precise agreement of the SU(2) and the SU(3) simulations. This is in parts due to the slightly larger error bars on the fit results for the secondary growth rates. On the other hand, we cannot expect the dynamics of the secondaries to be encoded completely in the initial conditions because their dynamics is highly nonlinear as has been demonstrated before. In any case, the difference in the secondary growth rates for SU(2) and SU(3) is of the order of twenty per cent as well and thus does not alter the phenomenological picture gained from the SU(2) simulations in a significant way.

3.4 Nielsen-Olesen instabilities on the lattice

In Section 3.2 we found that the functional shape of the growth rates as a function of momentum does not agree with the predictions for chromo-Weibel instabilities of the hard-loop effective theory. A resolution of this issue has recently been proposed by the authors of [76]. They suggest that our initial conditions give rise to a Nielsen-Olesen instability [59, 129, 147]. Indeed,

the growth rate[15] of longitudinal modes featuring a Nielsen-Olesen instability is given by [59, 76, 129, 147]

$$\gamma_{\mathrm{NO}}(p_z) = \sqrt{gB - p_z^2} \tag{3.34}$$

where B is the absolute value of a homogeneous magnetic field aligned in parallel to the z- axis. Although this cannot be precisely fitted to the data[16] displayed for instance in Fig. 3.9 its functional shape resembles the behaviour of our results much closer than the hard-loop predictions. In this Section we present a brief investigation of this issue. It will turn out that the instabilities reported in Section 3.2 are indeed likely to be of the Nielsen-Olesen kind. This opens up new possibilities for the *rôle* that instabilities may play in heavy ion collisions.

The Nielsen-Olesen instability occurs in the presence of a homogeneous magnetic field. By a suitable gauge transformation the latter can always be arranged to point into the direction $a = 1$ in colour space, which we will assume in the following. In an infinite volume such a field can easily be generated for instance from the vector potential[17]

$$A_x^1 = -\frac{1}{2} yB\,,\; A_y^1 = \frac{1}{2} xB\,,\; \text{all other } A_j^b = 0\,. \tag{3.35}$$

This yields the desired magnetic field $B_j^a = \delta^{1a}\delta_{3j}B$. The gauge field components A_x^2, A_x^3, A_y^2 and A_y^3 then feature a band of unstable low-momentum modes[18] which commence to grow exponentially when slightly excited. It can be readily verified that (3.35) is a time-independent solution of the Yang-Mills equations (2.11). Accordingly, also the magnetic field derived from (3.35) is constant in both space and time as long as it is unperturbed.

Unfortunately, studying a vector potential of the type (3.35) cannot be done with the program used for the numerical studies in the rest of this work without extensive alterations. The reason is that the periodic boundary conditions will introduce an undesired discontinuity into the above vector potential. Therefore, we numerically investigate Nielsen-Olesen instabilities in a slightly different setup.

[15] In Section 3.2 we have defined the growth rate from $|A|^2 \propto e^{\gamma t}$, which is motivated by relating $|A|^2$ to an occupation number. In the present section we define γ_{NO} from the exponential growth in $|A|$ rather than $|A|^2$ in order to allow for direct comparison with the literature. Thus, when comparing γ_{NO} to the growth rates of Section 3.2 one has to take into account this factor of two.

[16] This can easily be seen by noting that Eq. (3.34) describes points lying on an arc of a circle. However, inspection of the primary growth rates in Fig. 3.9 shows that $\gamma(p_z \to 0) \simeq 0.2\,\epsilon^{1/4}$ does not agree with the value where γ vanishes, which happens at $p_z \simeq 1\,\epsilon^{1/4}$. The authors of [76] argue that such a deformation of the curve $\gamma(p_z)$ should be expected for initial conditions of the shape (3.2).

[17] In this section we will often denote the x- components of the gauge field in colour a explicitly by A_x^a instead of A_1^a in order to avoid confusion with the colour indices. As before, we work in temporal axial gauge (2.14).

[18] Fuji *et al.* [76] choose their magnetic field to be aligned along the ($a = 3$)- direction in colour space. They carry out the analysis of unstable modes in a complex linear combination ϕ of the corresponding gauge field components.

From Eq. (2.5) one sees immediately that a homogeneous magnetic field can also be generated from a suitable constant gauge potential via the commutator term. For instance, consider the SU(2) gauge field

$$A_x^2 = A_y^3 = \sqrt{\frac{B}{g}} \text{ , all other } A_j^b = 0 \text{ .} \tag{3.36}$$

This yields the same magnetic field as (3.35). However, there is an important difference between the two gauge field configurations (3.35) and (3.36). The former is a constant (in space and time) solution of the Yang-Mills equations while the latter is not. Instead, its zero modes display nonlinear oscillations in time governed by the differential equations

$$\begin{aligned} \partial_t^2 A_x^2 &= -g^2 (A_y^3)^2 \, A_x^2 \\ \partial_t^2 A_y^3 &= -g^2 (A_x^2)^2 \, A_y^3 \text{ .} \end{aligned} \tag{3.37}$$

Note that $A_x^2 = A_y^3$ at all times if they are equal at initial time as it is the case for the initial conditions Eq. (3.36). This system can readily be solved numerically[19]. For future reference, we note that the temporal average of the magnetic field's modulus over one period of oscillation is found to be

$$\bar{B} \simeq 0.46 \, B(t = 0). \tag{3.38}$$

It has been shown that magnetic fields derived from spatially constant gauge fields also exhibit Nielsen-Olesen instabilities [151].

As in Section 3.2 we solve the discretised field equations but now starting from Eq. (3.36). In order to trigger a Nielsen-Olesen instability we add a bit of noise of the form $\delta A(r - 0.5)$ to all $A_j^b(t = 0, \mathbf{x})$. The amplitude of the noise is $\delta A = 0.001 \sqrt{B/g}$ and $r \in]\,0, 1\,[$ is a random number from the homogeneous distribution on that interval[20] . In particular, we also perturb those components that have originally been set to zero in Eq. (3.36). Given this initial configuration for the gauge field we can initialise all links according to Eq. (2.30). When computing the magnetic field from Eq. (2.37) we find that the result possesses non-vanishing entries in the colours $a = 2$ and $a = 3$, which is in disagreement with the continuum field. By modifying the amplitude of the lattice gauge field, which can alternatively be interpreted as a change in lattice spacing a_s via Eq. (2.48), we have found that the contamination of $\hat{\mathcal{F}}$ scales as a_s^3, which unmasks it as the inherent but well-controlled discretisation errors in Eq. (2.33).

We plot the time evolution of several low-momentum modes $A_j^b(t, p_z)$ in Fig. 3.16. In contrast

[19] As an aside, we have integrated Eq. (3.37) by means of both a computer algebra package and our program. The two solutions were found to be in excellent agreement.

[20] We have checked that varying the amplitude of the noise over an order of magnitude does not affect the results.

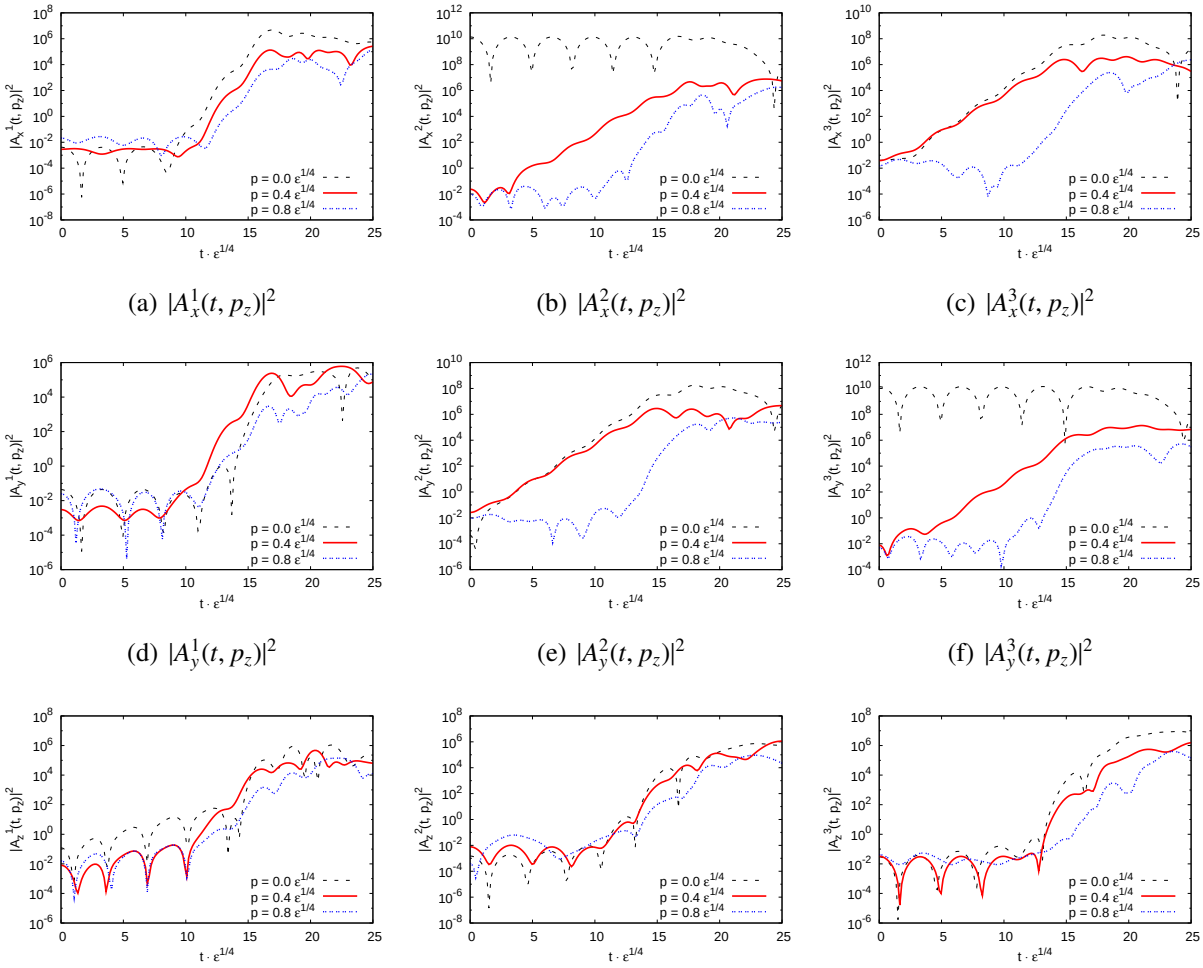

(a) $|A_x^1(t,p_z)|^2$ (b) $|A_x^2(t,p_z)|^2$ (c) $|A_x^3(t,p_z)|^2$

(d) $|A_y^1(t,p_z)|^2$ (e) $|A_y^2(t,p_z)|^2$ (f) $|A_y^3(t,p_z)|^2$

(g) $|A_z^1(t,p_z)|^2$ (h) $|A_z^2(t,p_z)|^2$ (i) $|A_z^3(t,p_z)|^2$

Figure 3.16: Time evolution of the individual gauge field components in lattice units starting from the initial conditions (3.36) supplemented by noise. Each panel shows the time evolution of three different Fourier coefficients whose momenta are parallel to the z- axis. Subfigures (c) and (e) show exponentially growing zero modes which are typical for Nielsen-Olesen instabilities. The strongly initialised zero modes and there oscillations are clearly visible in (b) and (f). In contrast to Fig. 3.3, no averaging over colour has been carried out here.

to Section 3.2, we have plotted the curves for each individual colour index rather than averaging over them in order to gain more detailed insights into the instability. Several important observations can be made in Fig. 3.16.

First, we see that the zero modes of A_x^2 and A_y^3 oscillate. These oscillations are almost identical to the unperturbed case (*i.e.* zero noise $\delta A = 0$). The zero mode oscillations remain practically unaffected by the dynamics of the other modes until $t \simeq 15\,\epsilon^{-1/4}$. At early times the magnetic field is given as a function of time by these curves in Fig. 3.16(b) and (f). This is because the contribution of the derivative terms is small so that $B(t) \simeq A(t)^2$ from Eq. (2.5).

Next, it is obvious that the low-momentum modes of A_x^2, A_x^3, A_y^2 and A_y^3 are unstable, which is in agreement with the predictions [76, 151]. Above a certain wave number there are no instabilities at early times $t \lesssim 10\,\epsilon^{-1/4}$ as exemplified by the blue, lowermost curves in each of the panels of Fig. 3.16. All instabilities saturate at approximately $t \simeq 15\,\epsilon^{-1/4}$ which coincides with the time when the zero modes cease to oscillate.

Unambiguous evidence for the Nielsen-Olesen nature of the instabilities at hand is provided by Figs. 3.16(c) and (e). They demonstrate that the gauge field possesses unstable zero modes. This is typical for the Nielsen-Olesen instability while there are no growing zero modes in the chromo-Weibel scenario.

A discerning look at Fig. 3.16(b) and (f) reveals that the exponential growth is actually not uniform in time. Rather, it slows down and accelerates again with the frequency of the zero mode oscillations as can be nicely seen there. In particular, the growth always seems to speed up when the amplitude of the zero mode is at its maximum while it slows down at the respective minimum. Fitting growth rates over times large compared to the oscillation frequency must yield something like an average growth rate. This will be relevant below.

Finally, one observes that the behaviour of the system changes at $t \simeq 10\,\epsilon^{-1/4}$. In analogy to the secondary instabilities discussed in Section 3.2 formerly stable modes suddenly start to grow as well.

The growth rates of the instabilities can be obtained by fitting an exponential function to the data. The results of such a fit are shown in Fig. 3.17. The left panel shows γ_{NO} as a function of p_z for different initial field strengths. Both the growth rate and the momentum are plotted in lattice units. Comparing the data to the prediction from Eq. (3.34) it turns out that the latter does not represent the data. However, we find that the growth rates can be described very well by

$$\gamma_{\mathrm{NO}}^{(\mathrm{num})}(p_z) = \sqrt{0.42gB - p_z^2} \tag{3.39}$$

which is the function underlying the analytic curves in Fig. 3.17(a) for each of the simulations. We note that the numerical factor appearing in Eq. (3.39) is almost equal to the one in Eq. (3.38). This is explained by the aforementioned observation that the exponential growth is not uniform

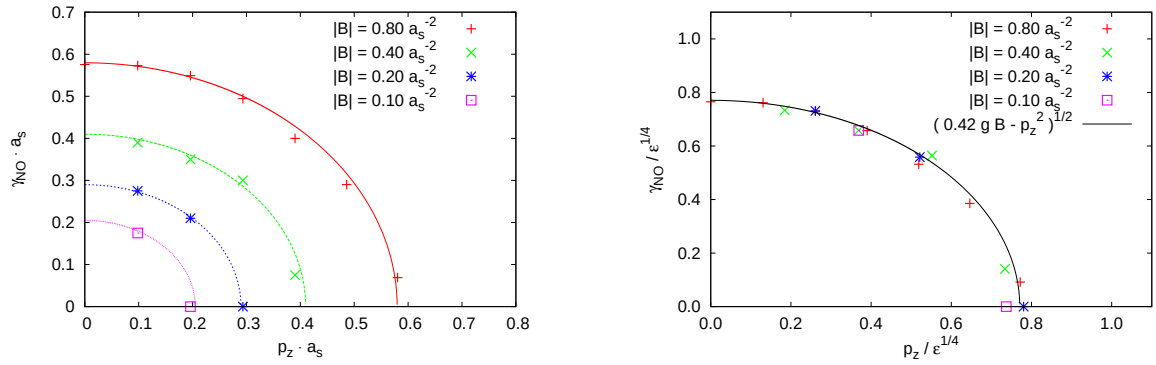

(a) (b)

Figure 3.17: Growth rates of Nielsen-Olesen instabilities from simulations with different magnetic field strengths measured (a) in lattice units and (b) in units of $\epsilon^{1/4}$. The solid lines represent the corresponding function Eq. (3.39) for the various magnetic field strengths. $g = 1$ in all computations.

in time. The average growth rate as obtained by fitting over a time interval of several zero mode oscillations is thus given to a very good approximation by inserting the temporal average of the magnetic field into the analytical expression (3.34). We emphasise that the latter was derived for the initial condition (3.35) which yields a magnetic field that is constant in time.

The data points in Fig. 3.17(b) are exactly the same as in Fig. 3.17(a), however with the growth rate as well as the momentum measured in units of $\epsilon^{1/4}$. The reason for the precise collapse of the results of simulations with different initial field strength onto a single curve can be understood from Eqns. (3.34) or (3.39) for the growth rate. The relevant momentum scale appearing there (as in the initial conditions) is set by $\sqrt{gB}$ which determines both the maximum growth rate and the zero of the expression under the square root. Note that this is directly related to the energy density which is proportional to B^2.

The inverse of the maximum growth rate (*i.e.* the characteristic time scale) in physical units following from (3.39) for an energy density of 30 GeV and $g = 1$ is

$$\frac{1}{\gamma_{\mathrm{NO}}^{(\mathrm{num})}(p_z = 0)} \simeq \frac{1}{0.8\epsilon^{1/4}} = 0.36 \text{ fm/c} . \tag{3.40}$$

Using the analytical formula (3.34) for matching to physical units with the same parameters yields

$$\frac{1}{\gamma_{\mathrm{NO}}(p_z = 0)} = \frac{1}{\sqrt{B}} = \frac{1}{\sqrt[4]{2\epsilon}} \simeq 0.24 \text{ fm/c} . \tag{3.41}$$

The momentum scales corresponding to (3.40) and (3.41) are 560 MeV and 830 MeV, respec-

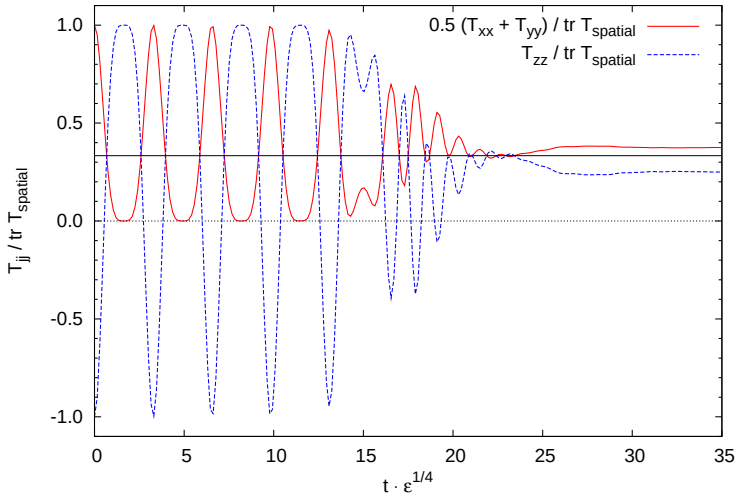

Figure 3.18: Time evolution of the diagonal entries of the spatial stress-energy-momentum tensor. This is the analogue to Fig. 3.6. Here, an approximately isotropic state is reached much faster.

tively. This indicates which degrees of freedom could be affected by Nielsen-Olesen instabilities. Either of (3.40) and (3.41) represents noticeable speed-up when compared to (3.21). On the other hand, due care should be exercised when interpreting these numbers in the context of heavy ion collisions. Initial conditions of the idealised type (3.36) are certainly not realised in the out-of-equilibrium quark gluon plasma created at RHIC or LHC.

As in the case of the initial conditions (3.2) from Section 3.1 we are interested in the time it takes the system to become globally isotropic. Fig. 3.18 shows the transverse and longitudinal pressure computed from the same field configurations as the data displayed in Fig. 3.16. This is to be compared to Fig. 3.6. It is obvious that the time evolution is much more violent in the present scenario. More surprising, the stress-energy-momentum-tensor becomes isotropic after a relatively short time. Note that there is a significant difference between the initial conditions employed in Section 3.2 and the ones of this section. While in the case of the former $T_{33} \simeq 0$ at initial time, the homogeneous fields (3.36) give T_{33} a negative value[21], as follows from (3.7).

In spite of several differences the primary instabilities in Section 3.2 bear remarkable similarity to the Nielsen-Olesen instabilities studied here. Most important, the functional shape of the growth rate as a function of longitudinal momentum is better reproduced by the Nielsen-Olesen scenario than by the predictions for the chromo-Weibel instability. An argument why the initial conditions (3.2) should trigger Nielsen-Olesen instabilities has been given in [76]. Eq. (3.2) will

[21] Cf. the discussion of the structure of T_{ij} in the colour glass condensate in [103].

cause derivatives to be of a typical scale Δ_x. In turn, the initial fields will be approximately homogeneous on length scales Δ_x^{-1}, which also holds for the magnetic fields. Therefore, the latter are susceptible to Nielsen-Olesen instabilities.

3.5 Implications for heavy ion collision experiments

We close this Chapter by drawing conclusions about the thermalisation process of the quark gluon plasma created in heavy ion collisions. As outlined in the introduction, this has been a major motivation for this investigation.

The majority of our calculations has been carried out using the colour-glass-like initial conditions presented in Section 3.1. Accordingly, the respective analysis relies on the assumptions that have been stated there. It has emerged that considering SU(2) is not a severe restriction and that many of our results can be extrapolated to the physical QCD- gauge group SU(3) in a controlled way.

The occurrence of plasma instabilities has been confirmed and their impact on the isotropization of the medium has been studied. We emphasise that this could be analysed to a big extent in terms of gauge invariant quantities. It can be said that the instabilities indeed do have the effect to isotropize the system, as has been conjectured in the past [17]. The restriction to be made here is that the system does not fully isotropize. Only a domain of low-momentum degrees of freedom is driven to isotropy by the instabilities. In this regard, instability driven isotropization is still reminiscent of the original "bottom-up" scenario [25] of thermalisation. The momentum scale on which isotropization happens is not too different from the transverse-momentum range for which elliptic flow is well described by hydrodynamic calculations.

We have been able to make predictions of the involved time scales in physical units. These characteristic time scales of the plasma instabilities are comparable to the time at which hydrodynamic evolution sets in. However, the growth rates computed for the colour-glass initial conditions do not allow for a large number of e- foldings during this time. A similar results was obtained in [142]. The fact that the growth rates in SU(3) are even slower than in the SU(2) case renders the scenario of instability driven isotropization less likely.

Aside from the study of the primary instabilities, which are relevant during the entire period of violent dynamics, we have found another class of instabilities. These secondary instabilities could be shown to bear remarkable qualitative similarity to parametric resonance in scalar field theories. Their relevance for the thermalisation of the quark gluon plasma is even more difficult to judge, though, than for the primaries. While their growth rates are significantly higher than those of the primary instabilities they set in rather late. Apart from a narrow momentum interval secondary instabilities saturate before the affected modes even come close to isotropy.

The results for Nielsen-Olesen instabilities open up new perspectives. Certainly, the initial conditions used in the simulations are too idealised to be considered of direct relevance for RHIC or LHC. However, it could be shown that non-Abelian gauge theories do allow for processes with a characteristic time scale of 0.2 fm/c. An instability with such a fast growth rate certainly would have a sizable impact. It can be speculated that sufficiently homogeneous fields could exist in flux tubes connecting *e.g.* quark-antiquark pairs in the out-of-equilibrium plasma. Phenomenological questions of this kind are beyond the scope of this work and need to be engaged in a different approach.

Chapter 4

Fixed points and turbulence

In Chapter 3 we have analysed the time evolution of an out-of-equilibrium ensemble of non-Abelian gauge fields focusing on the processes that are relevant at early times. In this Chapter we will investigate the properties of the system after the saturation of instabilities.

From Figs. 3.3, 3.4 and 3.7 it is obvious that the time evolution of the Yang-Mills system starting from the anisotropic ensemble (3.2) can very roughly be divided into two phases. The first one is governed by violent processes (plasma instabilities) whose dynamics are intrinsically "fast". The second phase can generally be characterised as "slow". After the saturation of instabilities the further evolution towards (classical) thermal equilibrium apparently slows down tremendously, as has been indicated by Fig. 3.6 and the discussion thereof. It is the purpose of this Chapter to provide a detailed analysis of this slow phase. Rather than just being slow it will turn out to be even quasi-stationary in nature.

We have already mentioned in Section 3.2 in the context of secondary instabilities that there are remarkable similarities between scalar theories and gauge theories. The analogies between these two - *a priori* very different - physical systems will eventually prove to be even more profound. This agreement turns out to be so precise that it confirms the notion of universality far from equilibrium.

In the context of out-of-equilibrium scalar theories encountered in inflationary early universe cosmology the fast and violent evolution at initial times drives the system towards quasi-stationary states [41, 112, 113]. Note that - as for the initial conditions (3.2) studied here - also in that case the evolution at early times is almost entirely classical, which has been demonstrated by explicitly comparing the quantum and the classical time evolution obtained from numerical 2PI computations for instance in [41]. These states feature power-law spectra in the statistical prop-

agator (2.22) with clearly non-thermal spectral indices[1]. Hence these quasi-stationary states are also referred to as nonthermal fixed points. Their description is usually based on the assumption of classicality (2.29) and thus their occurrence is limited to the classical regime. The full quantum dynamics eventually causes the system to depart from the fixed point and drives it towards (quantum) thermal equilibrium. Even if finally superseded by quantum physics, the presence of a fixed point in the classical dynamics can significantly impede the overall thermalisation of the system under consideration.

A general approach to out-of-equilibrium fixed points has recently been proposed [39]. Based on functional renormalisation group (FRG) techniques it allows to investigate nonthermal fixed points from first principles of quantum field theory. Applying these methods, the properties of the fixed point ensuing parametric resonance could be understood [41] and were found to agree with numerical computations. The FRG approach correctly describes the IR- as well as the UV- parts of the spectrum. It is important to stress that the physics of fixed points encountered in both of these regimes is very different. While the fixed points in the low-momentum regime manifest themselves in a similar (but more extreme) way as equilibrium critical phenomena, the fixed-point solutions present at asymptotically high momenta are analogous to Kolmogorov wave turbulence [159]. It is the latter that we focus upon in this work, using the methods from [39,41] to investigate turbulence in SU(2) Yang-Mills theory after the saturation of instabilities.

Several authors have already studied turbulence-like phenomena in Yang-Mills theory. Earlier works [77, 127, 128, 156, 157] have found indications for chaotic behaviour, some of them studying gauge theories in (1+1) or (2+1) dimensions. Recently, the interest in the subject has been amplified again in the context of the thermalisation of the quark gluon plasma. Various publications report the occurrence of power-law spectra [18, 19, 73, 126, 149]. Unfortunately, the knowledge about turbulence in non-Abelian gauge theories is not as advanced as in the case of scalars. For instance, the precise numerical value of the spectral index is still under debate [19, 126]. These recent works are based on the framework of Boltzmann equations and hard-loop resummation.

An important motivation for the analysis presented in this Chapter is that the study of fixed points provides an excellent test case for the application of 2PI resummation techniques to gauge theories, as outlined in the Introduction. It has also been mentioned there that the treatment of non-Abelian gauge theories in the 2PI framework is not as advanced as for other field theories, despite significant progress recently made [135–137, 143]. The equations governing nonthermal fixed-point solutions are less complicated than the general non-equilibrium evolution equations [30, 31, 39] due to the symmetry properties (*i.e.* translation invariance in time and space

[1] Phenomena of this kind are frequently discussed in terms of Boltzmann equations and power-law particle number spectra, for instance in [113, 159].

and isotropy) of the fixed point. Therefore, the analysis of nonthermal fixed points by means of 2PI methods contributes to the development of these methods in order to finally apply them in generic out-of-equilibrium studies of non-Abelian gauge theories as well.

The investigation of turbulence in SU(2) Yang-Mills theory in this Chapter proceeds along two complimentary lines. In Section 4.1 we numerically compute Fourier spectra of the gauge field propagator in the classical-statistical approximation. Subsequently, we study the properties of the fixed point analytically in Section 4.2 and we will compare the results obtained in these two ways.

We briefly summarise some necessary definitions, closely following the conventions in [30, 31,39,41]. We start by recalling the definitions of the time-ordered, advanced and retarded propagators of the gauge field which have been defined in Eqns. (2.20), (2.25) and (2.26), respectively. For the purposes of this Chapter the statistical propagator (2.22) and the spectral function (2.23) are particularly relevant. We now discuss several properties of these propagators that will be exploited in the following.

Without spontaneous breaking of the gauge symmetry, all of the above propagators are diagonal in the colour indices. That is, the colour structure of *e.g.* the time-ordered propagators can be factored out according to

$$G^{ab}_{\mu\nu}(x,y) \equiv \delta^{ab} G_{\mu\nu}(x,y) \; . \tag{4.1}$$

Completely analogous identities hold for the other correlation functions. This property will greatly facilitate many of the below calculations.

In this chapter we are interested in the properties of fixed-point solutions. By definition, fixed-point solutions are invariant under translations in time and we will moreover assume that they are also invariant with respect to spatial translations. Introducing the centre of mass coordinate

$$X^\mu := \frac{x^\mu + y^\mu}{2} \tag{4.2}$$

and the displacement

$$s^\mu := x^\mu - y^\mu \; , \tag{4.3}$$

the propagators only depend on s (but not on X) under the premise of spacetime translation invariance. Therefore, the full information is encoded in the Wigner transformed functions (By assumption, both sides of the following equations are independent of X.)

$$\begin{aligned} \tilde{F}_{\mu\nu}(k) &:= \int d^4 s \, e^{ik\cdot s} \, F_{\mu\nu}(X + \frac{s}{2}, X - \frac{s}{2}) \\ \tilde{\rho}_{\mu\nu}(k) &:= -i \int d^4 s \, e^{ik\cdot s} \, \rho_{\mu\nu}(X + \frac{s}{2}, X - \frac{s}{2}) \end{aligned} \tag{4.4}$$

where factors of i have been introduced in order to keep these functions real-valued. The Wigner transforms of the advanced and retarded propagator are defined in the same way as $\tilde{\rho}$.

In addition to temporal and spatial translation invariance we will specialise to isotropic states. It will have to be checked afterwards to what extent this simplification is applicable in the current analysis[2]. For isotropic systems all Green functions are symmetric in the Lorentz indices, *i.e.*

$$\tilde{F}_{\mu\nu}(p) = \tilde{F}_{\nu\mu}(p) \qquad \tilde{\rho}_{\mu\nu}(p) = \tilde{\rho}_{\nu\mu}(p) \qquad \tilde{G}^{(A)/(R)}_{\mu\nu}(p) = \tilde{G}^{(A)/(R)}_{\nu\mu}(p)\ . \tag{4.5}$$

Under the present assumptions, the non-local contributions to the self-energy appearing in the decomposition (2.28) are also diagonal in the colour indices. In analogy to Eq. (4.1) they can be written as

$$\begin{aligned} \Pi^{\mu\nu}_{(F)\,ab}(x,y) &= \delta_{ab}\Pi^{\mu\nu}_{(F)}(x,y) \\ \Pi^{\mu\nu}_{(\rho)\,ab}(x,y) &= \delta_{ab}\Pi^{\mu\nu}_{(\rho)}(x,y)\ . \end{aligned} \tag{4.6}$$

Subsequently, the Wigner transforms of $\Pi_{(F)}$ and $\Pi_{(\rho)}$ are defined in a similar way as for the propagators:

$$\begin{aligned} \tilde{\Pi}^{\mu\nu}_{(F)}(k) &:= \int d^4s\, e^{ik\cdot s}\, \Pi^{\mu\nu}_{(F)}(X+\frac{s}{2}, X-\frac{s}{2}) \\ \tilde{\Pi}^{\mu\nu}_{(\rho)}(k) &:= -i\int d^4s\, e^{ik\cdot s}\, \Pi^{\mu\nu}_{(\rho)}(X+\frac{s}{2}, X-\frac{s}{2})\ . \end{aligned} \tag{4.7}$$

As in Eq. (4.4) the integrands in these definitions are in fact independent of X by virtue of spacetime translation invariance. Accordingly, we suppress the X- dependence in the following. The Wigner-transformed self-energies obey the following identities [30, 31]:

$$\begin{aligned} \tilde{\Pi}^{\mu\nu}_{(F)\,ab}(p) &= \tilde{G}^{-1\,\mu\gamma}_{(R)ac}(p)\,\tilde{F}^{cd}_{\gamma\delta}(p)\,\tilde{G}^{-1\,\delta\nu}_{(A)db}(p) \\ \tilde{\Pi}^{\mu\nu}_{(\rho)\,ab}(p) &= \tilde{G}^{-1\,\mu\nu}_{(R)ab}(p) - \tilde{G}^{-1\,\mu\nu}_{(A)ab}(p)\,, \end{aligned} \tag{4.8}$$

Using the identity [31, 55]

$$\tilde{\rho}^{ab}_{\mu\nu}(p) = \tilde{G}^{ab}_{(R)\mu\nu}(p) - \tilde{G}^{ab}_{(A)\mu\nu}(p) \tag{4.9}$$

the identities (4.8) can be recast into the form

$$\begin{aligned} \tilde{F}_{\mu\nu}(p) &= \tilde{G}^{(R)}_{\mu\alpha}(p)\tilde{\Pi}^{\alpha\beta}_{(F)}(p)\tilde{G}^{(A)}_{\alpha\nu}(p) \\ \tilde{\rho}_{\mu\nu}(p) &= \tilde{G}^{(R)}_{\mu\alpha}(p)\tilde{\Pi}^{\alpha\beta}_{(\rho)}(p)\tilde{G}^{(A)}_{\alpha\nu}(p)\ . \end{aligned} \tag{4.10}$$

[2]The numerical results of Section 4.1 provide evidence that the fixed point encountered here is indeed isotropic.

We note that the definitions of $\tilde{F}$ and $\tilde{\rho}$ imply the following intrinsic symmetries

$$\begin{aligned} \tilde{F}_{\mu\nu}(-p) &= +\tilde{F}_{\nu\mu}(p) \\ \tilde{\rho}_{\mu\nu}(-p) &= -\tilde{\rho}_{\nu\mu}(p) \, . \end{aligned} \tag{4.11}$$

In fact, this also holds without assuming isotropy.

As suggested by the scalar results [41] we search for scaling solutions for the statistical propagator and the spectral function of the kind

$$\begin{aligned} \tilde{F}_{\mu\nu}(l\,p) &= |\,l\,|^{-(2+\kappa)}\tilde{F}_{\mu\nu}(p) \\ \tilde{\rho}_{\mu\nu}(l\,p) &= |\,l\,|^{-2}\tilde{\rho}_{\mu\nu}(\mathrm{sign}(l)p) \, . \end{aligned} \tag{4.12}$$

Here, l is an arbitrary, non-zero real number. If scaling behaviour of this kind is found then the upper identity in Eq. (4.12) defines the occupation number exponent κ. For the sake of completeness we note in passing that the ansatz (4.12) assumes that the anomalous dimension η as well as the dynamical critical exponent - which is usually denoted by z - take their perturbative values zero and one, respectively. This is justified since in the ensuing analytical treatment we require the UV to be perturbative anyway. Moreover, we note that if the spectral function $\tilde{\rho}$ scales as in Eq. (4.12) then the advanced and retarded propagators (and their Wigner transforms) exhibit the identical scaling behaviour, *i.e.*

$$\tilde{G}^{(R)/(A)}_{\mu\nu}(l\,p) = |\,l\,|^{-2}\tilde{G}^{(R)/(A)}_{\mu\nu}(\mathrm{sign}(l)p) \, . \tag{4.13}$$

4.1 Turbulent spectra from lattice simulations

The results of Section 3.2 show that the non-Abelian gauge field dynamics slow down tremendously following the saturation of the instabilities. Moreover, it has been stated in Section 3.2 that the instabilities display remarkable similarities with parametric resonance in scalar field theories. Since nonthermal fixed points have been found in the latter case [41] it is straightforward to consider the possibility that such a fixed point could be encountered in the Yang-Mills system, too. In this Section we will tackle this issue numerically. The corresponding analytical approach is the subject of the ensuing Section 4.2.

In order to numerically check for the existence of a fixed point we compute spectra of the statistical propagator (2.22) in the classical-statistical approximation. To that end we use the same program as in Chapter 3 starting the integration of the field equations from the same initial conditions (3.2). However, we run the program until much later times. Moreover, we take larger lattice volumes in order to achieve a better momentum resolution, which allows to fit the shape of spectra more precisely. The parameters of the simulations are listed in Table 4.1.

Quantity	**Symbol**	**Value/setting**
Lattice volume	N^3	128^3
Number of initial configurations/ensemble size	-	20
Transverse width	$\hat{\Delta}_x$	0.5
Longitudinal width	$\hat{\Delta}_z$	0.001
Average energy density	$\hat{\epsilon}$	0.05
Time step	a_t	$0.02\, a_s$
Gauge coupling	g	1
Coulomb gauge fixing precision Eq. (4.19)	e_2	$< 10^{-12}$

Table 4.1: Parameters of the simulations from which the results presented in Section 4.1 have been computed.

In the classical-statistical approximation the statistical propagator (2.22) is given as the correlation function of the gauge field. From a practical point it is too cumbersome to access $\tilde{F}_{\mu\nu}(p)$ in these simulations, though, because that would require to store entire field configurations $\tilde{F}_{\mu\nu}(t,\mathbf{x})$ for a large number of time steps. The most direct way to find possible scaling solutions of the kind (4.12) is the analysis of the statistical propagator (2.22) evaluated at equal times $t = x^0 = y^0$. A scaling solution (4.12) implies that the equal-time correlation function

$$F^{ab}_{\mu\nu}(t,\mathbf{p}) = \int d^3x\, e^{-i\mathbf{p}\cdot\mathbf{x}} \langle\, A^a_\mu(t,\mathbf{x}) A^b_\nu(t,0)\,\rangle \tag{4.14}$$

also displays power-law behaviour of the form

$$F_{\mu\nu}(t, l\,\mathbf{p}) = |\,l\,|^{-(1+\kappa)} F_{\mu\nu}(t,\mathbf{p}) \tag{4.15}$$

once the system is sufficiently close to the fixed point such that $F(t,\mathbf{p})$ does not show a perceivable time dependence anymore. Of course, it is only then that identifying the equal time correlation function $F(t,\mathbf{p})$ with the translation invariant Wigner transform $\tilde{F}(p_0,\mathbf{p})$ for $p_0 = 0$ is justified. Assuming that the system has reached the fixed point and that a scaling solution as in Eq. (4.12) is present, the assertion in Eq. (4.15) can be proved as follows:

$$\begin{aligned} F_{\mu\nu}(t, l\mathbf{p}) &= \int \frac{d\omega}{2\pi}\, e^{i\omega\Delta t} \tilde{F}_{\mu\nu}(\omega, l\mathbf{p}) \qquad (\Delta t = 0) \\ &\overset{\text{Eq. (4.12)}}{=} l^{-(2+\kappa)} \int \frac{d\omega}{2\pi}\, \tilde{F}_{\mu\nu}(\frac{\omega}{l}, \mathbf{p}) \\ &\overset{\omega \equiv l\omega'}{=} l^{-(1+\kappa)} \int \frac{d\omega'}{2\pi}\, e^{i\omega'\cdot 0} \tilde{F}_{\mu\nu}(\omega', \mathbf{p}) \\ &= l^{-(1+\kappa)} F_{\mu\nu}(t,\mathbf{p})\ . \end{aligned} \tag{4.16}$$

By virtue of the convolution theorem it is straightforward and numerically inexpensive (using the Fast Fourier Transforms) to access the equal-time correlation functions of the gauge field once the Fourier coefficients of the latter have been computed. In particular, for a fixed spatial index j

$$F^{aa}_{jj}(t,\mathbf{p}) = \langle\, A^a_j(t,\mathbf{p}) A^a_j(t,-\mathbf{p}) \,\rangle = \langle\, |A^a_j(t,\mathbf{p})|^2 \,\rangle \tag{4.17}$$

where the last equality follows from the fact that $A^a_\mu(t,\mathbf{x})$ is a real-valued function in spacetime. In the following, we will drop the colour indices and understand F_{jj} as the average

$$\frac{\sum_a \langle\, |A^a_j(t,\mathbf{p})|^2 \,\rangle}{3} \tag{4.18}$$

of F^{aa}_{jj} over all three colour indices of SU(2). This is what we compute numerically.

The statistical propagator (2.22) is a gauge dependent quantity, which makes the analysis of fixed point less intuitive as compared to the scalar case. So far we have not chosen a specific gauge to carry out our analysis. There are good reasons to opt for the Coulomb gauge which is defined in the continuum case by the familiar Eq. (2.15). The most significant motivation for Coulomb gauge is that the relation to particle numbers can be put on a sound basis in the perturbative limit, which should be realised in the high momentum regime in which we expect turbulent behaviour. The gauge condition (2.15) eliminates one degree of freedom from the three spatial components of the gauge field. Thus only two degrees of freedom remain, corresponding to two transverse polarisations of gluons. Coulomb gauge has been employed for instance in [19] where the relation to particle numbers is discussed as well. Therefore, we compute Coulomb gauge spectra of the statistical propagator in what follows.

We have to expect that even if the system approaches a nonthermal fixed point at some stage of the time evolution it will finally evolve towards (classical) thermal equilibrium[3] characterised by $\kappa = 1$. Therefore, we can at best find a quasi-stationary regime during the course of the simulations.

Coulomb gauge is defined by the gauge condition Eq. (2.15). Since we solve the Yang-Mills equations in temporal axial gauge we need to transform them to Coulomb gauge first before computing the statistical propagator. This can be achieved by means of various methods. It is important to note that fixing to Coulomb gauge in Minkowski spacetime at a fixed time t is basically the same numerical problem as Landau gauge fixing in Euclidean spacetime. Many publications exist on that topic and we refer to [70] for a review.

We briefly summarise some relevant technical details about our implementation of Coulomb

[3] In Appendix D we demonstrate numerically that this is indeed the case.

gauge fixing. A measure for the precision with which a given lattice field configuration satisfies the Coulomb gauge condition at a particular time t we employ the quantity

$$e_2 := \frac{1}{N^3} \sum_{\mathbf{x}} \sum_{b=1}^{3} \left[(\hat{\nabla} \cdot \hat{\mathbf{A}})^b(t, \mathbf{x}) \right]^2 \tag{4.19}$$

as defined in [70]. Here, $\hat{A}$ denotes the dimensionless lattice gauge field defined in Eq. (2.48) and the derivatives indicated by $\hat{\nabla}$ are computed as finite differences, *i.e.*

$$(\hat{\nabla} \cdot \hat{\mathbf{A}})^b = \sum_j \Big(\hat{A}^b_j(t, \mathbf{x} + \hat{j}) - \hat{A}^b_j(t, \mathbf{x}) \Big) \,. \tag{4.20}$$

Obviously, perfect Coulomb gauge corresponds to $e_2 = 0$ in the continuum limit. In the present work, all data referred to as Coulomb gauge have been computed from field configurations with $e_2 < 10^{-12}$.

The Coulomb gauge condition (2.15) fixes the gauge only up to a global gauge transform. The freedom to carry out the latter is related to the conservation of colour charges. We leave this remaining gauge freedom unfixed in order not to violate Eq. (3.6). This does not pose any problems as long as only equal-time quantities are computed in Coulomb gauge [11].

Our gauge fixing procedure is an implementation of the stochastic overrelaxation algorithm described in [70] applied to a three-dimensional configuration at fixed time. The efficiency of the gauge fixing procedure is crucial for the feasibility of the computations in this chapter. Therefore, it is imperative to experiment with the numerical value of the overrelaxation parameter ω introduced in [70]. For the large lattices of 64^3 to 128^3 sites employed in the investigations in this Chapter, the optimum value of ω turned out to be $\omega \simeq 0.85 - 0.95$. Of course, we keep a copy of the configuration in temporal axial gauge in the memory in order to be able to further evolve the system in time with the methods discussed in Section 2.3. As an aside, we mention that gauge fixing by stochastic overrelaxation can easily be parallelised, which has been exploited in our implementation. It is interesting in this context to report that the convergence of our gauge-fixing procedure is very slow at the time when the instabilities saturate. This might be related to the fact that the field configurations undergo dramatic changes at this point. Due to the narrow width $\Delta_z \ll \Delta_x$ in the initial state (3.2) their $z-$ dependence is initially not very pronounced, which is altered when Fourier modes with $p_z \neq 0$ become populated to a perceivable extent. Since this is of no direct relevance to the ensuing discussion of the fixed point we will not study this phenomenon any further, though.

Fig. 4.1 exemplifies the Fourier spectra of the Coulomb gauge correlation function. It shows snapshots of the equal-time correlation function defined in Eq. (4.17) at different instants of time

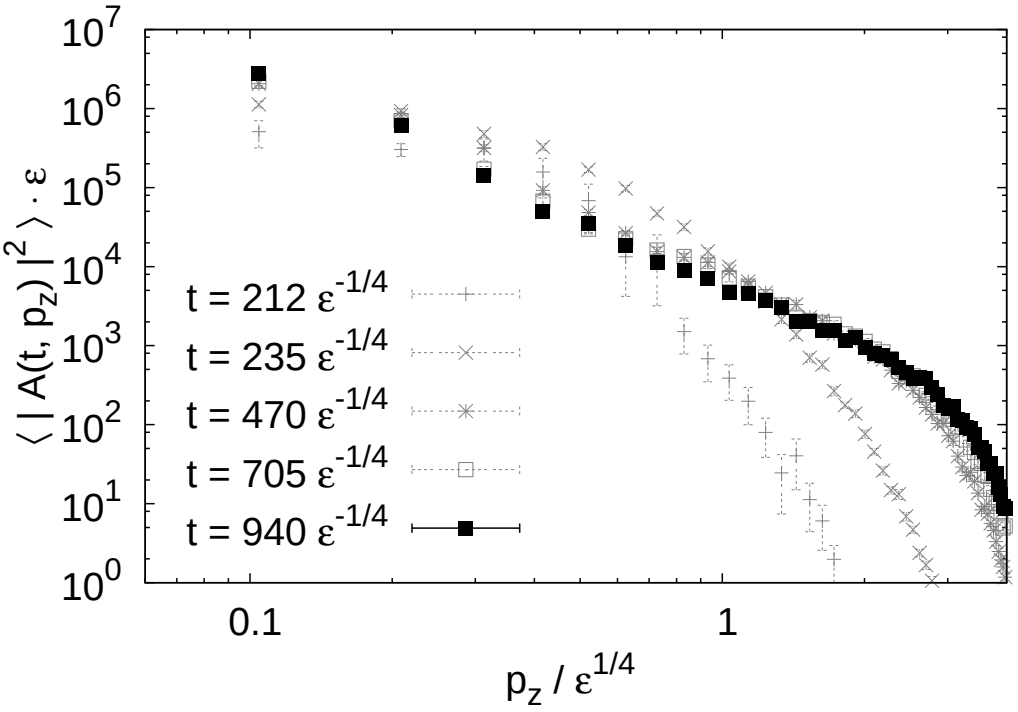

Figure 4.1: The Fourier spectrum of the equal-time gauge field correlation function Eq. (4.14) in Coulomb gauge. This plot visualises how the system approaches the quasi-stationary regime after the saturation of plasma instabilities. See the text for further explanations.

as a function of the momentum's absolute value[4] for **p** parallel to the z- axis. The data is plotted in a double-logarithmic fashion. The Lorentz index of the gauge field corresponds to transverse directions (*i.e.* x- / y- axis); note that in Coulomb gauge $A_z(t, \mathbf{p})$ is zero anyway for $\mathbf{p} \parallel \hat{z}$, which is satisfied numerically to very high precision. The earliest time for which the spectrum is plotted in Fig. 4.1 corresponds to a time shortly after the saturation of instabilities (Cf. Fig. 3.3 which shows that saturation takes place at approximately $150\,\epsilon^{-1/4}$.). The data shown in Fig. 4.1 indicates that the spectrum becomes quasi-stationary at times of order $t \sim 1000\,\epsilon^{-1/4}$ and seems to follow a power law for intermediate momenta. In temporal axial gauge, the spectrum of (4.14) becomes quasi-stationary as well but does not show power-law behaviour.

The results from Fig. 4.1 lead us to focus on the Coulomb gauge correlation functions for times $t \gtrsim 1000\,\epsilon^{-1/4}$. In the following, we fit their slope in order to establish the presence of nonthermal power-law spectra and extract their spectral index κ as introduced via Eqns. (4.12) and (4.15) in a systematic way.

[4]This is the lattice momentum computed according to Eq. (3.1).

We numerically determine κ as follows. In each run data for $A_j^a(t, \mathbf{p})$, which is required in the computation of Eq. (4.17), is saved for momenta parallel to all of the three coordinate axes[5]. The simulation is repeated for twenty different initial conditions[6] generated from the ensemble (3.2), thus allowing to approximate the ensemble average in Eq. (4.17). We carry out a χ^2- fit [133], fitting a straight line to the logarithm of (4.17) as a function of the logarithm of the momentum's absolute value. As it is obvious from Eq. (4.15), the slope of the curve yields an estimate for $\kappa+1$. We carry out the fit individually for transverse and longitudinal momenta in order to take into account the different dynamics of these modes and to check to what extent the configurations can be considered isotropic. The values of χ^2 per degree of freedom for the individual fits are in the range of 0.5 to 2, which provides confidence in the validity of the power-law ansatz. The domain of $|\mathbf{p}|$ that we employ for the fit is chosen as follows. For longitudinal momenta we choose $p_z \in [0.6\,\epsilon^{1/4}, 2.0\,\epsilon^{1/4}]$ because at early times there are obvious deviations from a power-law shape at lower and higher momenta, as can be seen from the data shown in Fig. 4.1. Transverse momentum spectra show a clear power law over a larger domain already at earlier times and hence we fit those spectra on the domain $|\mathbf{p}| \in [0.6\,\epsilon^{1/4}, 3.0\,\epsilon^{1/4}]$ providing more data points to fit to[7].

The results of individual fits to $A_y(t, p_x)$ and $A_y(t, p_z)$ are presented in Fig. 4.3. Several important observations can be made there. Firstly, transverse and longitudinal spectra[8] yield incompatible estimates for κ at early times. This can be explained by the different dynamics in these modes. While the transverse modes ($\mathbf{p} \perp \hat{z}$) are strongly populated already at initial times, the longitudinal ones are only filled up by the instabilities and the subsequent cascade at a later point in the time evolution, as can be inferred from Fig. 4.1. For $t \gtrsim 1000\,\epsilon^{-1/4}$ these differences disappear and one can consider the system as at least approximately isotropic. The isotropization of the system is also confirmed by the late-time spectra shown in Fig. 4.2. It demonstrates that the system "forgets" about the initial anisotropy at late times; deviations are only discernible at the highest and lowest momenta available on the lattice. We emphasise the significance of this observation for the subsequent analytical investigations because it implies that the correlation functions possess the symmetry properties (4.5). The second important observation from Fig. 4.3 is that it provides good evidence for a non-thermal fixed point. For times from approx. $1000\,\epsilon^{-1/4}$

[5]We have not binned the correlation functions w. r. t. the absolute value of the momentum because that would not have allowed to check the degree of isotropy of the configurations.

[6]The size of the sample is somewhat smaller than of the one used for the investigation of plasma instabilities in Chapter 3. This is because the present computation are far more computationally demanding owing to the larger volume, the longer time evolution and in particular the gauge fixing.

[7]This is the reason why the error bars on the estimates for $\kappa(t)$ in Fig. 4.3 are slightly smaller for $F(t, p_T)$, as a discerning look will reveal.

[8]In this context, "transverse" and "longitudinal" are understood to mean perpendicular and parallel to the axis of anisotropy singled out by the initial conditions (3.2). This is not to be confused with the notion of transversality pertaining to the Coulomb gauge condition Eq. (2.15).

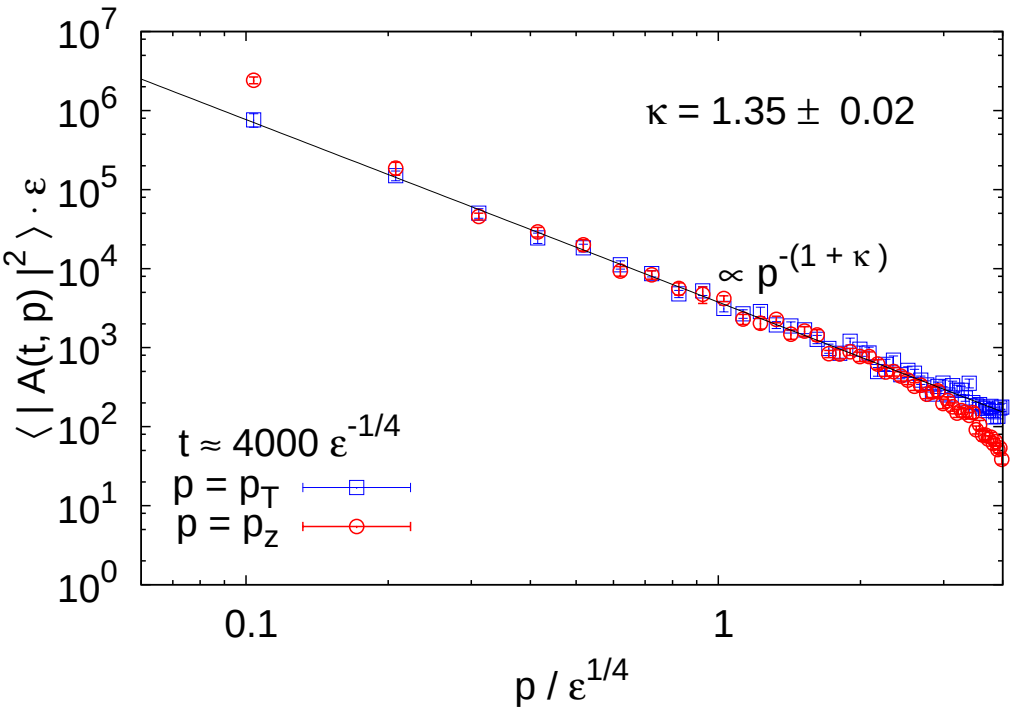

Figure 4.2: The spectrum of the equal-time gauge field correlation function (4.14) at late times for momenta parallel (red circles) and perpendicular (blue squares) to the axis of anisotropy. The solid line represents the overall result Eq. (4.21) for the occupation number exponent κ. Note that the deviations from isotropy in the lowest and highest attainable momenta are hardly visible. The values of the momentum as quoted on the abscissa give the momentum computed from Eq. (3.1).

to $4500\,\epsilon^{-1/4}$ the slopes of the spectra are nearly constant, as should be the case at a fixed point. Moreover, the all estimates of the spectral index κ are clearly incompatible with 1 which is found in classical thermal equilibrium.

Next, we average the individual estimates for κ over transverse and longitudinal directions[9]. This yields the estimates for $\kappa(t)$ plotted in Fig. 4.4. The error bars in that figure have been determined as the statistical errors from averaging the individual estimates for the spectral index at each time[10]. The large error at $\simeq 500\,\epsilon^{-1/4}$ reflects the fact that transverse and longitudinal spectra are qualitatively different at this time and thus the slopes fitted to transverse and longitudinal spectra cannot be averaged in a meaningful way, in fact (Also confer the discussion of

[9]Besides the data underlying Fig. 4.3 we also use spectra for $A_x(t, p_z)$ and $A_z(t, p_x)$. That is, the results that are presented in Fig. 4.4 are based on more values than included in Fig. 4.3.

[10]Computing the errors on the data in Fig. 4.4 from the error estimates of the individual fits using Gauss' error propagation formula yields comparable results. A discernible deviation occurs only at $t \simeq 500\,\epsilon^{-1/4}$ but this is irrelevant for the reasons outlined in the text.

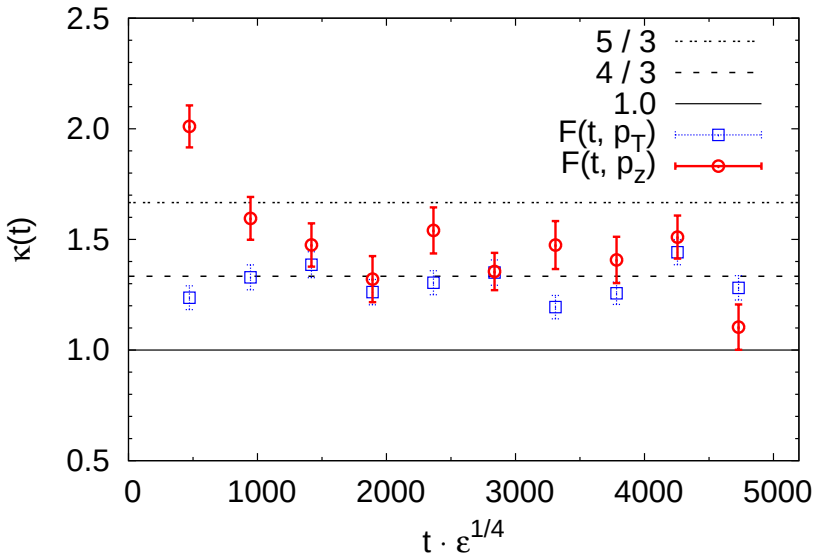

Figure 4.3: Results for κ as obtained from fits to equal-time correlation functions (4.14) of $A_y(t, \mathbf{p})$ (again averaged over colour indices). The red circles give the results for momenta parallel to the $z-$ axis while the blue squares were obtained for momenta with $p_z = 0$. The dashed and the dotted line represent the analytical results (4.49) and (4.50) from Section 4.2. At all times, the results are clearly incompatible with thermal equilibrium which corresponds to $\kappa = 1$ as given by the solid line. The significant deviation between the fit results at early times is due to the different dynamics of these modes; confer the text for further explanations. This confirms that the system is approximately isotropic for $t \gtrsim 1000\, \epsilon^{-1/4}$, as stated in the discussion of Fig. 4.2.

Fig. 4.3.). Fig. 4.4 reveals the presence of the fixed point in an even more striking way than Fig. 4.3. Obviously, the system remains in a configuration characterised by power-law spectra with an obviously non-thermal (*i.e.* $\kappa \neq 1$) exponent for a long period of time. At the latest available time the drop in $\kappa(t)$ could indicate the system's final approach to thermal equilibrium which features a spectrum with $\kappa = 1$. However, the available data do not allow to draw conclusions on later stages of the thermalisation process. We have carried out a simulation running to twice as long a time with only a single ensemble member. The spectra obtained in that computation do not provide any indication for the system moving away from the fixed point.

Having accumulated compelling evidence for the presence of a fixed point it is justified to average the values of $\kappa(t)$ over the quasi-stationary regime in time. Averaging the data plotted in Fig. 4.4 excluding the first and last data point yields

$$\kappa = 1.35 \pm 0.02 \,, \tag{4.21}$$

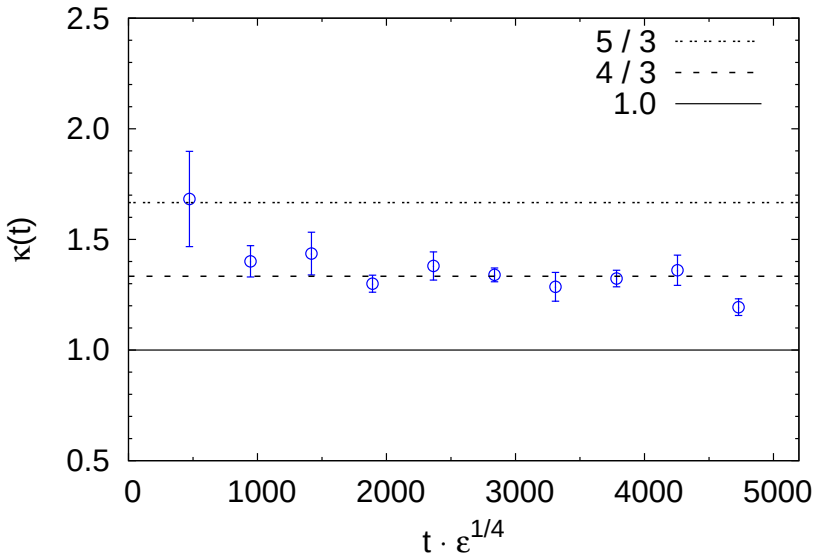

Figure 4.4: Fit results for κ as a function of time. The error bars quote the statistical errors as from averaging over different spectra. The dotted and dashed lines represent the analytical results (4.49) and (4.50), respectively. The solid line corresponds to classical thermal equilibrium.

where again the error estimate has been computed as the statistical error resulting from the computation of the average. We will further comment on the error estimates below. At this point we note that the result (4.21) is in very good agreement with the analytical result (4.50) that will be derived in Section 4.2. Moreover, comparing the late-time spectra to the curve corresponding to the fit result as done in Fig. 4.2 demonstrates the accuracy of the fit.

We now turn to discuss the error estimate for κ in Eq. (4.21) in more detail. First, we have to estimate the uncertainty introduced by choosing (i) a certain range of momentum to carry out the fits and (ii) a particular time interval over which $\kappa(t)$ is averaged when computing (4.21). It turns out that in both cases changes in the choice of data taken into account alter the result (4.21) by an amount of the order of the statistical error estimate quoted there. We have checked this by (i) fitting the spectra on an extended range with $0.2\,\epsilon^{1/4}$ as the lower bound and (ii) recalculating the temporal average from the data plotted in Fig. 4.2 discarding two more data points (That is, taking into account only $\kappa(t)$ for $1000\,\epsilon^{-1/4} < t < 4000\,\epsilon^{-1/4}$.). This gives us confidence that the arbitrariness introduced in the choices we had to made is negligible.

A source for systematic error is posed by the fact that the spectra are slightly steeper when the momentum is chosen in parallel alignment to the z- axis than the corresponding transverse momentum spectra, as can be seen in Fig. 4.3. This is due to the different dynamics taking place

in longitudinal and transverse modes, thereby reflecting the anisotropy introduced by the initial conditions (3.2). However, even if this difference is employed to estimate the error of (4.21) the relative error will still be less than ten per cent. The reliability of our error estimates is confirmed by the analysis of spectra in thermal equilibrium in Section D.

We comment on the numerical stability of the results. First, we have run simulations also on smaller lattices of 64^3 sites (as compared to the 128^3 lattices on which the data presented here were generated). This computation produced compatible value for κ with a slightly larger error, however. This is to be expected because the number of data points for a given momentum range is half as big on the smaller lattice. Furthermore, we have made a single run on a 256^3 lattice and compared the spectra to a power-law curve with the exponent (4.21). Again, the two results were in agreement and did not provide any hint of a change in κ. Thus we conclude that the result for κ is not affected by serious finite-volume effects. When increasing the gauge fixing precision to even smaller values of e_2 (cf. Eq. (4.19)) alterations of the spectra are only discernible at the modes of lowest momentum. Since these have not been taken into account in the χ^2- fit anyway, we are confident that our results do indeed represent perfect Coulomb gauge, *i.e.* $e_2 \to 0$. Finally, we have carried out a few simulations in which the parameters Δ_x and the energy density were changed. The late-time Coulomb gauge spectra obtained from those computations were also in agreement with the power-law shape presented above. Summarising, there is ample evidence for the numerical stability of the central result (4.21).

To summarise, the following conclusions have to be drawn. First, the system exhibits quasi-stationary behaviour, as expected at a fixed point. The fixed point is characterised by power-law spectra in Coulomb gauge whose spectral index (i) is in good agreement with one of the analytically predicted values (cf. Eq. (4.50)) and (ii) is definitely non-thermal. Second, our data clearly rule out $\kappa = 2$ as well as $\kappa = 1$ which have been reported in other publications [18, 19, 126, 149]. Third, the presence of the fixed point and the numerical value of the spectral index are similar to the properties of fixed points encountered in parametric resonance in scalar field theories [41].

Besides the calculations whose results have been reported upon in this Section a lot of effort was made in order to characterise the fix point by other quantities than the statistical propagator in Coulomb gauge. However, we have not found power-law spectra in neither gauge-invariant quantities (*e.g.* plaquette-plaquette correlators) nor gauge-field correlation functions in temporal axial gauge. At least, both kinds of quantities do not display any discernible time dependence in the fixed-point regime anymore. At this point it is interesting to refer to Section D of the Appendix where it is demonstrated that the statistical propagator in thermal equilibrium only exhibits the expected spectrum ($\kappa = 1$) in Coulomb gauge but not in temporal axial gauge. Un-

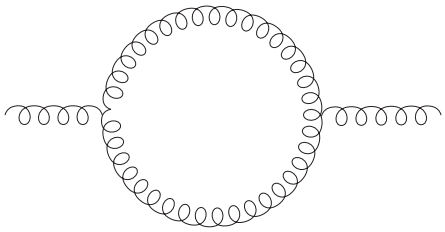

Figure 4.5: The gluonic contribution to the gluon self-energy at order g^2. The curly lines represent dressed gluon propagators.

derstanding the fixed point in terms of gauge invariant quantities (or alternatively understanding the gauge dependence of the spectra) remains an intriguing task for future studies.

4.2 Analytical approach to turbulence

In this Section we strive for an analytical understanding of the numerical result (4.21) presented in Section 4.1 analytically in the framework of the 2PI effective action. Our approach is to adopt the methods of [39, 41] developed for nonthermal fixed points in scalar theories to non-Abelian gauge theories. For the sake of simplicity we stick to SU(2) Yang-Mills theory which we have also studied in the numerical simulations presented in Section 4.1. Given that we are predominantly interested in the UV properties of the theory we expect that the problem is amenable to perturbation theory, as suggested by asymptotic freedom [83, 132]. Therefore, we will employ a perturbative expansion of the self-energy in powers of the non-Abelian gauge coupling g. In this limit the 2PI effective action scheme is effectively equivalent to resummed perturbation theory.

The starting point for our treatment is the identity

$$\tilde{\Pi}^{\mu\nu}_{(\rho)ab}(p)\,\tilde{F}^{ba}_{\nu\mu}(p) - \tilde{\Pi}^{\mu\nu}_{(F)\,ab}(p)\,\tilde{\rho}^{ba}_{\nu\mu}(p) \;=\; 0\,, \tag{4.22}$$

which has been derived using functional renormalisation group methods in [39]. Eq. (4.22) is at the heart of the investigation of nonthermal fixed points. It is reminiscent the familiar statement in the language of Boltzmann equations that gain and loss terms mutually cancel in stationary states. In fact, the latter can be derived from the more general Eq. (4.22) in the on-shell limit. Employing the KMS relation it is straightforward to check that this identity is satisfied in thermal equilibrium. In the following however, we will search for scaling solutions of $\tilde{F}_{\mu\nu}(p)$ and $\tilde{\rho}_{\mu\nu}(p)$ of the kind (4.12) which in general do not fulfil the KMS relation.

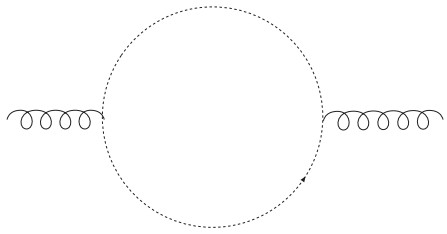

Figure 4.6: The $O(g^2)$- ghost contribution to the gluon self-energy.

With the propagators being diagonal in colour indices (cf. Eq. (4.1)) the one-loop contribution to the gluon self-energy factors into a tensor part containing all colour indices and another factor which is completely independent of colour indices. If the approximation to the self-energy under consideration possesses this property one finds upon contraction of the colour indices that the fixed-point identity (4.22) is equivalent[11] to

$$\tilde{\Pi}^{\mu\nu}_{(\rho)}(p)\,\tilde{F}_{\nu\mu}(p) - \tilde{\Pi}^{\mu\nu}_{(F)}(p)\,\tilde{\rho}_{\nu\mu}(p) \;=\; 0\;. \tag{4.23}$$

When evaluated at a fixed point, Eqns. (4.22) and (4.23) are trivially satisfied when integrated over the spatial components $\mathbf{p}$ of the momentum $p = (p^0, \mathbf{p})$. Hence the following equation represents a necessary criterion for the propagators $\tilde{F}$ and $\tilde{\rho}$ to represent a fixed-point solution:

$$\int d^3p \left\{ \tilde{\Pi}^{\mu\nu}_{(\rho)ab}(p)\,\tilde{F}^{ba}_{\nu\mu}(p) - \tilde{\Pi}^{\mu\nu}_{(F)\;ab}(p)\,\tilde{\rho}^{ba}_{\nu\mu}(p) \right\} = 0\;. \tag{4.24}$$

Note that an additional integration over p^0 would render the equation trivially fulfilled due to the symmetry properties (4.11) of the spectral function ρ and the imaginary part of the self-energy $\tilde{\Pi}^{\mu\nu}_{(\rho)ab}(p)$ (The latter is anti-symmetric from its definition in Eq. (2.28).). When considered from a quasi-particle point of view, *i.e.* assuming the spectral function to be on-shell, the integration in Eq. (4.24) has the effect of picking up the only non-zero contributions to the integrand. It has emerged from [41] that Eq. (4.24) allows to access nonthermal fixed points in a convenient way.

Our strategy to search for nonthermal fixed points is the following. First, we approximate the self-energy perturbatively. Subsequently, we look for zeroes in Eq. (4.24) assuming a power-law as in Eq. (4.12) for the spectral function and the statistical propagator.

The leading order contributions to the (non-local) self-energies $\Pi_{(F)}$ and $\Pi_{(\rho)}$ in a perturbative setting arise from the purely gluonic diagram depicted in Fig. 4.5 and the ghost loop shown in Fig. 4.6. These contributions are of order g^2. In this work we neglect the ghost contributions

[11] Of course, this tacitly assumes that the result of the colour contraction is non-zero, which applies to all cases considered in this work.

assuming that we can work in a ghost free gauge[12]. Therefore, we do not consider the ghost diagram any further in the following.

It is important to stress that the propagator lines in Figs. 4.5 are fully resummed propagators, as implied by the use of the 2PI effective action. Therefore, these diagrams actually contain contributions up to infinite order in g. Including higher order diagrams in the gauge coupling thus has the effect that more, topologically distinct diagrams are included in the resummation.

Before turning to the analysis of the fixed point in terms of one-loop self energies we introduce some pieces of notation. For momentum integrals we use the shorthands

$$\int_q \equiv \int \frac{d^4q}{(2\pi)^4} \qquad \text{and} \qquad \int_{\mathbf{q}} \equiv \frac{d^3q}{(2\pi)^3} \,. \tag{4.25}$$

Furthermore, we define

$$V_3^{\mu\kappa\rho}(p,k,q) := g^{\mu\kappa}(p-k)^\rho + g^{\kappa\rho}(k-q)^\mu + g^{\rho\mu}(q-p)^\kappa \,, \tag{4.26}$$

which allows to write the perturbative three-gluon vertex as

$$V_3^{\mu\kappa\rho,abc}(p,k,q) = g\epsilon^{abc} V_3^{\mu\kappa\rho}(p,k,q) \,. \tag{4.27}$$

From this it is obvious that the colour structure of all vertices and propagators appearing in Eq. (4.22) to order g^2 can be factored out and pulled out of the integral in Eq. (4.24). Thus we can ignore the colour structure and stick to the slightly simpler version of the fixed-point identity (4.23) in the analysis of the gluonic one-loop diagram. We note in passing that the three-gluon vertex has the following, trivial scaling property:

$$V_3^{\mu\kappa\rho}(lp,lk,lq) = lV_3^{\mu\kappa\rho}(p,k,q) \,. \tag{4.28}$$

Furthermore, it possesses the symmetries

$$\begin{aligned} V_3^{\mu\kappa\rho}(p,k,q) &= V_3^{\kappa\rho\mu}(k,q,p) \\ V_3^{\mu\kappa\rho}(p,k,q) &= -V_3^{\mu\rho\kappa}(p,q,k) \\ V_3^{\mu\kappa\rho}(p,k,q) &= -V_3^{\mu\kappa\rho}(-p,-k,-q) \,. \end{aligned} \tag{4.29}$$

For the sake of completeness we recall the behaviour of the Dirac- δ function under rescaling of its argument with $l \neq 0$:

$$\delta^{(d)}(l\,p) = \frac{1}{|l|^d}\,\delta^{(d)}(p) \,. \tag{4.30}$$

[12] An alternative could be to employ the frozen-ghost formalism [65, 71, 102].

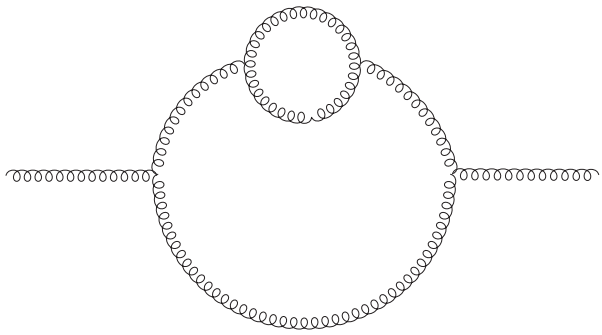

Figure 4.7: This diagram visualises how the $O(g^4)$- contribution to the gluon self-energy from Fig. 4.5 is isolated by iteratively replacing propagator using the identities (4.10). Note that this this diagram cannot be obtained by functional differentiation of any term in the 2PI effective action, as can easily be seen by connecting the external propagator lines. The contributions of this diagram to the symmetric and the anti-symmetric part of the Wigner transformed gluon self-energy are denoted by $\tilde{L}_{(F)}$ and $\tilde{L}_{(\rho)}$ in the text.

The explicit expressions for the Wigner- transformed self-energies at order $O(g^2)$ corresponding to Fig. 4.5 are given by

$$\begin{aligned}\tilde{\Pi}^{\mu\nu}_{(F)}(p) &= -g^2 \int_{k,q} (2\pi)^4 \, \delta^{(4)}(p+k+q) V_3^{\mu\alpha\gamma}(p,k,q) V_3^{\nu\beta\delta}(p,k,q) \left[\tilde{F}_{\beta\alpha}(k) \tilde{F}_{\delta\gamma}(q) + \frac{1}{4} \tilde{\rho}_{\beta\alpha}(k) \tilde{\rho}_{\delta\gamma}(q) \right] \\ \tilde{\Pi}^{\mu\nu}_{(\rho)}(p) &= g^2 \int_{k,q} (2\pi)^4 \, \delta^{(4)}(p+k+q) V_3^{\mu\alpha\gamma}(p,k,q) V_3^{\nu\beta\delta}(p,k,q) \left[\tilde{F}_{\beta\alpha}(k) \tilde{\rho}_{\delta\gamma}(q) + \tilde{\rho}_{\beta\alpha}(k) \tilde{F}_{\delta\gamma}(q) \right] .\end{aligned} \tag{4.31}$$

Plugging these into the integrated fixed-point identity (4.24) yields the following for the g^2-contribution:

$$\begin{aligned} 0 &\stackrel{!}{=} \int d^3p \left\{ \tilde{\Pi}^{\mu\nu}_{(\rho)}(p) \tilde{F}_{\nu\mu}(p) - \tilde{\Pi}^{\mu\nu}_{(F)}(p) \tilde{\rho}_{\nu\mu}(p) \right\} \\ &= g^2 \int d^3p \int_{k,q} (2\pi)^4 \, \delta^{(4)}(p+k+q) V_3^{\mu\kappa\rho}(p,k,q) V_3^{\nu,\lambda\sigma}(p,k,q) \Big\{ \\ &\qquad \left[\tilde{F}_{\kappa\lambda}(k) \tilde{\rho}_{\rho\sigma}(q) + \tilde{\rho}_{\kappa\lambda}(k) \tilde{F}_{\rho\sigma}(q) \right] \tilde{F}_{\nu\mu}(p) + \left[\tilde{F}_{\kappa\lambda}(k) \tilde{F}_{\rho\sigma}(q) + \frac{1}{4} \tilde{\rho}_{\kappa\lambda}(k) \tilde{\rho}_{\rho\sigma}(q) \right] \tilde{\rho}_{\nu\mu}(p) \Big\} \end{aligned} \tag{4.32}$$

Without loss of generality, we assume $p^0 > 0$ from now on.

The next step in order in the search for nonthermal scaling solutions would now be to plug in the ansatz (4.12). However, the contribution to (4.32) at order g^2 is kinematically suppressed, which is to a big extent analogous to the vanishing of the g^2- contribution to the Boltzmann equation in quantum electrodynamics [30, 31]. This can easily be seen in the on-shell limit of

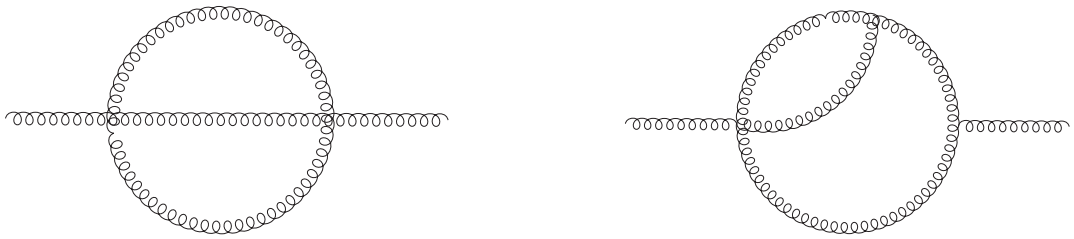

(a) "Setting sun" (b) "Squint"

Figure 4.8: Contributions to the gluon self-energy at order $O(g^4)$. The symmetric and anti-symmetric contributions of (a) are denoted by $\tilde{S}_{(F)}, \tilde{S}_{(\rho)}$ in the text, those of (b) by $\tilde{Q}_{(F)}, \tilde{Q}_{(\rho)}$.

massless particles which applies to gluons in the perturbative regime considered here where $\tilde{F}_{\mu\nu}$ and $\tilde{\rho}_{\mu\nu}$ are proportional to $\delta(p^2) = \delta(p_0^2 - \mathbf{p}^2)$, implying that the only non-zero contributions arise from $p_0 = \pm|\mathbf{p}|$. Combining the on-shell condition with the δ- function $\delta^{(4)}(p + k + q) = \delta(p_0 + k_0 + q_0)\delta^{(3)}(\mathbf{p} + \mathbf{k} + \mathbf{q})$ in the integrand of Eq. (4.32) one finds that the only contributions stem from solutions to the kinematic condition

$$-p_0 = k_0 + q_0 = |\mathbf{k}| + |\mathbf{q}| = \pm|\mathbf{p}| = \pm|\mathbf{k} + \mathbf{q}| \,.$$

For this to admit a solution, $\mathbf{k}$ and $\mathbf{q}$ must be either parallel or anti-parallel by virtue of the Cauchy-Schwartz inequality. Hence only purely collinear scattering processes can occur and these are thus phase-space suppressed.

Given that the $O(g^2)$- contribution to the integrand of Eq. (4.32) is suppressed we continue the search for fixed-point solutions at order g^4. At this order, there are several diagrams contributing to the self-energy. These are depicted in Figs. 4.7, 4.8 and 4.9. As before, we neglect the contributions of ghosts. Note that the diagram shown in Fig. 4.7 merely isolates the order g^4 contribution that is already included in the one-loop diagram from Fig. 4.5. This can be seen by replacing one propagator line using Eqns. (4.10). We underscore again that the propagator lines represent fully dressed propagators in the 2PI resummation scheme. The diagram in Fig. 4.7 actually does not possess a functional anti-derivative contributing to the 2PI effective action; connecting the external lines does not result in a two-particle irreducible diagram.

The diagrams shown in Figs. 4.8 and 4.9 represent the common $O(g^4)$- contributions to the gluon self-energy. It is only necessary to consider the former, though, because the latter are included in the other $O(g^4)$- contributions through a cancellation identity [31]. Note that cutting the diagram of Fig. 4.7 produces the matrix elements for the s-, t- and u- channel in $2 \leftrightarrow 2$ scattering in the on-shell limit. Cutting the "setting-sun diagram" (Fig. 4.8(a)) yields the corrresponding

contribution from the four-gluon vertex. The "squint" displayed in Fig. 4.8(b) does not yield a contribution to $2 \leftrightarrow 2$ scattering.

Before reproducing the details of the calculation we briefly summarise our way to engage the full g^4- analysis, which is quite involved. Since the self-energies are a sum of the diagrammatic contributions we can split up the task to find a solution to Eq. (4.24) at order g^4 in the gauge coupling by considering the terms arising from each of the above diagrams individually. Denoting the contraction of Lorentz and colour indices in Eq. (4.22) by "$\cdot$" for the sake of brevity and introducing the symbols $\tilde{L}_{(F)}, \tilde{L}_{(\rho)}, \tilde{S}_{(F)}, \tilde{S}_{(\rho)}$ and $\tilde{Q}_{(F)}, \tilde{Q}_{(\rho)}$ for the symmetric and anti-symmetric self-energy contributions of the one-loop diagram (Fig. 4.7), the setting-sun (Fig. 4.8(a)) and the squint (Fig. 4.8(b)), respectively, we can split up the fixed-point identity (4.22) into several integrals:

$$\begin{aligned} 0 &= \int d^3p \left\{ \tilde{\Pi}_{(\rho)}(p) \cdot \tilde{F}(p) - \tilde{\Pi}_{(F)}(p) \cdot \tilde{\rho}(p) \right\} \\ &= \int d^3p \left\{ \left(\tilde{L}_{(\rho)}(p) + \tilde{S}_{(\rho)}(p) + \tilde{Q}_{(\rho)}(p) \right) \cdot \tilde{F}(p) - \left(\tilde{L}_{(F)}(p) + \tilde{S}_{(F)}(p) + \tilde{Q}_{(F)}(p) \right) \cdot \tilde{\rho}(p) \right\} \\ &= \int d^3p \left\{ \tilde{L}_{(\rho)}(p) \cdot \tilde{F}(p) - \tilde{L}_{(F)}(p) \cdot \tilde{\rho}(p) \right\} + \int d^3p \left\{ \tilde{S}_{(\rho)}(p) \cdot \tilde{F}(p) - \tilde{S}_{(F)}(p) \cdot \tilde{\rho}(p) \right\} \\ &\qquad + \int d^3p \left\{ \tilde{Q}_{(\rho)}(p) \cdot \tilde{F}(p) - \tilde{Q}_{(F)}(p) \cdot \tilde{\rho}(p) \right\} \end{aligned} \tag{4.33}$$

We deal with the individual integrals in the following order:

1. We search for zeroes in the contribution of Fig. 4.7, that is, the integrals featuring $\tilde{L}$. We find scaling solutions of the kind (4.12) in the classical limit. Keeping the quantum terms as well we can show that no scaling solutions persist in the full quantum theory.

2. We check that the contributions of the diagrams in Fig. 4.8 (*i.e.* the integrals appearing in Eq. (4.33) with $\tilde{S}$ and $\tilde{Q}$ in the integrand) also vanish in the classical limit for the same values of the occupation number exponent κ.

In this way we will be able to demonstrate that there is a nonthermal fixed point in the classical limit. We do not need to compute the quantum contributions to the setting-sun and the squint diagram explicitly because we will already see from the diagram in Fig. 4.5 that the quantum terms destroy the fixed-point solution[13].

We commence by analysing the $O(g^4)$- contribution to the one-loop diagram which is depicted in Fig. 4.7. Mathematically, this is obtained by replacing one propagator line in each of

[13]This argumentation is not a hundred percent airtight. Though not very likely, the quantum terms from the $\tilde{L}-, \tilde{S}-$ and $\tilde{Q}-$ contributions could mutually cancel.

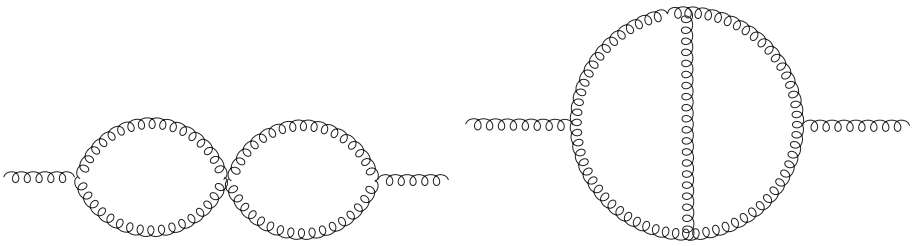

(a) (b)

Figure 4.9: Contributions to the gluon self-energy at order $O(g^4)$ which are implicitly included in the diagrams of Figs. 4.5 and 4.8 by virtue of a cancellation identity [31].

the terms in Eq. (4.32) by virtue of the identity (4.10). We choose to replace all propagators depending on the internal momentum k in Eq. (4.32). This yields

$$0 = g^2 \int d^3p \int_{k,q} \delta^{(4)}(p+k+q) V_3^{\mu\kappa\rho}(p,k,q) V_3^{\nu\lambda\sigma}(p,k,q)\, \tilde{G}^R_{\kappa\alpha}(k)\tilde{G}^A_{\beta\lambda}(k) \Big\{ \\ \Big[\tilde{\Pi}^{\alpha\beta}_{(F)}(k)\tilde{\rho}_{\rho\sigma}(q) + \tilde{\Pi}^{\alpha\beta}_{(\rho)}(k)\tilde{F}_{\rho\sigma}(q)\Big]\tilde{F}_{\nu\mu}(p) + \Big[\tilde{\Pi}^{\alpha\beta}_{(F)}(k)\tilde{F}_{\rho\sigma}(q) + \frac{1}{4}\,\tilde{\Pi}^{\alpha\beta}_{(\rho)}(k)\tilde{\rho}_{\rho\sigma}(q)\Big]\tilde{\rho}_{\nu\mu}(p)\Big\} \tag{4.34}$$

whose right hand side is already of order g^4 because the leading contribution to $\tilde{\Pi}_{(F)}$ and $\tilde{\Pi}_{(\rho)}$ is proportional to g^2. Upon replacing the self-energies by the one-loop expressions (4.31) one obtains

$$\begin{aligned} 0 = g^4 \int d^3p \int_{k,q,r,s} & \delta^{(4)}(p+k+q)\,\delta^{(4)}(k+r+s) \\ & \times V_3^{\mu\kappa\rho}(p,k,q) V_3^{\nu\lambda\sigma}(p,k,q) V_3^{\alpha\gamma\zeta}(k,r,s) V_3^{\beta\delta\tau}(k,r,s)\, \tilde{G}^R_{\kappa\alpha}(k)\tilde{G}^A_{\beta\lambda}(k)\Big\{ \\ & \underbrace{-\tilde{\rho}_{\rho\sigma}(q)\tilde{F}_{\nu\mu}(p)\Big(\tilde{F}_{\gamma\delta}(r)\tilde{F}_{\zeta\tau}(s) + \frac{1}{4}\,\tilde{\rho}_{\gamma\delta}(r)\tilde{\rho}_{\zeta\tau}(s)\Big)}_{\textbf{(I)}} \\ & \underbrace{+\tilde{\rho}_{\zeta\tau}(s)\tilde{F}_{\gamma\delta}(r)\Big(\tilde{F}_{\rho\sigma}(q)\tilde{F}_{\nu\mu}(p) + \frac{1}{4}\,\tilde{\rho}_{\rho\sigma}(q)\tilde{\rho}_{\nu\mu}(p)\Big)}_{\textbf{(II)}} \\ & \underbrace{+\tilde{\rho}_{\gamma\delta}(r)\tilde{F}_{\zeta\tau}(s)\Big(\tilde{F}_{\rho\sigma}(q)\tilde{F}_{\nu\mu}(p) + \frac{1}{4}\,\tilde{\rho}_{\rho\sigma}(q)\tilde{\rho}_{\nu\mu}(p)\Big)}_{\textbf{(III)}} \\ & \underbrace{-\tilde{\rho}_{\nu\mu}(p)\tilde{F}_{\rho\sigma}(q)\Big(\tilde{F}_{\gamma\delta}(r)\tilde{F}_{\zeta\tau}(s) + \frac{1}{4}\,\tilde{\rho}_{\gamma\delta}(r)\tilde{\rho}_{\zeta\tau}(s)\Big)}_{\textbf{(IV)}}\Big\}\,. \end{aligned} \tag{4.35}$$

We search for zeroes of this expression by plugging in the ansatz from Eq. (4.12) and carrying out scaling transformations. This procedure, which is inspired by a similar method in the analysis of Boltzmann equations [159], is analogous to the scaling transformations applied in the case of scalar theories in [39, 41]. The main complication compared to the latter case is the more complicated tensor structure of the vertices in the gauge theory. Since the integrand of Eq. (4.35) is a sum of four terms we need to carry out three scaling transformations in order to arrange for all of these terms being of the same structure. We choose to transform the terms **(II)**, **(III)** and **(IV)** to the shape of the first term **(I)** in Eq. (4.35).

In order to transform term (**II**) we substitute the integration variables in the following way[14]:

$$
\begin{aligned}
r_0{}' &:= \frac{p_0^2}{r_0} & r_0 &= \frac{p_0^2}{r_0'} & dr_0 &= -\frac{p_0^2}{(r_0')^2}\, dr_0' \\
l_r &:= \frac{r_0}{p_0} = \frac{p_0'}{r_0'} & p_o' &:= p_0 & & \\
\mathbf{r}' &:= \frac{1}{l_r}\,\mathbf{p} & \mathbf{p} &= l_r \mathbf{r}' & d^3p &= |\, l_r\,|^3 d^3r' \\
\mathbf{p}' &:= \frac{1}{l_r}\,\mathbf{r} & \mathbf{r} &= l_r \mathbf{p}' & d^3r &= |\, l_r\,|^3 d^3p' \\
k' &:= \frac{1}{l_r}\, k & k &= l_r k' & d^4k &= |\, l_r\,|^4 d^4k' \\
q' &:= \frac{1}{l_r}\, q & q &= l_r q' & d^4q &= |\, l_r\,|^4 d^4q' \\
s' &:= \frac{1}{l_r}\, s & s &= l_r s' & d^4s &= |\, l_r\,|^4 d^4s' \ .
\end{aligned}
\tag{4.36}
$$

Note that with these definitions

$$
r = l_r p' \ , \ p = l_r r' \ , \ k = l_r k' \ , \ q = l_r q' \text{ and } \ s = l_r s' \ . \tag{4.37}
$$

Somewhat loosely speaking, the effect of the substitutions (4.36) is to swap the variables p and r. Moreover, we define

$$
\Delta := -3\kappa + 4 \tag{4.38}
$$

in order to abbreviate the exponents occurring below. Exploiting the intrinsic symmetries of $\tilde{F}$ and $\tilde{\rho}$ (cf. Eq. (4.11)), the assumption of isotropy (4.5), Eqns. (4.28) and (4.30) and the scaling

[14] Recall that we have assumed $p^0 > 0$ in the context of Eq. (4.32).

ansatz (4.12), the integral with integrand (**II**) in Eq. (4.34) can be recast in the following way:

$$
\begin{aligned}
&\int d^3p \int_{k,q,r,s} \delta^{(4)}(p+k+q)\,\delta^{(4)}(k+r+s) V_3^{\mu\kappa\rho}(p,k,q) V_3^{\nu\lambda\sigma}(p,k,q) V_3^{\alpha\gamma\zeta}(k,r,s) V_3^{\beta\delta\tau}(k,r,s) \\
&\quad \tilde{G}^R_{\kappa\alpha}(k)\tilde{G}^A_{\beta\lambda}(k)\tilde{\rho}_{\zeta\tau}(s)\tilde{F}_{\gamma\delta}(r)\left[\tilde{F}_{\rho\sigma}(q)\tilde{F}_{\nu\mu}(p) + \frac{1}{4}\tilde{\rho}_{\rho\sigma}(q)\tilde{\rho}_{\nu\mu}(p)\right] \\
&\quad \text{(substitute according to Eq. (4.37))} \\
&= \int d^3p' \int_{k',q',r',s'} \delta^{(4)}(l_r(r'+k'+q'))\,\delta^{(4)}(l_r(k'+p'+s')) \\
&\quad V_3^{\mu\kappa\rho}(l_r r', l_r k', l_r q') V_3^{\nu\lambda\sigma}(l_r r', l_r k', l_r q') V_3^{\alpha\gamma\zeta}(l_r k', l_r p', l_r s') V_3^{\beta\delta\tau}(l_r k', l_r p', l_r s') \tilde{G}^R_{\kappa\alpha}(l_r k')\tilde{G}^A_{\beta\lambda}(l_r k') \\
&\quad \tilde{\rho}_{\zeta\tau}(\mathrm{sign}(l_r)|\,l_r\,|s')\tilde{F}_{\gamma\delta}(l_r p')\left[\tilde{F}_{\rho\sigma}(l_r q')\tilde{F}_{\nu\mu}(l_r r') + \frac{1}{4}\tilde{\rho}_{\rho\sigma}(\mathrm{sign}(l_r)|\,l_r\,|q')\tilde{\rho}_{\nu\mu}(\mathrm{sign}(l_r)|\,l_r\,|r')\right] \\
&\quad \text{(use scaling assumptions and symmetries)} \\
&= \int d^3p' \int_{k',q',r',s'} |\,l_r\,|^{\Delta}\delta^{(4)}(r'+k'+q')\delta^{(4)}(k'+p'+s') \\
&\quad V_3^{\mu\kappa\rho}(r',k',q') V_3^{\nu\lambda\sigma}(r',k',q') V_3^{\alpha\gamma\zeta}(k',p',s') V_3^{\beta\delta\tau}(k',p',s') \tilde{G}^R_{\kappa\alpha}(k')\tilde{G}^A_{\beta\lambda}(k') \\
&\quad \tilde{\rho}_{\zeta\tau}(\mathrm{sign}(l_r)s')\tilde{F}_{\gamma\delta}(p')\left[\tilde{F}_{\rho\sigma}(q')\tilde{F}_{\nu\mu}(r') + \frac{|\,l_r\,|^{2\kappa}}{4}\tilde{\rho}_{\rho\sigma}(\mathrm{sign}(l_r)q')\tilde{\rho}_{\nu\mu}(\mathrm{sign}(l_r)r')\right] \\
&\quad \text{(rename dummy integration variables } q' \leftrightarrow s', \text{ use vertex symmetries Eq. (4.29))} \\
&= \int d^3p' \int_{k',q',r',s'} |\,l_r\,|^{\Delta}\delta^{(4)}(r'+k'+s')\delta^{(4)}(k'+p'+q') \\
&\quad V_3^{\kappa\mu\rho}(k',r',s') V_3^{\lambda\nu\sigma}(k',r',s') V_3^{\gamma\alpha\zeta}(p',k',q') V_3^{\delta\beta\tau}(p',k',q') \tilde{G}^R_{\kappa\alpha}(k')\tilde{G}^A_{\beta\lambda}(k') \\
&\quad \tilde{\rho}_{\zeta\tau}(\mathrm{sign}(l_r)q')\tilde{F}_{\gamma\delta}(p')\left[\tilde{F}_{\rho\sigma}(s')\tilde{F}_{\nu\mu}(r') + \frac{|\,l_r\,|^{2\kappa}}{4}\tilde{\rho}_{\rho\sigma}(\mathrm{sign}(l_r)s')\tilde{\rho}_{\nu\mu}(\mathrm{sign}(l_r)r')\right] \\
&\quad \text{(rename indices } \gamma \leftrightarrow \mu\,,\ \alpha \leftrightarrow \kappa\,,\ \zeta \leftrightarrow \rho\,,\ \delta \leftrightarrow \nu\,,\ \beta \leftrightarrow \lambda\,,\ \tau \leftrightarrow \sigma \\
&\quad \text{and use propagator symmetries)} \qquad (4.39) \\
&= \int d^3p' \int_{k',q',r',s'} |\,l_r\,|^{\Delta}\delta^{(4)}(p'+k'+q')\delta^{(4)}(k'+r'+s') \\
&\quad V_3^{\mu\kappa\rho}(p',k',q') V_3^{\nu\lambda\sigma}(p',k',q') V_3^{\alpha\gamma\zeta}(k',r',s') V_3^{\beta\delta\tau}(k',r',s') \tilde{G}^R_{\alpha\kappa}(k')\tilde{G}^A_{\lambda\beta}(k') \\
&\quad \tilde{\rho}_{\rho\sigma}(\mathrm{sign}(l_r)q')\tilde{F}_{\mu\nu}(p')\left[\tilde{F}_{\delta\gamma}(r')\tilde{F}_{\zeta\tau}(s') + \frac{|\,l_r\,|^{2\kappa}}{4}\tilde{\rho}_{\delta\gamma}(\mathrm{sign}(l_r)r')\tilde{\rho}_{\zeta\tau}(\mathrm{sign}(l_r)s')\right]. \qquad (4.40)
\end{aligned}
$$

Next, we treat the term (**III**) in Eq. (4.35) in a similar way making the substitutions

$$
\begin{aligned}
s_0{}' &:= \frac{p_0^2}{s_0} & s_0 &= \frac{p_0^2}{s_0'} & ds_0 &= -\frac{p_0^2}{(s_0')^2}\,ds_0' \\
l_s &:= \frac{s_0}{p_0} = \frac{p_0'}{s_0'} & p_o' &:= p_0
\end{aligned}
$$

$$
\begin{aligned}
\mathbf{s}' &:= \frac{1}{l_s}\,\mathbf{p} & \mathbf{p} &= l_s\mathbf{s}' & d^3p &= |\,l_s\,|^3 d^3s' \\
\mathbf{p}' &:= \frac{1}{l_s}\,\mathbf{s} & \mathbf{s} &= l_s\mathbf{p}' & d^3s &= |\,l_s\,|^3 d^3p' \\
k' &:= \frac{1}{l_s}\,k & k &= l_s k' & d^4k &= |\,l_s\,|^4 d^4k' \\
q' &:= \frac{1}{l_s}\,q & q &= l_s q' & d^4q &= |\,l_s\,|^4 d^4q' \\
r' &:= \frac{1}{l_s}\,r & r &= l_s r' & d^4r &= |\,l_s\,|^4 d^4r' \ .
\end{aligned}
\tag{4.41}
$$

The above definitions imply

$$
s = l_s p' \ , \ p = l_s s' \ , \ k = l_s k' \ , \ q = l_s q' \text{ and } \ r = l_s r' \, , \tag{4.42}
$$

which will have the effect of trading the p- and the s- dependence of the integrand. Carrying out completely analogous steps as in Eq. (4.65) one obtains

$$
\begin{aligned}
&\int d^3p \int_{k,q,r,s} \delta^{(4)}(p+k+q)\delta^{(4)}(k+r+s) V_3^{\mu\kappa\rho}(p,k,q) V_3^{\nu\lambda\sigma}(p,k,q) V_3^{\alpha\gamma\zeta}(k,r,s) V_3^{\beta\delta\tau}(k,r,s) \\
&\qquad \tilde{G}^R_{\kappa\alpha}(k)\tilde{G}^A_{\beta\lambda}(k)\tilde{\rho}_{\gamma\delta}(r)\tilde{F}_{\zeta\tau}(s)\left[\tilde{F}_{\rho\sigma}(q)\tilde{F}_{\nu\mu}(p) + \frac{1}{4}\,\tilde{\rho}_{\rho\sigma}(q)\tilde{\rho}_{\nu\mu}(p)\right] \\
&\qquad \text{(substitute according to (4.42))} \\
&= \int d^3p' \int_{k',q',r',s'} \delta^{(4)}(l_s(s'+k'+q'))\delta^{(4)}(l_s(k'+r'+p')) \\
&\qquad V_3^{\mu\kappa\rho}(l_s s', l_s k', l_s q') V_3^{\nu\lambda\sigma}(l_s s', l_s k', l_s q') V_3^{\alpha\gamma\zeta}(l_s k', l_s r', l_s p') V_3^{\beta\delta\tau}(l_s k', l_s r', l_s p') \tilde{G}^R_{\kappa\alpha}(l_s k')\tilde{G}^A_{\beta\lambda}(l_s k') \\
&\qquad \tilde{\rho}_{\gamma\delta}(\mathrm{sign}(l_s)|\,l_s\,|r')\tilde{F}_{\zeta\tau}(l_s p')\left[\tilde{F}_{\rho\sigma}(l_s q')\tilde{F}_{\nu\mu}(l_s s') + \frac{1}{4}\,\tilde{\rho}_{\rho\sigma}(\mathrm{sign}(l_s)|\,l_s\,|q')\tilde{\rho}_{\nu\mu}(\mathrm{sign}(l_s)|\,l_s\,|s')\right] \\
&\qquad \text{(use scaling assumptions and symmetries)} \\
&= \int d^3p' \int_{k',q',r',s'} |\,l_s\,|^{\Delta}\delta^{(4)}(s'+k'+q')\delta^{(4)}(k'+r'+p') \\
&\qquad V_3^{\mu\kappa\rho}(s',k',q') V_3^{\nu\lambda\sigma}(s',k',q') V_3^{\alpha\gamma\zeta}(k',r',p') V_3^{\beta\delta\tau}(k',r',p') \tilde{G}^R_{\kappa\alpha}(k')\tilde{G}^A_{\beta\lambda}(k') \\
&\qquad \tilde{\rho}_{\gamma\delta}(\mathrm{sign}(l_s)r')\tilde{F}_{\zeta\tau}(p')\left[\tilde{F}_{\rho\sigma}(q')\tilde{F}_{\nu\mu}(s') + \frac{|\,l_s\,|^{2\kappa}}{4}\,\tilde{\rho}_{\rho\sigma}(\mathrm{sign}(l_s)q')\tilde{\rho}_{\nu\mu}(\mathrm{sign}(l_s)s')\right] \\
&\qquad \text{(rename integration variables } q' \leftrightarrow r', \text{ use vertex symmetries Eq. (4.29))} \\
&= \int d^3p' \int_{k',q',r',s'} |\,l_s\,|^{\Delta}\delta^{(4)}(s'+k'+r')\delta^{(4)}(k'+q'+p') \\
&\qquad V_3^{\kappa\rho\mu}(k',r',s') V_3^{\lambda\sigma\nu}(k',r',s') V_3^{\zeta\alpha\gamma}(p',k',q') V_3^{\tau\beta\delta}(p',k',q') \tilde{G}^R_{\kappa\alpha}(k')\tilde{G}^A_{\beta\lambda}(k') \\
&\qquad \tilde{\rho}_{\gamma\delta}(\mathrm{sign}(l_s)q')\tilde{F}_{\zeta\tau}(p')\left[\tilde{F}_{\rho\sigma}(r')\tilde{F}_{\nu\mu}(s') + \frac{|\,l_s\,|^{2\kappa}}{4}\,\tilde{\rho}_{\rho\sigma}(\mathrm{sign}(l_s)r')\tilde{\rho}_{\nu\mu}(\mathrm{sign}(l_s)s')\right]
\end{aligned}
$$

(rename indices $\zeta \leftrightarrow \mu$, $\alpha \leftrightarrow \kappa$, $\gamma \leftrightarrow \rho$, $\tau \leftrightarrow \nu$, $\beta \leftrightarrow \lambda$, $\delta \leftrightarrow \sigma$
and use propagator symmetries) (4.43)

$$
\begin{aligned}
= \int d^3p' \int_{k',q',r',s'} & |\, l_s \,|^{\Delta} \delta^{(4)}(p'+k'+q')\delta^{(4)}(k'+r'+s') \\
& V_3^{\mu\kappa\rho}(p',k',q')V_3^{\nu\lambda\sigma}(p',k',q')V_3^{\alpha\gamma\zeta}(k',r',s')V_3^{\beta\delta\tau}(k',r',s')\tilde{G}^R_{\alpha\kappa}(k')\tilde{G}^A_{\lambda\beta}(k') \\
& \tilde{\rho}_{\rho\sigma}(\mathrm{sign}(l_s)q')\tilde{F}_{\mu\nu}(p')\left[\tilde{F}_{\gamma\delta}(r')\tilde{F}_{\tau\zeta}(s') + \frac{|\, l_s \,|^{2\kappa}}{4}\tilde{\rho}_{\gamma\delta}(\mathrm{sign}(l_s)r')\tilde{\rho}_{\tau\zeta}(\mathrm{sign}(l_s)s')\right]. \qquad (4.44)
\end{aligned}
$$

Finally, we transform (**IV**) in Eq. (4.35) by defining

$$
\begin{aligned}
q_0{}' &:= \frac{p_0^2}{q_0} & q_0 &= \frac{p_0^2}{q_0'} & dq_0 &= -\frac{p_0^2}{(q_0')^2}\, dq_0' \\
l_q &:= \frac{q_0}{p_0} = \frac{p_0'}{q_0'} & p_o' &:= p_0 & & \\
\mathbf{q}' &:= \frac{1}{l_q}\,\mathbf{p} & \mathbf{p} &= l_q\mathbf{q}' & d^3p &= |\, l_q \,|^3 d^3q' \\
\mathbf{p}' &:= \frac{1}{l_q}\,\mathbf{q} & \mathbf{q} &= l_q\mathbf{p}' & d^3q &= |\, l_q \,|^3 d^3p' \\
k' &:= \frac{1}{l_q}\,k & k &= l_q k' & d^4k &= |\, l_q \,|^4 d^4k' \\
r' &:= \frac{1}{l_q}\,r & r &= l_q r' & d^4r &= |\, l_q \,|^4 d^4r' \\
s' &:= \frac{1}{l_q}\,s & s &= l_q s' & d^4s &= |\, l_q \,|^4 d^4s' \,. \qquad (4.45)
\end{aligned}
$$

The effect of this transform will be to swap the arguments p and q in the integrand. The substitution (4.45) implies

$$
q = l_q p' \;,\; p = l_q q' \;,\; k = l_q k' \;,\; r = l_q r' \text{ and } \; s = l_q s' \,. \qquad (4.46)
$$

Recasting the integral (**IV**) from Eq. (4.35) in a similar fashion as (**II**) and (**III**) above we arrive at

$$
\begin{aligned}
\int d^3p \int_{k,q,r,s} & \delta^{(4)}(p+k+q)\delta^{(4)}(k+r+s)V_3^{\mu\kappa\rho}(p,k,q)V_3^{\nu\lambda\sigma}(p,k,q)V_3^{\alpha\gamma\zeta}(k,r,s)V_3^{\beta\delta\tau}(k,r,s) \\
& \tilde{G}^R_{\kappa\alpha}(k)\tilde{G}^A_{\beta\lambda}(k)\tilde{\rho}_{\nu\mu}(p)\tilde{F}_{\rho\sigma}(q)\left[\tilde{F}_{\gamma\delta}(r)\tilde{F}_{\zeta\tau}(s) + \frac{1}{4}\tilde{\rho}_{\gamma\delta}(r)\tilde{\rho}_{\zeta\tau}(s)\right] \\
& \text{(substitute according to (4.46))}
\end{aligned}
$$

$$
\begin{aligned}
&= \int d^3p' \int_{k',q',r',s'} \delta^{(4)}(l_q(q'+k'+p'))\delta^{(4)}(l_q(k'+r'+s')) \\
&\quad V_3^{\mu\kappa\rho}(l_q q', l_q k', l_q p') V_3^{\nu\lambda\sigma}(l_q q', l_q k', l_q p') V_3^{\alpha\gamma\zeta}(l_q k', l_q r', l_q s') V_3^{\beta\delta\tau}(l_q k', l_q r', l_q s') \tilde{G}^R_{\kappa\alpha}(l_q k') \tilde{G}^A_{\beta\lambda}(l_q k') \\
&\quad \tilde{\rho}_{\nu\mu}(\mathrm{sign}(l_q)|\, l_q\, |q') \tilde{F}_{\rho\sigma}(l_q p') \left[\tilde{F}_{\gamma\delta}(l_q r') \tilde{F}_{\zeta\tau}(l_q s') + \frac{1}{4} \tilde{\rho}_{\gamma\delta}(\mathrm{sign}(l_q)|\, l_q\, |r') \tilde{\rho}_{\zeta\tau}(\mathrm{sign}(l_q)|\, l_q\, |s') \right] \\
&\quad \text{(use scaling assumptions and symmetries)} \\
&= \int d^3p' \int_{k',q',r',s'} |\, l_q\, |^{\Delta} \delta^{(4)}(q'+k'+p') \delta^{(4)}(k'+r'+s') \\
&\quad V_3^{\mu\kappa\rho}(q', k', p') V_3^{\nu\lambda\sigma}(q', k', p') V_3^{\alpha\gamma\zeta}(k', r', s') V_3^{\beta\delta\tau}(k', r', s') \tilde{G}^R_{\kappa\alpha}(k') \tilde{G}^A_{\beta\lambda}(k') \\
&\quad \tilde{\rho}_{\nu\mu}(\mathrm{sign}(l_q) q') \tilde{F}_{\rho\sigma}(p') \left[\tilde{F}_{\gamma\delta}(r') \tilde{F}_{\zeta\tau}(s') + \frac{|\, l_q\, |^{2\kappa}}{4} \tilde{\rho}_{\gamma\delta}(\mathrm{sign}(l_q) r') \tilde{\rho}_{\zeta\tau}(\mathrm{sign}(l_q) s') \right] \\
&\quad \text{(rename indices } \rho \leftrightarrow \mu\,,\ \sigma \leftrightarrow \nu \text{ use vertex symmetries Eq. (4.29))} \\
&= \int d^3p' \int_{k',q',r',s'} |\, l_q\, |^{\Delta} \delta^{(4)}(p'+k'+q') \delta^{(4)}(k'+r'+s') \\
&\quad V_3^{\mu\kappa\rho}(p', k', q') V_3^{\nu\lambda\sigma}(p', k', q') V_3^{\alpha\gamma\zeta}(k', r', s') V_3^{\beta\delta\tau}(k', r', s') \tilde{G}^R_{\kappa\alpha}(k') \tilde{G}^A_{\beta\lambda}(k') \\
&\quad \tilde{\rho}_{\sigma\rho}(\mathrm{sign}(l_q) q') \tilde{F}_{\mu\nu}(p') \left[\tilde{F}_{\gamma\delta}(r') \tilde{F}_{\zeta\tau}(s') + \frac{|\, l_q\, |^{2\kappa}}{4} \tilde{\rho}_{\gamma\delta}(\mathrm{sign}(l_q) r') \tilde{\rho}_{\zeta\tau}(\mathrm{sign}(l_q) s') \right] . \qquad (4.47)
\end{aligned}
$$

Having recast the four integrands from Eq. (4.35), we are now ready to collect the results from Eqns. (4.40), (4.44) and (4.47). Moreover, we make use of the symmetry properties (4.11) and (4.5) and make a trivial substitution in the first integral by endowing all integration variables appearing in its integrand with a prime. We also define $p'_0 \equiv p_o$, keeping in mind that we have assumed $p_0 > 0$. Then the contribution to the $O(g^4)$ fixed-point condition visualised in Fig. 4.7 takes the form

$$
\begin{aligned}
0 = &\int d^3p' \int_{k',q',r',s'} \delta^{(4)}(p'+k'+q')\, \delta^{(4)}(k'+r'+s') \\
&\quad V_3^{\mu\kappa\rho}(p', k', q') V_3^{\nu\lambda\sigma}(p', k', q') V_3^{\alpha\gamma\zeta}(k', r', s') V_3^{\beta\delta\tau}(k', r', s') \Big\{ \\
&- \frac{p'_0}{p'_0} \tilde{G}^R_{\kappa\alpha}(k') \tilde{G}^A_{\beta\lambda}(k') \tilde{\rho}_{\rho\sigma}(q') \tilde{F}_{\nu\mu}(p') \left[\tilde{F}_{\gamma\delta}(r') \tilde{F}_{\zeta\tau}(s') + \frac{1}{4} \tilde{\rho}_{\gamma\delta}(r') \tilde{\rho}_{\zeta\tau}(s') \right] \\
&+ |\, l_r\, |^{\Delta} \tilde{G}^R_{\alpha\kappa}(k') \tilde{G}^A_{\lambda\beta}(k') \tilde{\rho}_{\rho\sigma}(\mathrm{sign}(l_r) q') \tilde{F}_{\mu\nu}(p') \left[\tilde{F}_{\delta\gamma}(r') \tilde{F}_{\zeta\tau}(s') + \frac{|\, l_r\, |^{2\kappa}}{4} \tilde{\rho}_{\delta\gamma}(\mathrm{sign}(l_r) r') \tilde{\rho}_{\zeta\tau}(\mathrm{sign}(l_r) s') \right] \\
&+ |\, l_s\, |^{\Delta} \tilde{G}^R_{\alpha\kappa}(k') \tilde{G}^A_{\lambda\beta}(k') \tilde{\rho}_{\rho\sigma}(\mathrm{sign}(l_s) q') \tilde{F}_{\mu\nu}(p') \left[\tilde{F}_{\gamma\delta}(r') \tilde{F}_{\tau\zeta}(s') + \frac{|\, l_s\, |^{2\kappa}}{4} \tilde{\rho}_{\gamma\delta}(\mathrm{sign}(l_s) r') \tilde{\rho}_{\tau\zeta}(\mathrm{sign}(l_s) s') \right] \\
&- |\, l_q\, |^{\Delta} \tilde{G}^R_{\kappa\alpha}(k') \tilde{G}^A_{\beta\lambda}(k') \tilde{\rho}_{\sigma\rho}(\mathrm{sign}(l_q) q') \tilde{F}_{\mu\nu}(p') \left[\tilde{F}_{\gamma\delta}(r') \tilde{F}_{\zeta\tau}(s') + \frac{|\, l_q\, |^{2\kappa}}{4} \tilde{\rho}_{\gamma\delta}(\mathrm{sign}(l_q) r') \tilde{\rho}_{\zeta\tau}(\mathrm{sign}(l_q) s') \right] \Big\} \\
&= \int d^3p' \int_{k',q',r',s'} \delta^{(4)}(p'+k'+q') \delta^{(4)}(k'+r'+s') V_3^{\mu\kappa\rho}(p', k', q') V_3^{\nu\lambda\sigma}(p', k', q') \\
&\quad V_3^{\alpha\gamma\zeta}(k', r', s') V_3^{\beta\delta\tau}(k', r', s') \tilde{G}^R_{\alpha\kappa}(k') \tilde{G}^A_{\lambda\beta}(k') \tilde{\rho}_{\rho\sigma}(q') \tilde{F}_{\nu\mu}(p') \tilde{F}_{\gamma\delta}(r') \tilde{F}_{\zeta\tau}(s') \Big\{
\end{aligned}
$$

$$
\begin{aligned}
&- \operatorname{sign}(p_0')\left|\frac{p_0'}{p_0'}\right|^{\Delta} + \operatorname{sign}(r_0')\left|\frac{p_0'}{r_0'}\right|^{\Delta} + \operatorname{sign}(s_0')\left|\frac{p_0'}{s_0'}\right|^{\Delta} - \operatorname{sign}(q_0')\left|\frac{p_0'}{q_0'}\right|^{\Delta}\Big\} \\
&+ \frac{1}{4}\int d^3p' \int_{k',q',r',s'} \delta^{(4)}(p'+k'+q')\delta^{(4)}(k'+r'+s')V_3^{\mu\kappa\rho}(p',k',q')V_3^{\nu\lambda\sigma}(p',k',q') \\
&V_3^{\alpha\gamma\zeta}(k',r',s')V_3^{\beta\delta\tau}(k',r',s')\tilde{G}^R_{\alpha\kappa}(k')\tilde{G}^A_{\lambda\beta}(k')\tilde{\rho}_{\rho\sigma}(q')\tilde{F}_{\nu\mu}(p')\tilde{\rho}_{\gamma\delta}(r')\tilde{\rho}_{\zeta\tau}(s')\Big\{ \\
&- \operatorname{sign}(p_0')\left|\frac{p_0'}{p_0'}\right|^{\Delta+2\kappa} + \operatorname{sign}(r_0')\left|\frac{p_0'}{r_0'}\right|^{\Delta+2\kappa} + \operatorname{sign}(s_0')\left|\frac{p_0'}{s_0'}\right|^{\Delta+2\kappa} - \operatorname{sign}(q_0')\left|\frac{p_0'}{q_0'}\right|^{\Delta+2\kappa}\Big\} \\
&\text{(classical limit Eq. (2.29))} \\
\approx &\int d^3p' \int_{k',q',r',s'} \delta^{(4)}(p'+k'+q')\delta^{(4)}(k'+r'+s')V_3^{\mu\kappa\rho}(p',k',q')V_3^{\nu\lambda\sigma}(p',k',q') \\
&V_3^{\alpha\gamma\zeta}(k',r',s')V_3^{\beta\delta\tau}(k',r',s')\tilde{G}^R_{\alpha\kappa}(k')\tilde{G}^A_{\lambda\beta}(k')\tilde{\rho}_{\rho\sigma}(q')\tilde{F}_{\nu\mu}(p')\tilde{F}_{\gamma\delta}(r')\tilde{F}_{\zeta\tau}(s')\left| p_0\right|^{\Delta}\Big\{ \\
&- \operatorname{sign}(p_0')\left|p_0'\right|^{-\Delta} + \operatorname{sign}(r_0')\left|r_0'\right|^{-\Delta} + \operatorname{sign}(s_0')\left|s_0'\right|^{-\Delta} - \operatorname{sign}(q_0')\left|q_0'\right|^{-\Delta}\Big\}\,. \qquad (4.48)
\end{aligned}
$$

From the last line we can deduce that there are two solutions for κ in the classical limit that cause the integral to vanish. First, there is a solution in the case that

$$\Delta = -3\kappa + 4 = -1 \qquad \Rightarrow \qquad \kappa = \frac{5}{3}\,. \qquad (4.49)$$

To see this, note that for $\Delta = -1$

$$
\begin{aligned}
&- \operatorname{sign}(p_0')\left|p_0'\right|^{-\Delta} + \operatorname{sign}(r_0')\left|r_0'\right|^{-\Delta} + \operatorname{sign}(s_0')\left|s_0'\right|^{-\Delta} - \operatorname{sign}(q_0')\left|q_0'\right|^{-\Delta} \\
&= -\operatorname{sign}(p_0')\left|p_0'\right| + \operatorname{sign}(r_0')\left|r_0'\right| + \operatorname{sign}(s_0')\left|s_0'\right| - \operatorname{sign}(q_0')\left|q_0'\right| \\
&= -p_0' + r_0' + s_0' - q_0'\,,
\end{aligned}
$$

which is zero in Eq. (4.48) because the δ- functions ensure

$$p' + q' - r' - s' = 0\,.$$

(Note that only the 0- component of this identity is required to find the solution (4.49).)

Another solution is found in the on-shell limit with only $2 \leftrightarrow 2$ scattering contributing. If we take without loss of generality p' and q' as the four momenta of the incoming particles and r' and s' as the outgoing particles, then $p_0', q_0', r_0', s_0' > 0$. From Eq. (4.48) one then finds a zero for

$$\Delta = -3\kappa + 4 = 0 \qquad \Rightarrow \qquad \kappa = \frac{4}{3}\,. \qquad (4.50)$$

In this case the integrand in the last line of Eq. (4.48) is identically zero because

$$- \operatorname{sign}(p_0')\left|p_0'\right|^{-\Delta} + \operatorname{sign}(r_0')\left|r_0'\right|^{-\Delta} + \operatorname{sign}(s_0')\left|s_0'\right|^{-\Delta} - \operatorname{sign}(q_0')\left|q_0'\right|^{-\Delta}$$

$$= -\text{sign}(p_0') + \text{sign}(r_0') + \text{sign}(s_0') - \text{sign}(q_0')$$
$$= -1 + 1 + 1 - 1 = 0 \,.$$

Note that it is crucial in this case to make the additional assumption of being in the on-shell limit with contributions exclusively from $2 \leftrightarrow 2$ scattering.

It can be inferred from the last but one equality in Eq. (4.48) that there are no power-law solutions in the full quantum theory, where the classicality condition (2.29) does not hold. By the same reasoning as before, one sees that the quantum terms themselves would vanish provided that either $-\kappa + 4 = -1$ or $-\kappa + 4 = 0$, resulting in $\kappa = 5$ or $\kappa = 4$. However, there is no solution for κ that causes both the classical and the quantum contribution to vanish simultaneously. Therefore, we conclude that the quantum terms destroy the power-law solutions in Eqns. (4.49) and (4.50). These solutions can only be present in situations in which the classical approximation is applicable.

The analysis of the fixed point is not yet complete. So far it has only been shown that the contributions to the fixed-point equation (4.33) arising from the one-loop diagram Fig. 4.5 at order g^4 vanish in the classical limit. The scaling solutions found above with the occupation number exponent κ given by (4.49) or (4.50) could be spoilt if they were not zeroes of the setting- sun and the squint contribution to Eq. (4.33) as well. That they indeed cause those terms to vanish will be demonstrated in the following for the setting-sun diagram. The squint depicted in Fig. 4.8(b) can be dealt with along very similar lines, which has been checked in the computations for [43].

The analysis of the setting-sun diagram depicted in Fig. 4.8(a) requires the four-gluon vertex for SU(2) Yang-Mills theory defined in Eq. (3.25). In contrast to the above evaluation of the one-loop diagram it is not possible here to factor out the colour structure at the very beginning. However, we note that in the setting-sun contribution to the identity (4.22) two four-gluon vertices will be contracted with four Kronecker- deltas. It is convenient to contract the colour structure beforehand, thereby summarising the Lorentz structure in a tensor $W^{\mu\alpha\beta\gamma\nu\lambda\kappa\sigma}$:

$$\begin{aligned} V^{\mu\alpha\beta\gamma}_{4\ mabc} V^{\nu\kappa\lambda\sigma}_{4\ nkls}\, \delta_{mn}\delta_{ak}\delta_{bl}\delta_{cs} &= V^{\mu\alpha\beta\gamma}_{4\ mabc} V^{\nu\kappa\lambda\sigma}_{4\ mabc} \\ &= -18g^4\Big\{-g^{\alpha\beta}g^{\gamma\mu}\Big(g^{\kappa\sigma}g^{\lambda\nu} + g^{\kappa\nu}g^{\lambda\sigma} - 2g^{\kappa\lambda}g^{\nu\sigma}\Big) + g^{\alpha\mu}g^{\beta\gamma}\Big(2g^{\kappa\sigma}g^{\lambda\nu} - g^{\kappa\nu}g^{\lambda\sigma} - g^{\kappa\lambda}g^{\nu\sigma}\Big) \\ &\qquad - g^{\alpha\gamma}g^{\beta\mu}\Big(g^{\kappa\sigma}g^{\lambda\nu} - 2g^{\kappa\nu}g^{\lambda\sigma} + g^{\kappa\lambda}g^{\nu\sigma}\Big)\Big\} \\ &\equiv g^4 W^{\mu\alpha\beta\gamma\nu\lambda\kappa\sigma} \,. \end{aligned} \tag{4.51}$$

We note the following symmetries of the tensor $W^{\mu\alpha\beta\gamma\nu\lambda\kappa\sigma}$ which can easily be verified *e.g.* by

means of a computer algebra package:

$$W^{\mu\alpha\beta\gamma\nu\kappa\lambda\sigma} = W^{\nu\kappa\lambda\sigma\mu\alpha\beta\gamma} = W^{\alpha\beta\gamma\mu\kappa\lambda\sigma\nu} = W^{\mu\beta\alpha\gamma\nu\lambda\kappa\sigma} = W^{\alpha\mu\beta\gamma\lambda\nu\kappa\sigma} \,. \tag{4.52}$$

Decomposing the Wigner-transformed setting-sun contribution to the non-local self-energy into its symmetric and anti-symmetric part yields

$$\begin{aligned}
\tilde{S}^{\mu\nu}_{(F)\,mn}(p) = \int_{k,q,r} (2\pi)^4\, \delta^{(4)}(p-k-q-r) V_{4\;mabc}^{\mu\alpha\beta\gamma} V_{4\;nkls}^{\nu\kappa\lambda\sigma}\, \delta_{ak}\delta_{bl}\delta_{cs} \Big\{ & \tilde{F}_{\alpha\kappa}(k)\tilde{F}_{\beta\lambda}(q)\tilde{F}_{\gamma\sigma}(r) \\
& + \frac{1}{4}\Big(\tilde{F}_{\alpha\kappa}(k)\tilde{\rho}_{\beta\lambda}(q)\tilde{\rho}_{\gamma\sigma}(r) + \tilde{\rho}_{\alpha\kappa}(r)\tilde{F}_{\beta\lambda}(q)\tilde{\rho}_{\gamma\sigma}(r) + \tilde{\rho}_{\alpha\kappa}(k)\tilde{\rho}_{\beta\lambda}(q)\tilde{F}_{\gamma\delta}(r)\Big)\Big\} \\
\tilde{S}^{\mu\nu}_{(\rho)\,mn}(p) = \int_{k,q,r} (2\pi)^4\, \delta^{(4)}(p-k-q-r) V_{4\;mabc}^{\mu\alpha\beta\gamma} V_{4\;nkls}^{\nu\kappa\lambda\sigma}\, \delta_{ak}\delta_{bl}\delta_{cs} \Big\{ & \tilde{\rho}_{\alpha\kappa}(k)\tilde{F}_{\beta\lambda}(q)\tilde{F}_{\gamma\sigma}(r) \\
& + \tilde{\rho}_{\beta\lambda}(q)\tilde{F}_{\alpha\kappa}(k)\tilde{F}_{\gamma\sigma}(r) + \tilde{\rho}_{\gamma\sigma}(r)\tilde{F}_{\alpha\kappa}(k)\tilde{F}_{\beta\lambda}(q) - \frac{1}{4}\tilde{\rho}_{\alpha\kappa}(k)\tilde{\rho}_{\beta\lambda}(q)\tilde{\rho}_{\gamma\sigma}(r)\Big\} \,.
\end{aligned} \tag{4.53}$$

The corresponding contribution to the identity (4.24), whose zeroes we are interested in, reads

$$\int d^3p \left\{ \tilde{S}^{\mu\nu}_{(\rho)\,mn}(p)\tilde{F}^{nm}_{\nu\mu}(p) - \tilde{S}^{\mu\nu}_{(F)\,mn}(p)\tilde{\rho}^{nm}_{\nu\mu}(p) \right\} \stackrel{!}{=} 0 \,. \tag{4.54}$$

Upon contraction of the colour structure according to Eq. (4.51) this takes the form

$$\begin{aligned}
0 = \int d^3p \int_{k,q,r} \delta^{(4)}(p-k-q-r) W^{\mu\alpha\beta\gamma\nu\kappa\lambda\sigma} \Big\{ & \\
\tilde{F}_{\nu\mu}(p) \Big[& \tilde{\rho}_{\alpha\kappa}(k)\tilde{F}_{\beta\lambda}(q)\tilde{F}_{\gamma\sigma}(r) + \tilde{\rho}_{\beta\lambda}(q)\tilde{F}_{\alpha\kappa}(k)\tilde{F}_{\gamma\sigma}(r) + \tilde{\rho}_{\gamma\sigma}(r)\tilde{F}_{\alpha\kappa}(k)\tilde{F}_{\beta\lambda}(q) \\
& + \frac{1}{4}\tilde{\rho}_{\alpha\kappa}(k)\tilde{\rho}_{\beta\lambda}(q)\tilde{\rho}_{\gamma\sigma}(r) \Big] \\
-\tilde{\rho}_{\nu\mu}(p) \Big[& \tilde{F}_{\alpha\kappa}(k)\tilde{F}_{\beta\lambda}(q)\tilde{F}_{\gamma\sigma}(r) \\
& + \frac{1}{4}\Big(\tilde{F}_{\alpha\kappa}(k)\tilde{\rho}_{\beta\lambda}(q)\tilde{\rho}_{\gamma\sigma}(r) + \tilde{\rho}_{\alpha\kappa}(k)\tilde{F}_{\beta\lambda}(q)\tilde{\rho}_{\gamma\sigma}(r) + \tilde{\rho}_{\alpha\kappa}(k)\tilde{\rho}_{\beta\lambda}(q)\tilde{F}_{\gamma\sigma}(r)\Big) \Big] \Big\} \,.
\end{aligned} \tag{4.55}$$

Our objective is to verify that scaling solutions of the form (4.12) with κ given by either of Eqns. (4.49) or (4.50) cause the right hand side of Eq. (4.55) to vanish in the classical-statistical limit. Hence we can already make use of the classicality condition (2.29) at this point and discard the quantum terms, which can easily be identified in Eq. (4.55) as the terms featuring three factors of $\tilde{\rho}$ and one factor of $\tilde{F}$. Doing so, we obtain from Eq. (4.55)

$$0 = \int d^3p \int_{k,q,r} \delta^{(4)}(p-k-q-r) W^{\mu\alpha\beta\gamma\nu\kappa\lambda\sigma} \Big\{$$

$$\underbrace{\tilde{F}_{\nu\mu}(p)\tilde{\rho}_{\alpha\kappa}(k)\tilde{F}_{\beta\lambda}(q)\tilde{F}_{\gamma\sigma}(r)}_{S_I} + \underbrace{\tilde{F}_{\nu\mu}(p)\tilde{\rho}_{\beta\lambda}(q)\tilde{F}_{\alpha\kappa}(k)\tilde{F}_{\gamma\sigma}(r)}_{S_{II}}$$
$$+\underbrace{\tilde{F}_{\nu\mu}(p)\tilde{\rho}_{\gamma\sigma}(r)\tilde{F}_{\alpha\kappa}(k)\tilde{F}_{\beta\lambda}(q)}_{S_{III}} - \underbrace{\tilde{\rho}_{\nu\mu}(p)\tilde{F}_{\alpha\kappa}(k)\tilde{F}_{\beta\lambda}(q)\tilde{F}_{\gamma\sigma}(r)}_{S_{IV}}\Big\} . \tag{4.56}$$

We make the same scaling and symmetry assumptions on the propagators as in the case of the one-loop diagram depicted in Fig. 4.5 and carry out analogous scaling transformations in order to solve for κ. We start by transforming S_I to the form of S_{IV} by substituting

$$\begin{aligned}
k_0{}' &:= \frac{p_0^2}{k_0} & k_0 &= \frac{p_0^2}{k_0'} & dk_0 &= -\frac{p_0^2}{(k_0')^2}\, dk_0' \\
l_k &:= \frac{k_0}{p_0} = \frac{p_0'}{k_0'} & p_o' &:= p_0 & & \\
\mathbf{k}' &:= \frac{1}{l_k}\,\mathbf{p} & \mathbf{p} &= l_k \mathbf{k}' & d^3p &= |\, l_k\,|^3 d^3k' \\
\mathbf{p}' &:= \frac{1}{l_k}\,\mathbf{k} & \mathbf{k} &= l_k \mathbf{p}' & d^3k &= |\, l_k\,|^3 d^3p' \\
q' &:= \frac{1}{l_k}\, q & q &= l_k q' & d^4q &= |\, l_k\,|^4 d^4q' \\
r' &:= \frac{1}{l_k}\, r & r &= l_k r' & d^4r &= |\, l_k\,|^4 d^4r' \ .
\end{aligned} \tag{4.57}$$

This implies

$$k = l_k p' \ , \ p = l_k q' \ , \ q = l_k q' \text{ and } \ r = l_q r' \ . \tag{4.58}$$

With these substitutions we recast the contribution S_I:

$$\begin{aligned}
&\int d^3p \int_{k,q,r} \delta^{(4)}(p-k-q-r) W^{\mu\alpha\beta\gamma\nu\kappa\lambda\sigma}\, \tilde{F}_{\nu\mu}(p)\tilde{\rho}_{\alpha\kappa}(k)\tilde{F}_{\beta\lambda}(q)\tilde{F}_{\gamma\sigma}(r) \\
&= \int d^3p' \int_{k',q',r'} |\, l_k\,|^{\Delta} \delta^{(4)}(k'-p'-q'-r') W^{\mu\alpha\beta\gamma\nu\kappa\lambda\sigma}\, \tilde{F}_{\nu\mu}(k')\tilde{\rho}_{\alpha\kappa}(\mathrm{sign}(l_k)p')\tilde{F}_{\beta\lambda}(q')\tilde{F}_{\gamma\sigma}(r') \\
&\qquad \text{(Substitute } q' \mapsto (-q') \ , \ r' \mapsto (-r') \text{)} \\
&= \int d^3p' \int_{k',q',r'} |\, l_k\,|^{\Delta} \delta^{(4)}(k'-p'+q'+r') W^{\mu\alpha\beta\gamma\nu\kappa\lambda\sigma}\, \tilde{F}_{\nu\mu}(k')\tilde{\rho}_{\alpha\kappa}(\mathrm{sign}(l_k)p')\tilde{F}_{\beta\lambda}(q')\tilde{F}_{\gamma\sigma}(r') \\
&\qquad \text{(Use symmetries (4.52))} \\
&= \int d^3p' \int_{k',q',r'} |\, l_k\,|^{\Delta} \delta^{(4)}(k'-p'+q'+r') W^{\alpha\mu\beta\gamma\kappa\nu\lambda\sigma}\, \tilde{F}_{\nu\mu}(k')\tilde{\rho}_{\alpha\kappa}(\mathrm{sign}(l_k)p')\tilde{F}_{\beta\lambda}(q')\tilde{F}_{\gamma\sigma}(r') \\
&\qquad \text{(Rename summation indices } \mu \leftrightarrow \alpha \ , \ \nu \leftrightarrow \kappa \text{)} \\
&= \int d^3p' \int_{k',q',r'} |\, l_k\,|^{\Delta} \delta^{(4)}(p'-k'-q'-r') W^{\mu\alpha\beta\gamma\nu\kappa\lambda\sigma}\, \tilde{\rho}_{\mu\nu}(\mathrm{sign}(l_k)p')\tilde{F}_{\kappa\alpha}(k')\tilde{F}_{\beta\lambda}(q')\tilde{F}_{\gamma\sigma}(r') \ .
\end{aligned} \tag{4.59}$$

We transform the contributions of S_{II} by changing the variables according to

$$
\begin{aligned}
q_0{}' &:= \frac{p_0^2}{q_0} & q_0 &= \frac{p_0^2}{q_0'} & dq_0 &= -\frac{p_0^2}{(q_0')^2}\, dq_0' \\
l_q &:= \frac{q_0}{p_0} = \frac{p_0'}{q_0'} & p_o' &:= p_0 & & \\
\mathbf{q}' &:= \frac{1}{l_q}\,\mathbf{p} & \mathbf{p} &= l_q \mathbf{q}' & d^3p &= |\, l_q\,|^3 d^3q' \\
\mathbf{p}' &:= \frac{1}{l_q}\,\mathbf{q} & \mathbf{q} &= l_q \mathbf{p}' & d^3q &= |\, l_q\,|^3 d^3p' \\
k' &:= \frac{1}{l_q}\, k & k &= l_q k' & d^4k &= |\, l_q\,|^4 d^4k' \\
r' &:= \frac{1}{l_q}\, r & r &= l_q r' & d^4r &= |\, l_q\,|^4 d^4r' \ .
\end{aligned}
\tag{4.60}
$$

That is,

$$
q = l_q p' \ , \ p = l_q q' \ , \ k = l_q k' \text{ and } \ r = l_q r' \ . \tag{4.61}
$$

With these definitions the S_{II} integral can be cast into the form

$$
\begin{aligned}
&\int d^3p \int_{k,q,r} \delta^{(4)}(p-k-q-r) W^{\mu\alpha\beta\gamma\nu\kappa\lambda\sigma}\, \tilde{F}_{\nu\mu}(p)\tilde{\rho}_{\beta\lambda}(q)\tilde{F}_{\alpha\kappa}(k)\tilde{F}_{\gamma\sigma}(r) \\
&= \int d^3p' \int_{k',q',r'} |\, l_q\,|^{\Delta} \delta^{(4)}(q'-k'-p'-r') W^{\mu\alpha\beta\gamma\nu\kappa\lambda\sigma}\, \tilde{F}_{\nu\mu}(q')\tilde{\rho}_{\beta\lambda}(\mathrm{sign}(l_q)p')\tilde{F}_{\alpha\kappa}(k')\tilde{F}_{\gamma\sigma}(r') \\
&\qquad \text{(Substitute } k' \mapsto (-k') \ , \ r' \mapsto (-r') \ ) \\
&= \int d^3p' \int_{k',q',r'} |\, l_q\,|^{\Delta} \delta^{(4)}(q'+k'-p'+r') W^{\mu\alpha\beta\gamma\nu\kappa\lambda\sigma}\, \tilde{F}_{\nu\mu}(q')\tilde{\rho}_{\beta\lambda}(\mathrm{sign}(l_q)p')\tilde{F}_{\alpha\kappa}(k')\tilde{F}_{\gamma\sigma}(r') \\
&\qquad \text{(Use symmetries (4.52))} \\
&= \int d^3p' \int_{k',q',r'} |\, l_q\,|^{\Delta} \delta^{(4)}(q'+k'-p'+r') W^{\beta\alpha\mu\gamma\lambda\kappa\nu\sigma}\, \tilde{F}_{\nu\mu}(q')\tilde{\rho}_{\beta\lambda}(\mathrm{sign}(l_q)p')\tilde{F}_{\alpha\kappa}(k')\tilde{F}_{\gamma\sigma}(r') \\
&\qquad \text{(Rename summation indices } \mu \leftrightarrow \beta \ , \ \nu \leftrightarrow \lambda \ ) \\
&= \int d^3p' \int_{k',q',r'} |\, l_q\,|^{\Delta} \delta^{(4)}(p'kk'-q'-r') W^{\mu\alpha\beta\gamma\nu\kappa\lambda\sigma}\, \tilde{\rho}_{\mu\nu}(\mathrm{sign}(l_q)p')\tilde{F}_{\lambda\beta}(q')\tilde{F}_{\alpha\kappa}(k')\tilde{F}_{\gamma\sigma}(r') \ .
\end{aligned}
\tag{4.62}
$$

Finally, the scaling transformation applied to S_{III} is given by

$$
\begin{aligned}
r_0{}' &:= \frac{p_0^2}{r_0} & r_0 &= \frac{p_0^2}{r_0'} & dr_0 &= -\frac{p_0^2}{(r_0')^2}\, dr_0' \\
l_r &:= \frac{r_0}{p_0} = \frac{p_0'}{r_0'} & p_o' &:= p_0 & &
\end{aligned}
$$

$$\begin{aligned}
\mathbf{r}' &:= \frac{1}{l_r}\,\mathbf{p} & \mathbf{p} &= l_r\mathbf{r}' & d^3p &= |\,l_r\,|^3 d^3r' \\
\mathbf{p}' &:= \frac{1}{l_r}\,\mathbf{r} & \mathbf{r} &= l_r\mathbf{p}' & d^3r &= |\,l_r\,|^3 d^3p' \\
k' &:= \frac{1}{l_r}\,k & k &= l_r k' & d^4k &= |\,l_r\,|^4 d^4k' \\
q' &:= \frac{1}{l_r}\,q & q &= l_r q' & d^4q &= |\,l_r\,|^4 d^4q' \;. \qquad (4.63)
\end{aligned}$$

Note that with these definitions

$$r = l_r p' \;,\; p = l_r r' \;,\; k = l_r k' \text{ and } \; q = l_r q' \;. \qquad (4.64)$$

Manipulating the S_{III} in a similar fashion as the other integrals yields

$$\begin{aligned}
&\int d^3p \int_{k,q,r} \delta^{(4)}(p-k-q-r) W^{\mu\alpha\beta\gamma\nu\kappa\lambda\sigma}\, \tilde{F}_{\nu\mu}(p)\tilde{\rho}_{\gamma\sigma}(r)\tilde{F}_{\alpha\kappa}(k)\tilde{F}_{\beta\lambda}(q) \\
&= \int d^3p' \int_{k',q',r'} |\,l_r\,|^{\Delta}\delta^{(4)}(r'-k'-q'-p') W^{\mu\alpha\beta\gamma\nu\kappa\lambda\sigma}\, \tilde{F}_{\nu\mu}(q')\tilde{\rho}_{\gamma\sigma}(\mathrm{sign}(l_r)p')\tilde{F}_{\alpha\kappa}(k')\tilde{F}_{\beta\lambda}(q') \\
&\qquad \text{(Substitute } k' \mapsto (-k') \;,\; q' \mapsto (-q') \text{)} \\
&= \int d^3p' \int_{k',q',r'} |\,l_r\,|^{\Delta}\delta^{(4)}(r'+k'+q'-p') W^{\mu\alpha\beta\gamma\nu\kappa\lambda\sigma}\, \tilde{F}_{\nu\mu}(q')\tilde{\rho}_{\gamma\sigma}(\mathrm{sign}(l_r)p')\tilde{F}_{\alpha\kappa}(k')\tilde{F}_{\beta\lambda}(q') \\
&\qquad \text{(Rename summation indices } \mu \leftrightarrow \gamma \;,\; \nu \leftrightarrow \sigma \text{)} \\
&= \int d^3p' \int_{k',q',r'} |\,l_r\,|^{\Delta}\delta^{(4)}(r'+k'+q'-p') W^{\gamma\alpha\beta\mu\sigma\kappa\lambda\nu}\, \tilde{F}_{\sigma\gamma}(q')\tilde{\rho}_{\mu\nu}(\mathrm{sign}(l_r)p')\tilde{F}_{\alpha\kappa}(k')\tilde{F}_{\beta\lambda}(q') \\
&\qquad \text{(Use symmetries (4.52))} \\
&= \int d^3p' \int_{k',q',r'} |\,l_r\,|^{\Delta}\delta^{(4)}(p'-k'-q'-r') W^{\mu\alpha\beta\gamma\nu\kappa\lambda\sigma}\, \tilde{\rho}_{\mu\nu}(\mathrm{sign}(l_r)p')\tilde{F}_{\sigma\gamma}(q')\tilde{F}_{\alpha\kappa}(k')\tilde{F}_{\beta\lambda}(q') \;. \qquad (4.65)
\end{aligned}$$

Eventually, we can gather all contributions from Eqns. (4.56), (4.59), (4.62) and (4.65) to obtain

$$\begin{aligned}
0 &= g^4 \int\int d^3p' \int_{k',q',r'} \delta^{(4)}(p'-k'-q'-r') W^{\mu\alpha\beta\gamma\nu\kappa\lambda\sigma} \tilde{\rho}_{\nu\mu}(p')\tilde{F}_{\alpha\kappa}(k')\tilde{F}_{\beta\lambda}(q')\tilde{F}_{\gamma\sigma}(r') \\
&\qquad \Big\{ -1 + |l_k|^{\Delta}\mathrm{sign}(l_k) + |l_q|^{\Delta}\mathrm{sign}(l_q) + |l_r|^{\Delta}\mathrm{sign}(l_r) \Big\} \\
&= -g^4 \int\int d^3p' \int_{k',q',r'} \delta^{(4)}(p'-k'-q'-r') W^{\mu\alpha\beta\gamma\nu\kappa\lambda\sigma} \tilde{\rho}_{\nu\mu}(p')\tilde{F}_{\alpha\kappa}(k')\tilde{F}_{\beta\lambda}(q')\tilde{F}_{\gamma\sigma}(r') \\
&\qquad \Big\{ \frac{p_0}{p_0} - \Big|\frac{p_0}{k_0}\Big|^{\Delta}\mathrm{sign}\Big(\frac{p_0}{k_0}\Big) - \Big|\frac{p_0}{q_0}\Big|^{\Delta}\mathrm{sign}\Big(\frac{p_0}{q_0}\Big) - \Big|\frac{p_0}{r_0}\Big|^{\Delta}\mathrm{sign}\Big(\frac{p_0}{r_0}\Big) \Big\}
\end{aligned}$$

$$= -g^4 \int\int d^3p' \int_{k',q',r'} \delta^{(4)}(p'-k'-q'-r') W^{\mu\alpha\beta\gamma\nu\kappa\lambda\sigma} \tilde{\rho}_{\nu\mu}(p') \tilde{F}_{\alpha\kappa}(k') \tilde{F}_{\beta\lambda}(q') \tilde{F}_{\gamma\sigma}(r')$$
$$|p_0|^\Delta \left\{ |p_0|^{-\Delta} - |k_0|^{-\Delta} \mathrm{sign}(k_0) - |\, q_0\,|^{-\Delta} \mathrm{sign}(q_0) - |\, r_0\,|^{-\Delta} \mathrm{sign}(r_0) \right\} . \qquad (4.66)$$

As in Eq. (4.48), we have carried out a trivial substitution in the S_{IV}- term by endowing all of its integration variables with a prime and defining $p'_0 \equiv p_0$. Again, we find zeroes for the same values of κ as before, *i.e.* the values quoted in Eqns. (4.49) and (4.50).

In the above analysis we have demonstrated that the scaling solutions (4.49) and (4.50) also cause the setting-sun contribution in Eq. (4.33) to vanish in the classical-statistical limit. It remains to show that the same holds for the squint contribution. This has been verified in the preparations for [43]. Due to its length and its analogy to the other g^4- computations we refrain from giving the details of this computation here, however.

We close this Section by making some further comments on our results. First, we note that our analytical results (Eqns. (4.49) and (4.50)) for SU(2) Yang-Mills theory are equal to the values for κ that have been found for scalar theories using the formalism of Boltzmann equations in the context of early universe cosmology in [113][15]. More precisely, our results can be reproduced from the predictions of these authors under the assumption that the momenta are large compared to the rest mass of the particles under consideration, which causes the matrix element appearing in the Boltzmann equation and the dispersion relation to exhibit a certain scaling behaviour. In the framework of [113] the exponent (4.49) is found in situations characterised by constant energy flow in momentum space while (4.50) is reproduced for constant flow of particle number. These two cases are referred to in [113] as the "energy cascade" and the "particle cascade", respectively. Employing a different approach to scalar fields identical results for κ were obtained in [39, 41]. Given that our perturbative approach to non-Abelian gauge fields is valid at high momenta one can conclude that both kinds of field theories (*i.e.* scalars and non-Abelian gauge fields) exhibit identical scaling behaviour in the turbulent regime. This is an intriguing finding. *A priori*, scalar and gauge field theories are very different. Thus our result confirms the notion of universality far from thermal equilibrium [39].

Comparing the analytic predictions for κ from Eqns. (4.49) and (4.50) with the numerical result quoted in Eq. (4.21) one finds that the latter is in excellent agreement with the value derived for the "particle cascade". This confirms that the 2PI formalism can successfully be applied to gauge theories. One can also conclude that the classical-statistical lattice simulations represent on-shell physics that is dominated by $2 \leftrightarrow 2$ scattering. It is tempting to speculate if there might be initial conditions which trigger an "energy cascade", *i.e.* exhibiting power-law spectra with

[15] The authors of [113] denote the occupation number exponent by α rather than κ, however.

$\kappa = 5/3$. This remains to be investigated in future work. Furthermore, we stress that the assumption of isotropy entering via Eq. (4.5) can be justified by the numerical data. At late times the equal-time correlation function is indeed isotropic as can be inferred from Fig. 4.2.

Finally, some remarks are due regarding the gauge dependence of our results. In our analytical calculation we have not specified a gauge at any point. However, by neglecting the ghosts our approach implicitly favours gauges that are either free of ghosts, *e.g.* axial gauges, or gauges in which ghosts play a subordinate *rôle*. The latter applies to a certain extent to Coulomb gauge which we have chosen in our numerical study in Section 4.1. The spatial components of the gauge field are strictly transversal in Coulomb gauge, which allows to relate the gauge field's modulus to particle number in a perturbative setting [18]. At this point we can only speculate why power-law spectra do not seem to occur in temporal axial gauge even although the spectra display quasi-stationary at late times as well. On the other hand, the logic of our approach is to assume scaling behaviour of the kind (4.12) and subsequently to search possible solutions for κ. It does not predict that scaling should be observed in an arbitrary gauge, however. In this context it is interesting to note that temporal axial gauge spectra do not show scaling behaviour in (classical) thermal equilibrium either, while they do in Coulomb gauge. This is demonstrated in Appendix D.

4.3 A glance at the IR

Investigating the behaviour of gauge field propagators at low momentum is interesting for mainly two reasons. First, it is the infrared part of the spectrum on non-Abelian gauge theories that keeps posing tough challenges and which is therefore interesting by itself. In particular, the mechanism of confinement, which constitutes an IR phenomenon, is still puzzling. Second, recent works [39–41] have found out-of-equilibrium critical phenomena in scalar field theories. These are characterised by scaling solutions for the propagators in the infrared that are similar to Eq. (4.12). However, there are two major differences. On the one hand side, the IR spectra encountered in the scalar case feature far higher exponents $\kappa = 4 - 5$. Moreover, the physics in this regime is qualitatively different from the Kolmogorov-like turbulence studied in Sections 4.1 and 4.2. Investigating the IR part of the spectrum of non-Abelian gauge fields out of thermal equilibrium is thus certainly an interesting and rewarding project [16].

Some efforts have been spent on the investigation of the infrared parts of the spectrum. Unfortunately, no clear picture has emerged from those studies. As can be seen for instance in Fig. 4.2, there is no indication for presence of very different physics at low momentum. There-

[16] Research in this direction has already been carried out by the authors of [65].

fore, one probably needs to access far lower momenta in order to observe the emergence of new physics. We have carried out an exploratory simulation on an even bigger lattice of 256^3 sites. No evidence for steeper spectra in the far IR was found. Another approach to get a handle on the low-momentum behaviour of the gauge fields is to change the parameters in the initial conditions so that they correspond to a larger physical lattice spacing a_s. Computations using this method did not show signs of the suspected out-of-equilibrium critical behaviour either. In any case, an analytical treatment of the infrared in non-Abelian gauge theories would probably be far more involved than the approach followed in Section 4.2. Instead of the perturbative expansion in powers of g, which will certainly break down at some intermediate momentum, one will probably need to employ an approximation scheme that takes into account the momentum dependence of the vertices. This could be for instance an n-particle irreducible effective action or the functional renormalisation group.

4.4 Discussion

In this Chapter we have demonstrated by numerical as well as analytical means that, following the saturation of plasma instabilities, the gluonic medium evolves towards a quasi-stationary state in the classical limit. This stationary state is characterised by power-law spectra in the statistical propagator and bears remarkable similarities to Kolmogorov turbulence in fluid dynamics. There are strong indications that this UV- fixed point is not present in the full quantum theory.

The numerical result (4.21) for the occupation number exponent κ is in agreement with one of the two possible solutions (cf. Eqns. (4.49) and (4.50)) obtained from 2PI effective action methods in a perturbative setting. This can be regarded as a successful, quantitative confirmation of the applicability of the 2PI resummation scheme to non-Abelian gauge theories. Therefore, one can be optimistic that these methods will become as established for computing the full real-time evolution in non-Abelian gauge theories as they already are for scalar and fermionic fields. For instance, a next step towards this aim could be to benchmark numerical solutions of the 2PI evolution equations against classical-statistical lattice simulations[17] in a similar fashion as it has been done with great success in the scalar case [3–5].

Neither of the solutions for κ that we have found is in agreement with the existing, but contradictory predictions for Kolmogorov turbulence in QCD in the literature. Our numerical and analytical results are incompatible with both a thermal value $\kappa = 1$ (as predicted in [126]) and

[17] Some research in this direction has already been carried out in a project related to [143] and this thesis. However, the agreement found between the two methods so far is at best qualitative and hence no conclusive statement can be made at this point.

$\kappa = 2$, as reported in [18, 19]. No explanation for this obvious disagreement can be given which would be beyond the level of mere speculation. It has to be kept in mind though that all the suggested values for κ have been computed using different formalisms (Boltzmann equations, classical-statistical lattice simulations, 2PI resummation techniques and Vlasov equations based on the hard-loop effective action approach). Thus there is a chance that understanding the causes for the disagreement might allow one to gain further insight into the advantages and domains of applicability of the individual approximations.

As turbulence-like phenomena are almost omnipresent in a vast range of physical systems it is not very surprising that non-Abelian gauge theories with their intricate, inherently nonlinear dynamics exhibit this kind of behaviour, too[18]. What is new in this work is the perspective for the notion of far-from-equilibrium universality [39]. The numerical agreement of the occupation number exponent κ with corresponding results for scalar field theories (*e.g.* [39, 41, 113, 159]) corroborates the suggestion that microscopically very different systems can display universal properties at quasi-stationary, turbulent states. The mismatch between Kolmogorov exponents and the results reported for κ in earlier works [18, 19, 126] rather seemed to confirm the claim that gauge theories are qualitatively different from other physical systems, even in situations that are likely to feature traits of universality. The present work however provides strong evidence for the existence of universality far from thermal equilibrium. The analogy between parametric resonance in inflationary early universe cosmology and plasma instabilities in non-Abelian gauge theories, which has been discussed in Section 3.2, hence persists after the point when initially unstable modes cease to grow exponentially. In this Chapter we have shown that this analogy can even be established on a quantitative level.

We briefly comment on the significance of the UV fixed point for heavy ion collisions. It is unlikely for various reasons that the fixed point studied here is of immediate relevance for experiments at *e.g.* LHC or FAIR. Converting the times measured in units of $\epsilon^{-1/4}$ to fm/c one finds that the times when the quasi-stationary regime is encountered in the simulations are far beyond the presumed life time of the quark gluon plasma in the respective collider experiments. Furthermore, the classical-statistical approximation to the full quantum theory must break down at some intermediate time. Thus it is unclear if quantum effects would ever allow the medium to approach the turbulent regime. Nevertheless, it could be fruitful to explore the possibilities that a scaling solution of the kind (4.12) might offer for instance as an initial condition in hydrodynamic calculations of elliptic flow.

[18] As stated in the introduction to this Chapter, this fact has already been known from several publications before [77, 127, 128, 156, 157].

An obvious complication in the study of turbulent spectra in gauge field correlation functions is the gauge dependence of the latter. In this regard, gauge theories are indeed qualitatively different from other physical systems displaying turbulent behaviour where this difficulty is absent. It is reassuring though that turbulent spectra have been found in Coulomb gauge which can be considered as physical in some sense. Understanding the gauge dependence of the propagators may be even more relevant for a future numerical treatment of the full 2PI evolution equations.

There are intriguing possibilities for further research on Kolmogorov turbulence in QCD. First, it seems highly desirable to describe the fixed point in terms of gauge-invariant quantities on both the analytical and the numerical side. Although the outcome of first numerical attempts of this kind carried out in the context of this thesis was inconclusive this approach should not be abandoned yet. Thoroughly scrutinising *e.g.* correlation functions of gauge-invariant quantities such as the local energy density (2.46) or the components of the energy-momentum tensor might still yield unforeseen results. On the analytical side, a treatment in terms of gauge-invariant quantities is likely to be far more demanding though.

Another exciting way to proceed would be to carry out analogous computations in lower dimensional spacetime. This does not pose too severe a challenge, neither in numerical nor analytical terms and would allow to benchmark the analytical methods of Section 4.2 with similar precision as successfully done in the scalar case [41]. Moreover, it could allow to establish contact to the earlier works [156, 157] in which a fractal dimension has been computed for Yang-Mills fields in (2 + 1) dimensions.

Chapter 5

Conclusions and outlook

In this Chapter we subsume the main results of this thesis and provide a perspective on future research in non-Abelian gauge theories out of thermal equilibrium. We also refer to the discussions in Sections 3.5 and 4.4 at the end of Chapters 3 and 4 for more details.

Two central motivations for this thesis have been stated in the Introduction. The first of these is to scrutinise the *rôle* of plasma instabilities in the early stages of the thermalisation process in heavy ion collisions. Second - but of equal significance - is the aim to contribute to more formal developments in out-of-equilibrium gauge theories, in particular in the framework of the 2PI effective action approach.

In Chapter 3 we have investigated the impact of plasma instabilities on the isotropization process starting from a highly anisotropic initial ensemble. We have found that two kinds of instabilities occur namely initial "primary instabilities" and subsequent "secondary instabilities". The latter set in on a broad domain of intermediate and high momentum modes after a certain period of primary instability growth has elapsed. Understanding the secondary instabilities requires to go beyond hard-loop descriptions. The characteristic time scales (*i.e.* inverse growth rates) of the primary instabilities turn out to be of order 1 fm/c (cf. Eq. (3.21)) which is in the ballpark of the onset of the hydrodynamical regime. It turned out that the extrapolation of primary growth rates to SU(3) gauge theory can be carried out in a controlled way and that the time scales are not altered significantly in the SU(3) case. In both cases however, the rates of the exponential growth do not allow for more than a few $e-$ foldings to take place until the hydrodynamical phase sets in. The secondary instabilities with their higher growth rates have the effect to isotropize an intermediate momentum range of modes but they tend to saturate in higher wavenumber modes before an isotropic state is reached.

The ensuing numerical investigation of the primary instabilities has led to two major insights. Firstly, we have found that the instabilities efficiently render the fields isotropic on large length

scales. It has emerged from our studies that Fourier modes up to approximately 1 GeV become isotropized by the instabilities. This coincides parametrically with the transverse momentum range on which elliptic flow is well reproduced by hydrodynamical calculations with a small shear viscosity [106]. This agreement might thus be an indirect confirmation for the scenario of instability driven isotropization of the quark gluon plasma. The fact that instabilities render the long wavelength degrees of freedom isotropic first is summarised in the term "bottom-up isotropization".

Another central result concerning plasma instabilities is the numerical confirmation of the idea suggested in [76] that Nielsen-Olesen instabilities rather than chromo-Weibel instabilities dominate the physics at early times for the initial conditions Eq. (3.2). The reason behind this is that the anisotropic initial conditions sustain magnetic fields that are approximately homogeneous and hence prone to Nielsen-Olesen instabilities. Investigating Nielsen-Olesen instabilities in an idealised setup we have found out that their growth rates can in principle be higher than for initial conditions of the kind (3.2) by a relevant factor. Therefore we conclude that the Nielsen-Olesen instability could have significant effects on the quark gluon plasma dynamics provided that sufficiently strong and homogeneous fields are present in the initial state of the medium. The question whether this is the case is beyond the scope of this work and needs to be addressed in a different framework. In summary, several questions related to the non-equilibrium time evolution of the quark gluon plasma that is created in collider experiments have been addressed successfully.

Comparing the instability dynamics to the case of parametric resonance in early universe cosmology we have found that also in the gauge theory the secondary instabilities are caused by fluctuation effects induced by higher loop diagrams. The remarkable similarities between these two quite different field theories have also been the subject of the second main part of this thesis.

Also the analysis of the turbulent regime, which is entered after the saturation of plasma instabilities, has yielded several intriguing results. The most important one is the emergence of a quasi-stationary turbulent state whose signature is a characteristic, nonthermal power-law spectrum in the equal-time correlation functions. The exponent of this spectrum could be determined first from a numerical computation. Its value Eq. (4.21) is good agreement with 4/3 and hence clearly nonthermal. From the ensuing analytical calculation employing the 2PI effective action approach in a similar way as for scalar theories in earlier works [39, 41] we have found that the exponents 4/3 and 5/3 are solutions of the fixed-point identity (4.23) at high momenta. It represents a remarkable success of the 2PI formalism for gauge theories that the numerically obtained spectral exponent is in precise agreement with one of the analytical results. In contradiction to former calculations [18, 19, 126] we have found that the spectral index takes the same values as in the scalar case under very similar assumptions. Hence, this clearly confirms the notion of

universality far from thermal equilibrium. The successful application of the 2PI effective action approach at a nonthermal fixed point is an encouragement to employ these methods in more general out-of-equilibrium settings in future work.

Finally, we discuss possible ways to tackle the questions that remain to be answered and provide perspectives on future developments. The approach of Chapter 3 is based to a large extent on the assumption that fermionic degrees of freedom can be neglected in the early phases of the quark gluon plasma's thermalisation. Although this is justified within the colour glass condensate scenario and by the fact that instabilities generically cause a dramatic increase in occupation numbers, it appears worthwhile to check the validity of this approximation. This could be achieved by incorporating fermions into the setup in terms of a Dirac equation coupled to the SU(2) gauge field in analogy to [7].

The study of out-of-equilibrium fixed points offers plenty of opportunities for future work. As already hinted at in Section 4.3, determining and understanding the spectrum of the gluon propagator at low momenta seems very promising in spite of the tough challenges that need presumably to be overcome. Establishing a gauge independent description of the quasi-stationary solutions in the IR as well as in the UV also seems highly desirable

Of course, a major breakthrough would be achieved by computing the full time evolution of an out-of-equilibrium ensemble of non-Abelian gauge fields from first principles within *e.g.* the 2PI formalism[1], at best including quark fields as well. In this way one could study the thermalisation process of the quark gluon plasma directly from QCD. Besides obtaining further insights into the primary and secondary instabilities in the early phase of thermalisation, this would also allow to reveal the significance of the classical fixed point in the full quantum theory. Most important, an estimate for the complete thermalisation time could be obtained in this way.

[1] [143] already represents a study of this kind.

Acknowledgements

It is a great pleasure to express my gratitude to the many people without whose kind support this project could not have reached its final shape.

First and foremost, I would wholeheartedly like to thank my advisor Jürgen Berges, who gave me the opportunity to carry out the research reported upon in this document. Apart from his continuous support and encouragement in plenty of enlightening discussions I would like to thank him also for the many opportunities he granted me to participate in conferences and workshops, in particular at the KITP.

I thank Christian Fischer for his willingness to co-referee this thesis – despite being served a few "surprise pizzas" that really deserved their name at the lunch club seminar.

I say "Köszönöm!" to Dénes Sexty to whom I owe particular gratitude for co-supervising major parts of this project and for the more than three years of very fruitful collaboration.

While carrying out this research I had the pleasure to collaborate on this topic also with (in chronological order) Stefan Roth, Nenad Balanešković and Daniil Gelfand. Their contributions and input to this work are gratefully acknowledged.

Also, I am indebted to Nucu Stamatescu and Jan Pawlowski for granting me the privilege of discussing the progress of this work in the stimulating environment of the Δ- meetings in Heidelberg.

I thank Richard Williams and Jens Pruschke for the proofreading of this thesis. Their support was invaluable in the final stages of polishing this document. The blame for any remaining deficiencies is shouldered by me, of course.

During the entire time of my PhD studies I have profited from the exceedingly pleasant and productive environment in room 413; it never felt like room 101. I thank my office mates, fellow PhD students and the regular visitors Jens Pruschke, Alexander Rothkopf, Dominik Nickel, Thorsten Zöller, Richard Williams, Haris Đapo, Jens Müller, Gernot Eichmann and Jean-Sebastien Gagnon for the many stimulating and fruitful discussions. Everyone else of the IKP theory group is thanked for the friendly and congenial atmosphere on the fourth and fifth floor.

Given that this work has relied to a vast extent on numerical computations, it could not have been carried out without highly qualified and friendly assistance in computing issues. For this I am indebted to Robert Roth, Dénes Sexty, Mathias Wagner, Stefan Roth and Markus Hild. Axel Maas is thanked for sharing his knowledge about gauge-fixing algorithms with me.

I am especially grateful to my parents Herwig and Christiane Scheffler and my grandfather Wilhelm Buch for their continuous support during the entire time of my studies. Finally, I thank my girlfriend Lihui Jin for her great patience and love during the final year of this project.

I deeply apologise to anyone who might feel forgotten here.

Appendix A

List of symbols

The following table summarises the symbols used in this work together with references to their definitions.

Table A.1: List of mathematical symbols used in this work

Symbol	**Explanation**
$[A, B]$	Commutator $AB - BA$.
$\{A, B\}$	Anti-commutator $AB + BA$.
a_s	Spatial lattice spacing, defined in Section 2.3.
A_μ	Matrix-valued gauge field, defined through Eq. (2.1).
A^b_μ	Expansion coefficient of A_μ w. r. t. λ^b defined in (2.4).
$\mathcal{A}^b_\mu$	Ensemble average of A^b_μ, defined in Eq. (2.19) and set to zero in Eq. (3.6).
$\hat{A}^b_\mu$	Dimensionless lattice gauge field, defined in Eq. (2.48) on p. 26.
B^a_j	Magnetic field, given by Eq. (2.37) on the lattice.
$\hat{B}^a_j$	Dimensionless magnetic field, $B^a_j \cdot (g a_s^2)$. Defined in the context of Eq. (2.49).
β_T	Inverse temperature, defined below Eq. (D.1).
$C(x)$	Gauss constraint function from Eqns. (2.12) and (2.13).
D_μ	Covariant derivative, defined in Eq. (2.1).
a_t	Temporal lattice spacing/discrete time step. Defined in Section 2.3.
Δ	Abbreviation for exponents in scaling transform as defined in Eq. (4.38).
Δ_x	Transverse width of the initial distribution in Eq. (3.2).
	(continued on next page)

(List of mathematical symbols cont.)	
Symbol	**Explanation**
$\hat{\Delta}_x$	Δ_x in lattice units, defined in (3.5).
Δ_z	Longitudinal width of the initial distribution in Eq. (3.2).
e_2	Coulomb gauge fixing precision. Defined in Eq. (4.19).
E_j^a	Electric field, given by Eq. (2.37) on the lattice.
$\hat{E}_j^a$	Dimensionless electric field, $E_j^a \cdot (g a_\mathrm{t} a_s)$. Defined below Eq. (2.49).
ϵ	Energy density. Defined in Eq. (2.46).
$\hat{\epsilon}$	Dimensionless energy density in lattice units, defined in (2.50).
ϵ_{abc}	Antisymmetric Levi-Civita tensor.
f_{abc}	Structure constants of SU(N).
$\mathcal{F}_{\mu\nu}(x)$	Matrix-valued field strength. Definition in Eq. (2.5) on p. 14.
$\mathcal{F}_{\mu\nu}^b(x)$	Expansion coefficient of $\mathcal{F}_{\mu\nu}$ w. r. t. λ^b as defined through Eq. (2.5) on p. 14.
$\hat{\mathcal{F}}_{\mu\nu}^b(x)$	Dimensionless lattice field strength defined in Eq. (2.49).
$F_{\mu\nu}^{ab}$	Statistical propagator of the gauge field Eq. (2.22).
$F_{\mu\nu}$	Colour-independent part of the statistical propagator, defined in Eq. (4.1).
$\tilde{F}_{\mu\nu}^{ab}$	Wigner transform of $F_{\mu\nu}^{ab}$ defined in Eq. (4.4).
$G_{\mu\nu}^{ab}$	Time-ordered propagator (Feynman propagator) of the gauge field. Definition in Eq. (2.20).
$G_{\mu\nu}$	Colour-independent part of the statistical propagator, defined through Eq. (4.1).
$G_{\mu\nu}^\mathrm{A}$	Advanced propagator of the gauge field, defined in (2.25).
$G_{\mu\nu}^\mathrm{R}$	Retarded gauge field propagator, defined in (2.26).
$\tilde{G}_{\mu\nu}^\mathrm{A}$,$\tilde{G}_{\mu\nu}^\mathrm{R}$	Wigner transforms of the advanced and retarded propagator. Defined below Eq. (4.4).
$\gamma, \gamma(p_z), \gamma(\mathbf{p})$	Instability growth rate, possibly as a function of momentum or components thereof.
γ_NO	Growth rate of Nielsen-Olesen instabilities. Analytical expression in Eq. (3.34).
Γ	Legendre-transformed generating functional (2.21).
Γ_{2PI}	Two-particle irreducible contribution to Γ in Eq. (2.21).
λ^b	Generators of SU(N), defined in 2.1. Cf. also Section B.
κ	Occupation number exponent, defined through Eq. (4.12) on p. 71.

(continued on next page)

(List of mathematical symbols cont.)	
Symbol	**Explanation**
m_T	Tadpole mass defined in Eq. (3.9).
$P_0[A, \dot{A}]$, $P_0[A, E]$	Probability functional specifying the initial ensemble, defined through Eq. (2.45).
p_z	Longitudinal momentum, *i.e.* the component parallel to the axis of anisotropy. Introduced in 3.1.
p_T	Transverse (w. r. t. the axis of anisotropy) momentum. Introduced in 3.1.
P_L	Longitudinal pressure, cf. Eq. (3.13) on p. 43.
P_T	Transverse pressure, defined in Eq. (3.14) on p. 43.
$\Pi_{(F)}$, $\Pi_{(\rho)}$	Symmetric and anti-symmetric part of the gluon self-energy in the decomposition (2.24).
$\tilde{\Pi}_{(F)}$, $\tilde{\Pi}_{(\rho)}$	Wigner transforms of $\Pi_{(F)}$ and $\Pi_{(\rho)}$ as defined in Eq. (4.7).
ρ_0	Density matrix at initial time. Introduced in Section 2.2.
$\rho^{ab}_{\mu\nu}$	Spectral function, defined in (2.23) on p. 19.
$\rho_{\mu\nu}$	Colour-independent part of $\rho^{ab}_{\mu\nu}$, defined through Eq. (4.1).
$\tilde{\rho}^{ab}_{\mu\nu}$	Wigner transform of $\rho^{ab}_{\mu\nu}$ as defined in Eq. (4.4).
σ^b	Pauli matrices. Cf. Eq. (B.2) for explicit expressions.
$\mathcal{T}$	Time-ordering along the Schwinger-Keldysh contour introduced in Section 2.2.
Θ	Heaviside- Theta function.
$U_\mu(x)$	Link variable as defined in Eq. (2.30) on p. 22.
$U_{\mu\nu}(x)$	Plaquette variable defined in Eq. (2.32).
$V_3^{\mu\kappa\rho,abc}(p,k,q)$	Three-gluon vertex defined in Eq. (4.26).
$V_3^{\mu\kappa\rho}(p,k,q)$	Colour-independent part of V_3. Defined through Eq. (4.27).
$V^{\mu\nu\rho\sigma}_{4\ abcd}$	Four-gluon vertex. Definition in Eq. (3.25).
ξ	Bulk anisotropy measure, defined in Eq. (3.11).

Appendix B

Notation and conventions

We use the convention

$$g_{\mu\nu} = \mathrm{diag}(+1, -1, -1, -1) \tag{B.1}$$

for the metric on Minkowski space-time.

Greek indices denote Lorentz indices taking the values $0, 1, 2, 3$ corresponding to the coordinates t, x, y, z, respectively. Lower case Latin indices $i, j, k, ...$ refer to spatial indices and take values in $\{1, 2, 3\}$. Lower case Latin indices $a, b, c, ...$ refer to "colour" occurring for instance in the decomposition of gauge fields with respect to the generators of the SU(N)- Lie algebra.

If not stated otherwise, we employ the summation convention for contractions of Lorentz indices, spatial indices, and colour indices.

The Pauli matrices are denoted by σ^a, $a = 1, 2, 3$. They are explicitly given by

$$\sigma^1 = \begin{pmatrix} 0 & 1 \\ 1 & 0 \end{pmatrix} \qquad \sigma^2 = \begin{pmatrix} 0 & -i \\ i & 0 \end{pmatrix} \qquad \sigma^3 = \begin{pmatrix} 1 & 0 \\ 0 & -1 \end{pmatrix} . \tag{B.2}$$

Matrices $U \in \mathrm{SU}(2)$ are frequently decomposed as

$$U \equiv u_0 \mathbb{1} + i\mathbf{u} \cdot \sigma \tag{B.3}$$

with $u_0, u_a \in \mathbb{R}$ subject to the constraint $u_0^2 + \mathbf{u}^2 = 1$. Eq. (B.3) can be inverted as

$$\begin{aligned} u_0 &= \frac{1}{2} \mathrm{Tr} U = \pm \sqrt{1 - \mathbf{u}^2} \\ u_a &= \frac{1}{2i} \mathrm{Tr}(\sigma^a U) . \end{aligned} \tag{B.4}$$

The gauge fields A_μ and field strength $\mathcal{F}_{\mu\nu}$ are hermitian matrices *i.e.* $A_\mu^\dagger = A_\mu$ and analogously for $\mathcal{F}_{\mu\nu}$). They can be decomposed with respect to the generators λ^a of SU(N) as

$$\begin{aligned} A_\mu &= A_\mu^b \lambda^b \\ \mathcal{F}_{\mu\nu} &= \mathcal{F}_{\mu\nu}^b \lambda^b \ . \end{aligned} \tag{B.5}$$

The normalisation of the generators λ^a follows the usual convention $\mathrm{Tr}(\lambda^a \lambda^b) = \frac{1}{2}\,\delta^{ab}$. Especially, $\lambda^b = \sigma^b/2$ in the case of SU(2).

For any function $f(x) \equiv f(t, \mathbf{x})$ on spacetime we denote the Fourier transforms by the same symbol, indicating by the argument that it is the Fourier transform. We reserve the letters k, q, p for momenta. For example, $f(k) = f(k^0, \mathbf{k})$ would denote the Fourier transform of $f(x)$ w. r. t. four-momentum while $f(t, \mathbf{p})$ denotes its time-dependent, spatial Fourier transform. We tolerate the slight ambiguities of this notation because it is frequently used in the physics literature.

Appendix C

Numerical stability analysis

In this Section we present some calculations that demonstrate the numerical stability of our results in Chapters 3 and 4. All data shown in this Section were obtained for $g = 1$ starting the time evolution from an initial ensemble of the kind defined through Eq. (3.2).

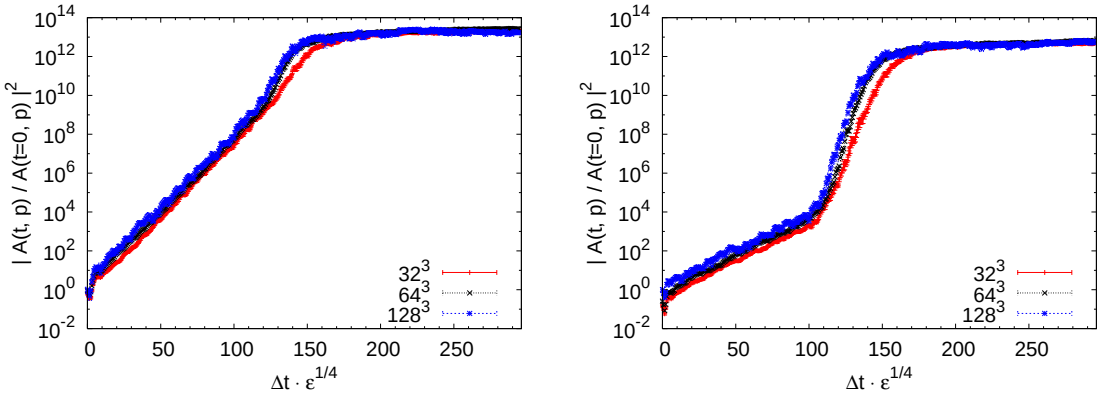

(a) $p_z = 0.5\,\epsilon^{1/4}$ (b) $p_z = 0.8\,\epsilon^{1/4}$

Figure C.1: Estimating the impact of finite-volume effects. Fourier coefficients of the gauge field as in Fig. 3.3 computed for three different lattice volumes. While the curves computed on 64^3- and 128^3- lattices coincide very well, the one from the 32^3- lattice (red) shows minor deviations.

Fig. C.1 demonstrates the insensitivity of our results under changes of the physical lattice volume. As in Fig. 3.3, we have plotted the squared modulus of the gauge field Fourier modes versus time obtained from lattices of 32^3, 64^3 and 128^3 sites. On all lattices we have chosen modes parallel to the z- axis with equal magnitude $p \simeq 0.5\,\epsilon^{1/4}$ and $p \simeq 0.8\,\epsilon^{1/4}$ for the left and the right graph of Fig. C.1, respectively. Volume dependencies are hardly perceivable for lattices of size 64^3 or larger and the deviations that occur on the smallest lattice are not very pronounced

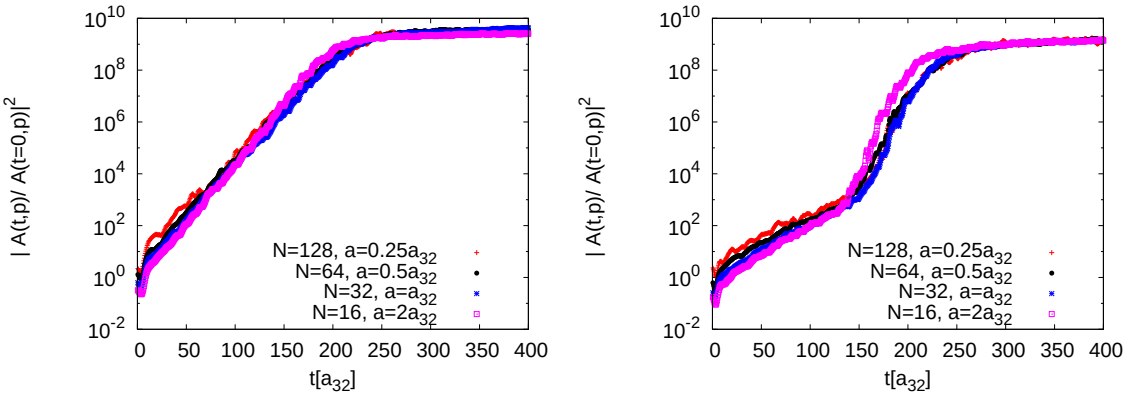

Figure C.2: Checking for cutoff artefacts. The time evolution of the first and second non-zero mode parallel to z-axis plotted for systems with different lattice spacings. Time is measured in units of the lattice spacing of the 32^3- lattice. The left graph employs the momentum $p = 0.20/a_{32}$ while the right graph uses $p = 0.39/a_{32}$. The ordering of the legend corresponds to the ordering of the curves from top to bottom at $t = 0$.

either. Since our computations have been carried out on 64^3 or 128^3 lattices we infer that they represent the infinite volume very well[1].

Given that the UV part of the spectrum is excited only weakly in the initial conditions (3.2), the dependence on the UV cutoff (*i.e.* the lattice spacing a_s) should be mild and well-controlled as well. In Fig. C.2 the time evolution of Fourier modes is plotted as obtained from simulations on lattices of different lattice spacings but same physical volume. We have chosen the first and the second non-zero momentum of the 32^3- lattice in the z- direction. The lattice spacings are $a = 0.25, 0.5, 1, 2$ in units of the lattice spacing used for the results presented in Chapter 3. One observes from Fig. C.2 that the results are insensitive to UV cutoff changes if the lattice spacing employed in this work or smaller is used.

In the explanation of the initial conditions in Section 3.1 it was stated below Eq. (3.6) that gauge field modes in Fourier space whose amplitude is smaller than a certain limit are initialised with a noise term. We have to demonstrate that our results do not depend on the amplitude of this noise. To that end, we replot the time evolution of the gauge field's first non-zero Fourier coefficient along the z- axis in Fig. C.3 (Apart from the units chosen here this is completely analogous to Fig. 3.3.). One sees that as long as the amplitude of the noise plateau is not chosen too big (as in the uppermost, red curve) the growth rate is not altered. On the contrary, the exact time when the saturation of plasma instabilities occurs is changed. However, this does not

[1] A further remark on the volume insensitivity of the spectral index κ can be found in the discussion of Eq. (4.21).

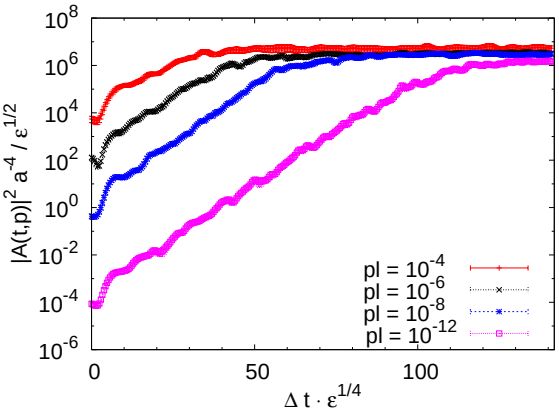

Figure C.3: Checking plateau independence. The instability growth rates turn out to be insensitive to the noise level as long as the latter is not chosen too high.

pose any problems because we are only interested in the growth rates of the instabilities; cf. the remarks in the discussion of Fig. 3.3 in Section 3.2.

Appendix D

Simulations in thermal equilibrium

In this appendix we present some results of real-time simulations of the Yang-Mills system in thermal equilibrium. The purpose of this is twofold. First, it represents yet another check of the program used for the numerical simulations. Second, studying equilibrium configurations allows to benchmark the non-equilibrium results presented in Chapters 3 and 4. Therefore, it provides valuable complementary information.

Classical real-time simulations of non-Abelian lattice gauge theories in thermal equilibrium have been studied extensively in the literature [9–11, 97, 99–101, 115–118, 148]. Most of these publications are concerned with the determination of the sphaleron rate in the early universe. More recently, the evaluation of effective potentials for heavy quarks has emerged as a problem which is amenable to classical lattice simulations (see [99, 101] and references therein). All algorithms that are discussed in this Section have been applied in these former works and therefore this Section does not contain anything new in this regard.

In order to study real-time evolution in thermal equilibrium we employ the same program as in the rest of this work in order to integrate the field equations (2.41). The only difference resides in the choice of initial conditions. While we have sampled initial field configurations from the out-of-equilibrium ensemble (3.2) in the main body of this work we would now like to initialise the link variables and their canonically conjugate momenta from a canonical thermal ensemble[1]. We briefly discuss some technical issues that are important for the thermal sampling, closely following [9, 116] to which we refer for a more detailed presentation.

The task is to sample the gauge field (or, equivalently, the spatial link variables) and the electric field in temporal axial gauge (Eqns. (2.14) and (2.39)) at initial time from the canonical

[1]Note the initial conditions of Section 3.1 realise a fixed-energy ensemble that should evolve towards the micro-canonical ensemble at asymptotically late times. In this appendix however we will consider the canonical ensemble where the energy is allowed to fluctuate. This will still allows to draw some conclusion because the description of thermodynamics is equivalent in both ensembles in the thermodynamic limit.

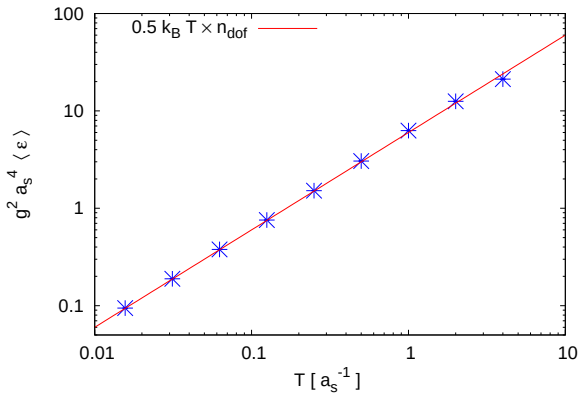

(a)

Figure D.1: Average energy per lattice site in units of $g^{-2}a_s^{-4}$ as a function of temperature T. $\mathrm{n_{dof}}$ denotes the number of degrees of freedom per lattice site which equals twelve for SU(2) gauge theory.

distribution

$$P_0[A,E] \propto \exp\left\{-\beta\, H[E,A]\right\}\delta[C] \tag{D.1}$$

where $\beta_T \equiv 1/(k_B T)$ is the inverse temperature[2] (with $k_B = 1$ in the following), H is the lattice Hamiltonian [93] which can be computed as an integral over the local energy density Eq. (2.46) and C denotes the Gauss constraint (2.13). Sampling a thermal distribution of the kind $p \propto e^{-\beta_T H}$ is a standard task in Monte Carlo simulations. A minor, purely technical complication in sampling from the distribution (D.1) is posed by the presence of Gauss constraint. Sampling field configurations satisfying this constraint is described in the literature by several authors [9, 97, 116], which we concisely subsume now.

Note from Eq. (2.46) that

$$\epsilon(x) = \frac{1}{2}\sum_{j,a}(E_j^a(x))^2 \;+\; \frac{2N}{g^2 a_s^4}\sum_{j<k}\left[1 - \frac{1}{2N}\left(\mathrm{Tr}\, U_{jk}(x) + \mathrm{Tr}\, U_{jk}^\dagger(x)\right)\right] + O(ga^2)\,. \tag{D.2}$$

Thus the electric fields appear in the form of a Gaussian distribution in Eq. (D.1) which can numerically be sampled in a straightforward way. However, given an arbitrary configuration of spatial link variables U_j a generic configuration of electric fields will not satisfy the Gauss constraint (2.44). There are several methods to remove the unphysical degrees of freedom that violate the Gauss constraint. We will exclusively consider the algorithm from [116] here[3]. Equipped

[2] The authors of some of the above mentioned publications prefer to absorb the factor of $2\mathrm{N}_c/g^2$ into the definition of β_T. We refrain from this convention here in order to facilitate the comparison to our previous results.

[3] Actually, Moore outlines two algorithms to accomplish the removal of constraint violations in [116]. The algorithm applied here is the one presented first in that paper.

with a routine that enforces the Gauss constraint a possible procedure to sample thermal gauge field configurations can be summarised as follows [116]:

0. Set all spatial links variables to $\mathbb{1}$ ("cold start").

1. Bring the electric fields into contact with a heat bath of the desired temperature $\beta_T = 1/T$. This amounts to sample their values from a Gaussian distribution, as can be inferred from Eqns. (D.1) and (D.2).

2. Enforce the Gauss constraint.

3. Allow the electric fields to share energy with the magnetic degrees of freedom by running the real-time evolution for a period of order β_T.

4. Repeat steps 1 - 3 about ten times.

It is claimed in [116] that this algorithm is more efficient than the one presented in [97]. The authors of [99] suggest to carry out heat-bath sweeps over the spatial plaquettes before commencing the above procedure. They report that this renders the thermalisation algorithm even faster, but we have not made use of this here. For the results presented in this Section we have chosen to run the real-time evolution in step 3 for a time of $10\beta_T$ thus ensuring that the electric and magnetic fields have sufficient time to share energy.

Having described how equilibrium configurations can be sampled we turn to the presentation of a few numerical results employing thermal initial conditions.

In Fig. D we have plotted the average energy density per lattice site as a function of the temperature T. The straight line shows $T\, n_{\text{d.o.f.}}/2$ with $n_{\text{d.o.f.}} = 12$ (Four degrees of freedom for each of the three adjoint colours of SU(2) per lattice site.). One observes very good agreement. Deviations seem to occur only at the highest temperatures. This expected because the compactness of the gauge group does not allows for the deposition of arbitrarily high energies in the link variables.

Next we present a few plots serving to benchmark calculations in Chapter 3. In particular, we are interested in the ratios of Fourier coefficients introduced in Eqns. (3.15) and (3.16). It has been asserted in the context of those equations that these ratios are equal to one in an isotropic state such as thermal equilibrium. Although this is intuitively clear it is interesting to check this claim by numerical means.

In Fig. D.2 we compare the ratio from Eq. (3.15) as obtained from simulations in and out of thermal equilibrium. The individual panels show the data for the ratio (3.15) for a selection of four different momenta representing low, intermediate and high lattice momenta. The out-of-equilibrium data was computed from an ensemble of initial conditions as defined Eq. (3.2) with

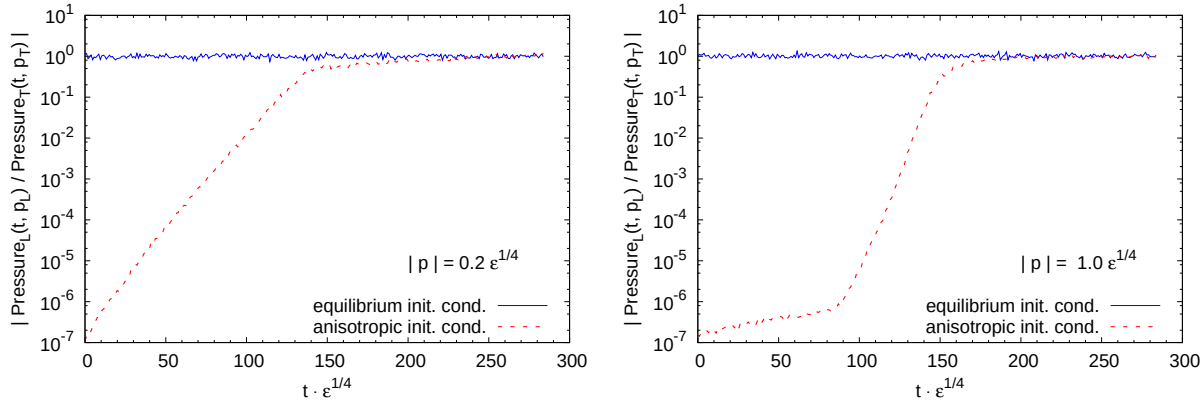

(a) $|p| = 0.2\,\epsilon^{1/4}$

(b) $|p| = 1.0\,\epsilon^{1/4}$

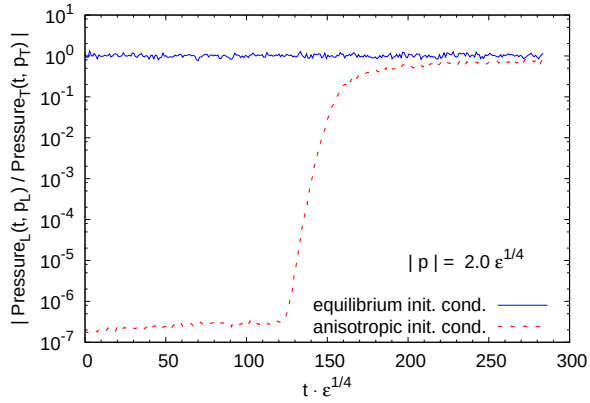

(c) $|p| = 2.0\,\epsilon^{1/4}$

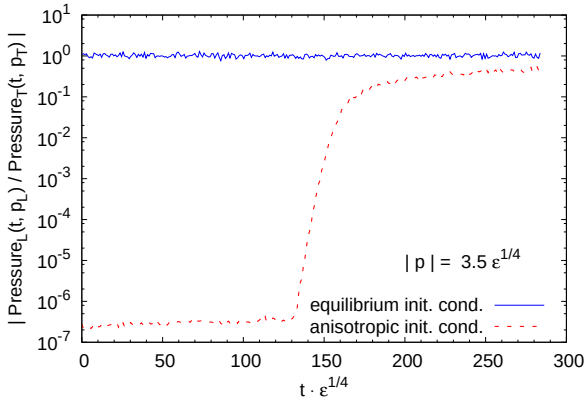

(d) $|p| = 3.5\,\epsilon^{1/4}$

Figure D.2: The ratio (3.15) computed for anisotropic non-equilibrium initial conditions (3.2) (lower, red lines) and for equilibrium initial conditions (upper, blue lines). In both simulations the average lattice energy density was adjusted to $\hat{\epsilon} = 0.05$ within a few per cent. The size of the error bars is below the resolution of this plot.

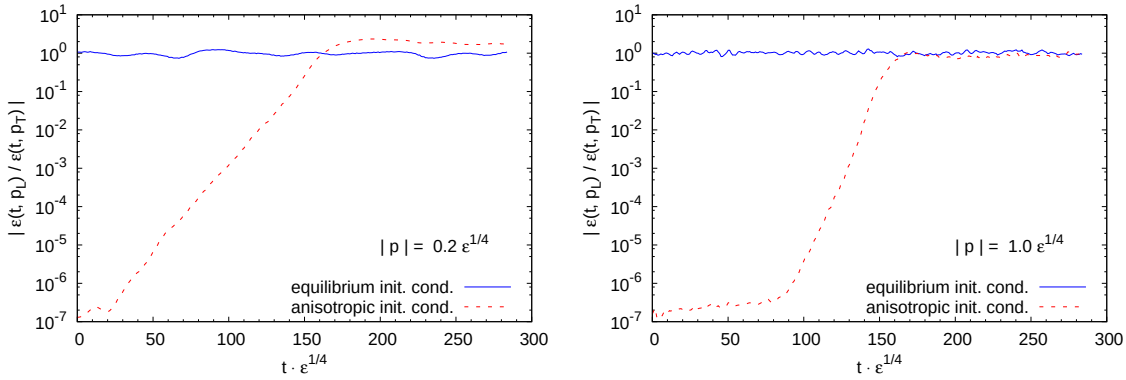

(a) $|p| = 0.2\,\epsilon^{1/4}$ (b) $|p| = 1.0\,\epsilon^{1/4}$

Figure D.3: Similar to Fig. D.2 but showing the ratio (3.16) of Fourier coefficients of the local energy density (2.46). The data stems from the same simulations as in Fig. D.2. Red lines: anisotropic nonequilibrium initial conditions (3.2). Blue, approximately constant lines: thermal equilibrium initial conditions.

identical parameters[4] as for Fig. 3.7. The thermal ensemble employed to compute the equilibrium curves encompassed fifty configurations while the out-of-equilibrium had one hundred members. The inverse temperature of the thermal ensemble was adjusted to yield the same average energy density as in the out-of-equilibrium with a small margin of error. It is immediately apparent from Fig. D.2 that the equilibrium value of the ratios (3.15) is indeed one and that the deviations from the average value caused by the finiteness of the ensemble are tiny. As discussed in detail in Section 3.2, the non-equilibrium instabilities drive the system towards an isotropic state. While the IR modes do become isotropic quickly, a sizable anisotropy remains in the UV as can be seen by comparing the panels (a) and (b) with panels (c) and (d) in Fig. D.2.

In Fig. D.3 we show analogous results based on the Fourier spectrum of the energy (cf. Eq. (3.16)) as for the pressure in Fig. D.2. Basically, all comments made on the latter also apply here. It is interesting to observe that the plasma instabilities seem to slightly overpopulate the low-momentum modes, which can be observed in Fig. D.3.

Having benchmarked some calculations from Chapter 3, we now turn to compare some results from Section 4.1 to their equilibrium counterparts. Doing so we will gain some insights into (i) the gauge dependence of the statistical propagator (2.22) and (ii) the possible precision of the determination of the spectral index κ which has been the central quantity of interest in Chapter 4.

It was mentioned in Section 4.1 that the spectra $A^a_j(t, \mathbf{p})$ exhibit strong gauge dependencies.

[4]The data underlying Figs. D.2 and D.3 has a been acquired from a new calculation with a more frequent computation of physical observables than most of the data in Chapter 3, as a closer look will reveal. The initial conditions were identical however.

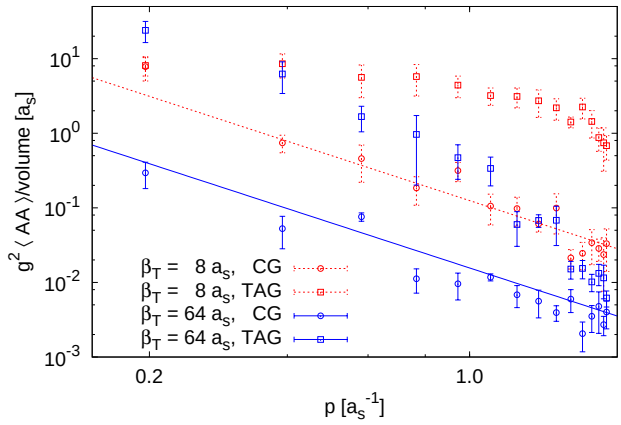

Figure D.4: Equal-time correlation function of the gauge field as a function of momentum for two different temperatures in both temporal axial gauge (squares) and Coulomb gauge (circles). Blue data points give the results for the cooler ensemble ($\beta_T = 64a_s$), red data points for the warmer one ($\beta_T = 8a_s$). The straight lines represent the respective $T/\mathbf{p}^2$. The data shown here stem from a small ensemble (five configurations) of 32^3 lattices and should hence be regarded as illustrative only.

In particular, scaling behaviour according to Eq. (4.12) could only be found in Coulomb but not in temporal axial gauge. We would like to check if the expected scaling in the particle number $n(\mathbf{p}) \propto T/\omega(\mathbf{p}) \simeq T/|\mathbf{p}|$ can be found in (classical) thermal equilibrium, at least at high momentum. By the argumentation of Chapter 4 such a functional shape of $n(\mathbf{p})$ would manifest itself in the equal-time gauge field correlation function (4.14) by scaling of the kind $F(t, \mathbf{p}) \sim T/\mathbf{p}^2$ (That is, $\kappa = 1$ in Eqns. (4.12) and (4.15).

Fig. D.4 shows the outcome of an exploratory study[5] comparing spectra in Coulomb and temporal axial gauge[6] at two different temperatures. Also included is the expected, classical thermal scaling behaviour for both temperatures by straight lines. All data for the lower temperature ($\beta_T = 64a_s$) are printed in blue, while the data for the higher temperature ($\beta_T = 8a_s$) is plotted in red. Coulomb gauge spectra are represented by circles while the squares give the results for temporal axial gauge. The result is quite striking. In spite of the rather large error bars (We will consider data with better statistics further below) one can immediately learn that only the Coulomb gauge correlation functions have a chance to reproduce the expected scaling behaviour. This finding confirms that it is advantageous to use Coulomb gauge in the investigation

[5]These data were gathered on ensembles of only five 32^3 lattices.

[6]The temporal axial gauge condition (2.14) still permits time independent gauge transformations. In the data presented here we have not fixed this remaining gauge freedom. A possible way to accomplish this would be to require the Coulomb gauge condition (2.15) be fulfilled at a certain instant of time, *e.g.* at $t = 0$. Of course, the two gauges would then yield identical results at $t = 0$. It would be interesting to study if the time evolution causes the spectra to deviate again.

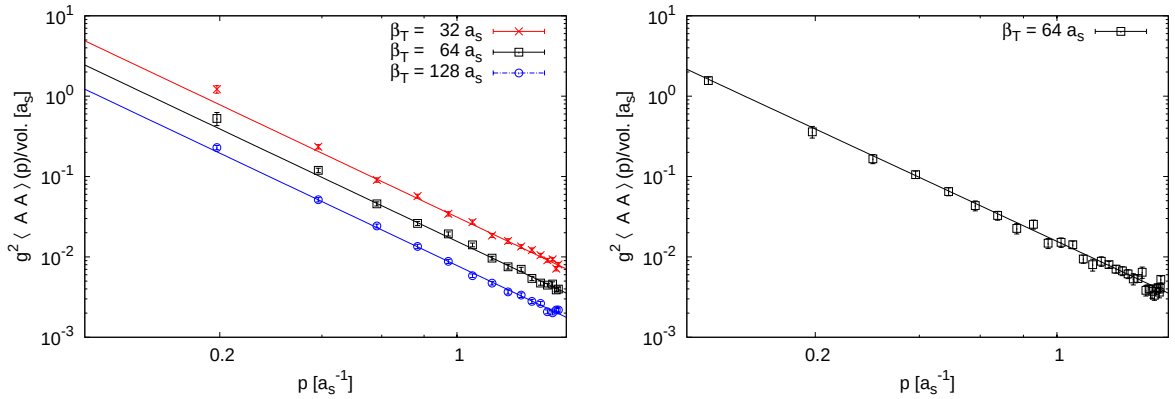

Figure D.5: Gauge field spectra in Coulomb gauge in thermal equilibrium. (a): Gauge-field spectra for three different temperatures on relatively small lattices (32^3) but with good statistics (100 runs). (b): Spectrum for $\beta_T = 64a_s$ together with $T/\mathbf{p}^2$ obtained on a large lattice (64^3) from twenty configurations. The straight lines give the corresponding $T/\mathbf{p}^2$ in both subfigures.

of scaling behaviour as mentioned in Chapter 4.

Figs. D.5(a) and (b) ought to be compared with Fig. 4.2 in Section 4.1. They serve to provide further evidence for the nonthermal nature of the fixed point presented there. All data here stem from configurations that were fixed to Coulomb gauge. Panel (a) displays the equal-time correlation function of the gauge field as a function of $|\mathbf{p}|$ for various temperatures together with the corresponding curve $T/\mathbf{p}^2$, which is expected from the high-temperature limit of the Bose-Einstein distribution. The agreement is remarkably good. The underlying data were produced on rather small lattices of 32^3 sites, however with good statistics (100 configurations each). Panel (b) contains a plot of the gauge field correlation function obtained at $\beta_T = 64a_s$, this time computed on a 64^3- lattice (20 runs). Again, the agreement with the theoretically expected curve is very good.

From fitting a power-law function (4.15) to the thermal spectra in Fig. D.5 we can gain some insights into the reliability of the numerical result quoted in Eq. 4.21 for κ at the nonthermal fixed point. In Figs. D.6(a) and (b) the fit results are plotted for fitting the occupation number exponent κ. This is similar to Figs. 4.3 and 4.4 from Section 4.1. Here however, κ is not plotted as a function of time because the system is in equilibrium and thus stationary. The numbers on the abscissa refer to fits to different ensemble members. The fits underlying Fig. D.6(a) were carried out on the same part of the spectrum as used for the transverse spectra in Section 4.1. The exponents in panel (b) however were fitted to the entire available data. Averaging the results yields

$$\kappa = 0.997 \pm 0.013 \quad , \quad |\mathbf{p}| \cdot a_s \in [0.3, 1.5] \tag{D.3}$$

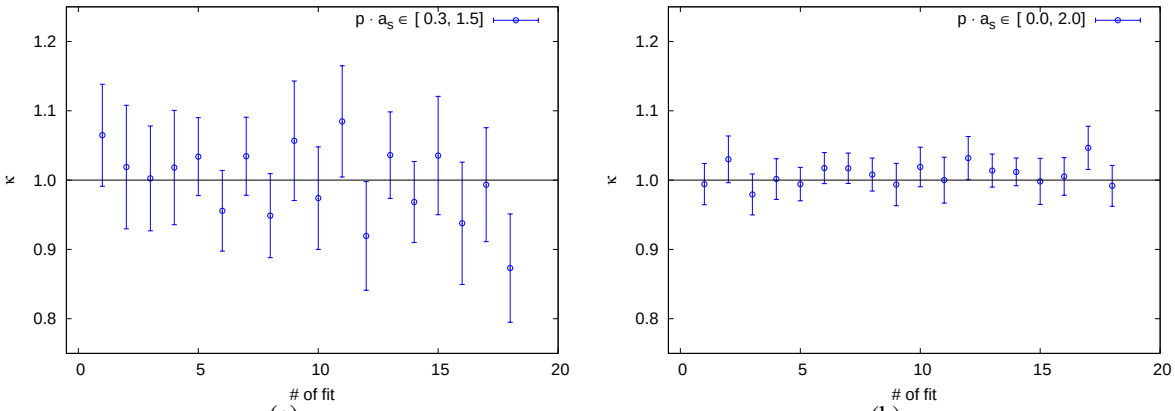

Figure D.6: Results for the spectral index κ. (a): Fit results for the occupation number exponent κ obtained from the same simulation as the data in Fig. D.5(a) fitted on the same momentum interval as used in Section 4.1. (b): Fit results for κ exploiting the entire set of data.

in the case of the restricted fit interval (data in Fig. D.6(a)) and

$$\kappa = 1.009 \pm 0.004 \quad , \quad |\,\mathbf{p}\,| \cdot a_s \in \,]0.0, 2.0] \tag{D.4}$$

for the data in Fig. D.6(b). Note that the distribution of lattice momenta in the interval $[0.0, 2.0]$ along a coordinate axis is not homogeneous as can be inferred from Eq. (3.1). On the contrary, there is an accumulation of modes with momenta close to the maximum so that the number of data points taken into account in (D.4) is much bigger than suggested by the size of the respective momentum domains.

Several important conclusions can be drawn from these results. First, both values are in excellent agreement with the $\kappa = 1$ which is expected for classical thermal equilibrium. Second, the error bars of either result ((D.3) or (D.4)) are so small that the estimates for the thermal κ are certainly incompatible with the non-equilibrium value (4.21) obtained in Section 4.1. This rules out the possibility that the results of Section 4.1 represent an unlucky fit to an actually thermal spectrum. Therefore, the results in Eqns. (D.3) and (D.4) indirectly prove the nonthermal nature of the quasi-stationary state encountered the out-of-equilibrium simulations of Chapter 4.

Finally, we can use the results of this Section to check the reliability of the statistical error estimate in Eq. (4.21). Recall that the latter was computed as an average of eight estimates for κ displayed in Fig. 4.4. We have employed subsamples of eight data points from Fig. D.5(a) to re-compute the result in Eq. D.3 and its error estimate. This yields statistical errors for κ in the range 0.01 to 0.03, which is compatible with the statistical error of the nonthermal κ in Eq. (4.21). This confirms the accuracy of the error estimate in the latter equation.

Bibliography

[1] G. Aarts, Can complex Langevin dynamics evade the sign problem?, PoS LAT2009 (2009) 024.

[2] G. Aarts, Can stochastic quantization evade the sign problem? – the relativistic Bose gas at finite chemical potential, Phys. Rev. Lett. 102 (2009) 131601.

[3] G. Aarts, J. Berges, Classical aspects of quantum fields far from equilibrium, Phys. Rev. Lett. 88 (2002) 041603.

[4] G. Aarts, G. F. Bonini, C. Wetterich, On thermalization in classical scalar field theory, Nucl. Phys. B587 (2000) 403–418.

[5] G. Aarts, G. F. Bonini, C. Wetterich, Exact and truncated dynamics in nonequilibrium field theory, Phys. Rev. D63 (2001) 025012.

[6] G. Aarts, N. Laurie, A. Tranberg, Effective convergence of the 2PI-1/N expansion for nonequilibrium quantum fields, Phys. Rev. D78 (2008) 125028.

[7] G. Aarts, J. Smit, Real-time dynamics with fermions on a lattice, Nucl. Phys. B555 (1999) 355–394.

[8] G. Aarts, I.-O. Stamatescu, Stochastic quantization at finite chemical potential, JHEP 09 (2008) 018.

[9] J. Ambjorn, T. Askgaard, H. Porter, M. E. Shaposhnikov, Sphaleron transitions and baryon asymmetry: A Numerical real time analysis, Nucl. Phys. B353 (1991) 346–378.

[10] J. Ambjorn, A. Krasnitz, The classical sphaleron transition rate exists and is equal to $1.1(\alpha_w T)$ 4, Phys. Lett. B362 (1995) 97–104.

[11] J. Ambjorn, A. Krasnitz, Improved determination of the classical sphaleron transition rate, Nucl. Phys. B506 (1997) 387–403.

[12] J. O. Andersen, M. Strickland, Three-loop Phi-derivable approximation in QED, Phys. Rev. D71 (2005) 025011.

[13] A. Andronic, F. Beutler, P. Braun-Munzinger, K. Redlich, J. Stachel, Thermal description of hadron production in e+e- collisions revisited, Phys. Lett. B675 (2009) 312–318.

[14] Y. Aoki, G. Endrodi, Z. Fodor, S. D. Katz, K. K. Szabo, The order of the quantum chromodynamics transition predicted by the standard model of particle physics, Nature 443 (2006) 675–678.

[15] P. Arnold, J. Lenaghan, The abelianization of QCD plasma instabilities, Phys. Rev. D70 (2004) 114007.

[16] P. Arnold, J. Lenaghan, G. D. Moore, QCD plasma instabilities and bottom-up thermalization, JHEP 08 (2003) 002.

[17] P. Arnold, J. Lenaghan, G. D. Moore, L. G. Yaffe, Apparent thermalization due to plasma instabilities in quark gluon plasma, Phys. Rev. Lett. 94 (2005) 072302.

[18] P. Arnold, G. D. Moore, QCD plasma instabilities: The nonabelian cascade, Phys. Rev. D73 (2006) 025006.

[19] P. Arnold, G. D. Moore, The turbulent spectrum created by non-Abelian plasma instabilities, Phys. Rev. D73 (2006) 025013.

[20] P. Arnold, G. D. Moore, Non-Abelian Plasma Instabilities for Extreme Anisotropy, Phys. Rev. D76 (2007) 045009.

[21] P. Arnold, G. D. Moore, L. G. Yaffe, The fate of non-abelian plasma instabilities in 3+1 dimensions, Phys. Rev. D72 (2005) 054003.

[22] A. Arrizabalaga, J. Smit, Gauge-fixing dependence of Phi-derivable approximations, Phys. Rev. D66 (2002) 065014.

[23] A. Arrizabalaga, J. Smit, A. Tranberg, Tachyonic preheating using 2PI - 1/N dynamics and the classical approximation, JHEP 10 (2004) 017.

[24] A. Arrizabalaga, J. Smit, A. Tranberg, Equilibration in phi**4 theory in 3+1 dimensions, Phys. Rev. D72 (2005) 025014.

[25] R. Baier, A. H. Mueller, D. Schiff, D. T. Son, 'bottom-up' thermalization in heavy ion collisions, Phys. Lett. B502 (2001) 51–58.

[26] N. Balanešković, Nichtgleichgewichts-Anfangsbedingungen für Plasma-Instabilitäten. Bachelor- Thesis, Technische Universität Darmstadt, 2008.

[27] G. Baym, Selfconsistent approximation in many body systems, Phys. Rev. 127 (1962) 1391–1401.

[28] F. Becattini, M. Gazdzicki, A. Keranen, J. Manninen, R. Stock, Study of chemical equilibrium in nucleus nucleus collisions at AGS and SPS energies, Phys. Rev. C69 (2004) 024905.

[29] J. Berges, Controlled nonperturbative dynamics of quantum fields out of equilibrium, Nucl. Phys. A699 (2002) 847–886.

[30] J. Berges, n-PI effective action techniques for gauge theories, Phys. Rev. D70 (2004) 105010.

[31] J. Berges, Introduction to nonequilibrium quantum field theory, AIP Conf. Proc. 739 (2005) 3–62.

[32] J. Berges, S. Borsanyi, J. Serreau, Thermalization of fermionic quantum fields, Nucl. Phys. B660 (2003) 51–80.

[33] J. Berges, S. Borsanyi, D. Sexty, I. O. Stamatescu, Lattice simulations of real-time quantum fields, Phys. Rev. D75 (2007) 045007.

[34] J. Berges, S. Borsanyi, C. Wetterich, Prethermalization, Phys. Rev. Lett. 93 (2004) 142002.

[35] J. Berges, S. Borsanyi, C. Wetterich, Isotropization far from equilibrium, Nucl. Phys. B727 (2005) 244.

[36] J. Berges, J. Cox, Thermalization of quantum fields from time-reversal invariant evolution equations, Phys. Lett. B517 (2001) 369–374.

[37] J. Berges, T. Gasenzer, Quantum versus classical statistical dynamics of an ultracold Bose gas, Phys. Rev. A76 (2007) 033604.

[38] J. Berges, D. Gelfand, S. Scheffler, D. Sexty, Simulating plasma instabilities in SU(3) gauge theory, Phys. Lett. B677 (2009) 210–213.

[39] J. Berges, G. Hoffmeister, Nonthermal fixed points and the functional renormalization group, Nucl. Phys. B813 (2009) 383–407.

[40] J. Berges, J. Pruschke, A. Rothkopf, Instability-induced fermion production in quantum field theory, Phys. Rev. D80 (2009) 023522.

[41] J. Berges, A. Rothkopf, J. Schmidt, Non-thermal fixed points: effective weak-coupling for strongly correlated systems far from equilibrium, Phys. Rev. Lett. 101 (2008) 041603.

[42] J. Berges, S. Scheffler, D. Sexty, Bottom-up isotropization in classical-statistical lattice gauge theory, Phys. Rev. D77 (2008) 034504.

[43] J. Berges, S. Scheffler, D. Sexty, Turbulence in nonabelian gauge theory, Phys. Lett. B681 (2009) 362–366.

[44] J. Berges, J. Serreau, Parametric resonance in quantum field theory, Phys. Rev. Lett. 91 (2003) 111601.

[45] J. Berges, D. Sexty, Real-time gauge theory simulations from stochastic quantization with optimized updating, Nucl. Phys. B799 (2008) 306–329.

[46] J. Berges, I. O. Stamatescu, Simulating nonequilibrium quantum fields with stochastic quantization techniques, Phys. Rev. Lett. 95 (2005) 202003.

[47] R. S. Bhalerao, J.-P. Blaizot, N. Borghini, J.-Y. Ollitrault, Elliptic flow and incomplete equilibration at RHIC, Phys. Lett. B627 (2005) 49–54.

[48] K. Blagoev, F. Cooper, J. Dawson, B. Mihaila, Schwinger-Dyson approach to non-equilibrium classical field theory, Phys. Rev. D64 (2001) 125003.

[49] J.-P. Blaizot, E. Iancu, The quark-gluon plasma: Collective dynamics and hard thermal loops, Phys. Rept. 359 (2002) 355–528.

[50] D. Bödeker, The impact of QCD plasma instabilities on bottom-up thermalization, JHEP 10 (2005) 092.

[51] D. Bödeker, K. Rummukainen, Non-abelian plasma instabilities for strong anisotropy, JHEP 07 (2007) 022.

[52] G. F. Bonini, C. Wetterich, Time evolution of correlation functions and thermalization, Phys. Rev. D60 (1999) 105026.

[53] A. Branschädel, T. Gasenzer, 2PI nonequilibrium versus transport equations for an ultracold Bose gas, J. Phys. B41 (2008) 135302.

[54] P. Braun-Munzinger, J. Wambach, The Phase Diagram of Strongly-Interacting Matter, arXiv:0801.4256 [hep-ph].

[55] E. Calzetta, B. L. Hu, Nonequilibrium Quantum Field Theory, Cambridge University Press.

[56] E. A. Calzetta, The 2-particle irreducible effective action in gauge theories, Int. J. Theor. Phys. 43 (2004) 767–799.

[57] M. E. Carrington, E. Kovalchuk, QED electrical conductivity using the 2PI effective action, Phys. Rev. D76 (2007) 045019.

[58] M. E. Carrington, E. Kovalchuk, Leading Order QED Electrical Conductivity from the 3PI Effective Action, Phys. Rev. D77 (2008) 025015.

[59] S.-J. Chang, N. Weiss, Instability of constant Yang-Mills fields, Phys. Rev. D20 (1979) 869.

[60] M. Cheng, et al., The transition temperature in QCD, Phys. Rev. D74 (2006) 054507.

[61] M. Cheng, et al., The Spatial String Tension and Dimensional Reduction in QCD, Phys. Rev. D78 (2008) 034506.

[62] F. Cooper, J. F. Dawson, B. Mihaila, Dynamics of broken symmetry lambda phi**4 field theory, Phys. Rev. D67 (2003) 051901.

[63] F. Cooper, J. F. Dawson, B. Mihaila, Quantum dynamics of phase transitions in broken symmetry lambda phi**4 field theory, Phys. Rev. D67 (2003) 056003.

[64] F. Cooper, S. Habib, Y. Kluger, E. Mottola, Nonequilibrium dynamics of symmetry breaking in lambda Phi**4 field theory, Phys. Rev. D55 (1997) 6471–6503.

[65] F. Cooper, C.-W. Kao, G. C. Nayak, Infrared behaviour of the gluon propagator in non-equilibrium situations, Phys. Rev. D66 (2002) 114016.

[66] F. Cooper, A. Khare, H. Rose, Classical limit of time-dependent quantum field theory: A Schwinger-Dyson approach, Phys. Lett. B515 (2001) 463–469.

[67] F. Cooper, et al., Nonequilibrium quantum fields in the large N expansion, Phys. Rev. D50 (1994) 2848–2869.

[68] J. M. Cornwall, R. Jackiw, E. Tomboulis, Effective Action for Composite Operators, Phys. Rev. D10 (1974) 2428–2445.

[69] M. Creutz, Quarks, gluons and lattices, Cambridge University Press, 1984.

[70] A. Cucchieri, T. Mendes, Critical Slowing-Down in SU(2) Landau Gauge-Fixing Algorithms, Nucl. Phys. B471 (1996) 263–292.

[71] M. D'Attanasio, M. Pietroni, Gauge-invariant renormalization group at finite temperature, Nucl. Phys. B498 (1997) 443–466.

[72] A. Dumitru, Y. Nara, QCD plasma instabilities and isotropization, Phys. Lett. B621 (2005) 89–95.

[73] A. Dumitru, Y. Nara, M. Strickland, Ultraviolet avalanche in anisotropic non-Abelian plasmas, Phys. Rev. D75 (2007) 025016.

[74] H. Fujii, K. Itakura, An analytic study towards instabilities of the glasma, arXiv:0806.1840 [hep-ph].

[75] H. Fujii, K. Itakura, Expanding color flux tubes and instabilities, Nucl. Phys. A809 (2008) 88–109.

[76] H. Fujii, K. Itakura, A. Iwazaki, Instabilities in non-expanding glasma, Nucl. Phys. A828 (2009) 178–190.

[77] T. Furusawa, Onset of chaos in the classical SU(2) Yang-Mills theory, Nucl. Phys. B290 (1987) 469.

[78] T. Gasenzer, J. Berges, M. G. Schmidt, M. Seco, Non-perturbative dynamical many-body theory of a Bose- Einstein condensate, Phys. Rev. A72 (2005) 063604.

[79] T. Gasenzer, J. Berges, M. G. Schmidt, M. Seco, Ultracold atomic quantum gases far from equilibrium, Nucl. Phys. A785 (2007) 214–217.

[80] D. Gelfand, Nichtgleichgewichtsdynamik in der SU(3) Eichtheorie. Bachelor- Thesis, Technische Universität Darmstadt, 2008.

[81] A. Giraud, J. Serreau, Nonlinear dynamics of fermions during preheating, Nucl. Phys. A820 (2009) 215c–218c.

[82] D. Y. Grigoriev, V. A. Rubakov, M. E. Shaposhnikov, Sphaleron transitions at finite tempreatures: numerical study in (1+1)-dimensions, Phys. Lett. B216 (1989) 172–176.

[83] D. J. Gross, F. Wilczek, Ultraviolet behavior of non-Abelian gauge theories, Phys. Rev. Lett. 30 (1973) 1343–1346.

[84] M. Gyulassy, L. McLerran, New forms of QCD matter discovered at RHIC, Nucl. Phys. A750 (2005) 30–63.

[85] U. W. Heinz, Thermalization at RHIC, AIP Conf. Proc. 739 (2005) 163–180.

[86] U. W. Heinz, P. F. Kolb, Early thermalization at RHIC, Nucl. Phys. A702 (2002) 269–280.

[87] E. Iancu, R. Venugopalan, The color glass condensate and high energy scattering in QCD, hep-ph/0303204.

[88] C. Itzykson, J. B. Zuber, Quantum Field Theory, McGraw-Hill, 1980.

[89] J. D. Jackson, Classical Electrodynamics, 3rd edition, Wiley & Sons, 1998.

[90] L. P. Kadanoff, G. Baym, Quantum Statistical Mechanics, Addison-Wesley Publishing Company, 1962.

[91] F. Karsch, H. W. Wyld, Thermal Green's functions and transport coefficients on the lattice, Phys. Rev. D35 (1987) 2518.

[92] L. V. Keldysh, Diagram technique for nonequilibrium processes, Zh. Eksp. Teor. Fiz. 47 (1964) 1515–1527.

[93] J. B. Kogut, L. Susskind, Hamiltonian formulation of Wilson's lattice gauge theories, Phys. Rev. D11 (1975) 395.

[94] Y. V. Kovchegov, Can thermalization in heavy ion collisions be described by QCD diagrams?, Nucl. Phys. A762 (2005) 298–325.

[95] A. Kovner, L. D. McLerran, H. Weigert, Gluon production at high transverse momentum in the McLerran-Venugopalan model of nuclear structure functions, Phys. Rev. D52 (1995) 3809–3814.

[96] A. Kovner, L. D. McLerran, H. Weigert, Gluon production from nonAbelian Weizsacker-Williams fields in nucleus-nucleus collisions, Phys. Rev. D52 (1995) 6231–6237.

[97] A. Krasnitz, Thermalization algorithms for classical gauge theories, Nucl. Phys. B455 (1995) 320–338.

[98] R. Kubo, Statistical mechanical theory of irreversible processes. 1. General theory and simple applications in magnetic and conduction problems, J. Phys. Soc. Jap. 12 (1957) 570–586.

[99] M. Laine, G. D. Moore, O. Philipsen, M. Tassler, Heavy Quark Thermalization in Classical Lattice Gauge Theory: Lessons for Strongly-Coupled QCD, JHEP 05 (2009) 014.

[100] M. Laine, O. Philipsen, P. Romatschke, M. Tassler, Real-time static potential in hot QCD, JHEP 03 (2007) 054.

[101] M. Laine, O. Philipsen, M. Tassler, Thermal imaginary part of a real-time static potential from classical lattice gauge theory simulations, JHEP 09 (2007) 066.

[102] P. V. Landshoff, A. Rebhan, Covariant gauges at finite temperature, Nucl. Phys. B383 (1992) 607–621.

[103] T. Lappi, L. McLerran, Some features of the glasma, Nucl. Phys. A772 (2006) 200–212.

[104] M. Le Bellac, Thermal Field Theory, Cambridge University Press.

[105] A. D. Linde, Infrared Problem in Thermodynamics of the Yang-Mills Gas, Phys. Lett. B96 (1980) 289.

[106] M. Luzum, P. Romatschke, Conformal Relativistic Viscous Hydrodynamics: Applications to RHIC results at sqrt(sNN) = 200 GeV, Phys. Rev. C78 (2008) 034915.

[107] E. Manousakis, J. Polonyi, Nonperturbative length scale in high temperature qcd, Phys. Rev. Lett. 58 (1987) 847.

[108] P. C. Martin, J. S. Schwinger, Theory of many particle systems. I, Phys. Rev. 115 (1959) 1342–1373.

[109] P. C. Martin, E. D. Siggia, H. A. Rose, Statistical Dynamics of Classical Systems, Phys. Rev. A8 (1973) 423–437.

[110] T. Matsui, H. Satz, J/psi Suppression by Quark-Gluon Plasma Formation, Phys. Lett. B178 (1986) 416.

[111] L. D. McLerran, R. Venugopalan, Gluon distribution functions for very large nuclei at small transverse momentum, Phys. Rev. D49 (1994) 3352–3355.

[112] R. Micha, I. I. Tkachev, Relativistic turbulence: A long way from preheating to equilibrium, Phys. Rev. Lett. 90 (2003) 121301.

[113] R. Micha, I. I. Tkachev, Turbulent thermalization, Phys. Rev. D70 (2004) 043538.

[114] I. Montvay, G. Münster, Quantum fields on a lattice, Cambridge University Press, 1994.

[115] G. D. Moore, Improved Hamiltonian for Minkowski Yang-Mills theory, Nucl. Phys. B480 (1996) 689–728.

[116] G. D. Moore, Motion of Chern-Simons Number at High Temperatures under a Chemical Potential, Nucl. Phys. B480 (1996) 657–688.

[117] G. D. Moore, Real time simulations in lattice gauge theory, Nucl. Phys. Proc. Suppl. 83 (2000) 131–135.

[118] G. D. Moore, Problems with lattice methods for electroweak preheating, JHEP 11 (2001) 021.

[119] G. D. Moore, K. Rummukainen, Classical sphaleron rate on fine lattices, Phys. Rev. D61 (2000) 105008.

[120] S. Mrówczyński, Stream instabilities of the quark - gluon plasma, Phys. Lett. B214 (1988) 587.

[121] S. Mrówczyński, Plasma instability at the initial stage of ultrarelativistic heavy ion collisions, Phys. Lett. B314 (1993) 118–121.

[122] S. Mrówczyński, Color collective effects at the early stage of ultrarelativistic heavy ion collisions, Phys. Rev. C49 (1994) 2191–2197.

[123] S. Mrówczyński, Color filamentation in ultrarelativistic heavy-ion collisions, Phys. Lett. B393 (1997) 26–30.

[124] S. Mrówczyński, Instabilities driven equilibration at the early stage of nuclear collisions, Nucl. Phys. A774 (2006) 149–158.

[125] S. Mrówczyński, Instabilities driven equilibration of the quark-gluon plasma, Acta Phys. Polon. B37 (2006) 427–454.

[126] A. H. Mueller, A. I. Shoshi, S. M. H. Wong, On Kolmogorov wave turbulence in QCD, Nucl. Phys. B760 (2007) 145–165.

[127] B. Müller, A. Trayanov, Deterministic chaos in nonAbelian lattice gauge theory, Phys. Rev. Lett. 68 (1992) 3387–3390.

[128] H. B. Nielsen, H. H. Rugh, S. E. Rugh, Chaos and scaling in classical non-Abelian gauge fields, chao-dyn/9605013.

[129] N. K. Nielsen, P. Olesen, An Unstable Yang-Mills Field Mode, Nucl. Phys. B144 (1978) 376.

[130] M. E. Peskin, D. V. Schroeder, An Introduction to quantum field theory, Addison-Wesley, 1995.

[131] R. Phythian, The functional formalism of classical statistical dynamics, Journal of Physics A: Mathematical and General 10 (5) (1977) 777–789.

[132] H. D. Politzer, Reliable perturbative results for strong interactions?, Phys. Rev. Lett. 30 (1973) 1346–1349.

[133] W. Press, S. Teukolsky, W. Vetterling, B. Flannery, Numerical Recipes in C, 2nd ed., Cambridge University Press, Cambridge, UK, 1992.

[134] A. Rebhan, P. Romatschke, M. Strickland, Hard-loop dynamics of non-Abelian plasma instabilities, Phys. Rev. Lett. 94 (2005) 102303.

[135] U. Reinosa, J. Serreau, 2PI effective action for gauge theories: Renormalization, JHEP 07 (2006) 028.

[136] U. Reinosa, J. Serreau, Ward Identities for the 2PI effective action in QED, JHEP 11 (2007) 097.

[137] U. Reinosa, J. Serreau, 2PI functional techniques for abelian gauge theories, Nucl. Phys. A820 (2009) 139c–146c.

[138] U. Reinosa, J. Serreau, 2PI functional techniques for gauge theories: QED, arXiv:0906.2881 [hep-ph].

[139] P. Romatschke, New Developments in Relativistic Viscous Hydrodynamics, arXiv:0902.3663 [hep-ph].

[140] P. Romatschke, U. Romatschke, Viscosity Information from Relativistic Nuclear Collisions: How Perfect is the Fluid Observed at RHIC?, Phys. Rev. Lett. 99 (2007) 172301.

[141] P. Romatschke, M. Strickland, Collective modes of an anisotropic quark gluon plasma, Phys. Rev. D68 (2003) 036004.

[142] P. Romatschke, R. Venugopalan, The unstable Glasma, Phys. Rev. D74 (2006) 045011.

[143] S. Roth, Nicht-Abelsche Eichtheorien fern des thermischen Gleichgewichts. Diploma thesis, Technische Universität Darmstadt, 2008.

[144] H. J. Rothe, Lattice gauge theories: An Introduction, World Sci. Lect. Notes Phys. 74 (2005) 1–605.

[145] J. S. Schwinger, Brownian motion of a quantum oscillator, J. Math. Phys. 2 (1961) 407–432.

[146] D. Sexty, A. Patkos, Non-equilibrium Higgs transition in classical scalar electrodynamics, JHEP 10 (2005) 054.

[147] P. Sikivie, Instability of abelian field configurations in Yang-Mills theory, Phys. Rev. D20 (1979) 877.

[148] J.-I. Skullerud, J. Smit, A. Tranberg, W and Higgs particle distributions during electroweak tachyonic preheating, JHEP 08 (2003) 045.

[149] M. Strickland, Thermalization and the chromo-Weibel instability, J. Phys. G34 (2007) S429–436.

[150] A. Tranberg, 2PI simulations in expanding backgrounds: Doing it anyway!, Nucl. Phys. A820 (2009) 195c–198c.

[151] T. N. Tudron, Instability of constant Yang-Mills fields generated by constant gauge potentials, Phys. Rev. D22 (1980) 2566.

[152] M. van der Meulen, D. Sexty, J. Smit, A. Tranberg, Chern-Simons and winding number in a tachyonic electroweak transition, JHEP 02 (2006) 029.

[153] L. von Smekal, A. Jorkowski, D. Mehta, A. Sternbeck, Lattice Landau gauge via Stereographic Projection, PoS CONFINEMENT8 (2008) 048.

[154] E. S. Weibel, Spontaneously growing transverse waves in a plasma due to an anisotropic velocity distribution, Phys. Rev. Lett. 2 (3) (1959) 83–84.

[155] S. Weinberg, The quantum theory of fields. Vol. 2: Modern applications, Cambridge University Press, 1996.

[156] M. Wellner, Evidence for a Yang-Mills fractal, Phys. Rev. Lett. 68 (1992) 1811–1813.

[157] M. Wellner, The Road to fractals in a Yang-Mills system, Phys. Rev. E50 (1994) 780–789.

[158] Z. Xu, C. Greiner, Thermalization of gluons in ultrarelativistic heavy ion collisions by including three-body interactions in a parton cascade, Phys. Rev. C71 (2005) 064901.

[159] V. E. Zakharov, V. S. L'vov, G. Falkovich, Kolmogorov Spectra of Turbulence I, Springer, 1992.

Lebenslauf

Persönliche Angaben

Vorname:	Sebastian Herwig Jürgen
Nachname:	Scheffler
Geburtsdatum:	5. Juni 1980
Geburtsort:	Hamburg, Deutschland

Schulische und universitäre Ausbildung

1986 - 1987:	Besuch der Grundschule in Minden
1987 - 1990:	Besuch der Grundschule in Erftstadt-Lechenich
1990 - 1999:	Städtisches Gymnasium Erftstadt-Lechenich, Abitur Juni 1999
1999 - 2000:	Wehrdienst beim Fernmeldeaufklärungsregiment 940 in Daun
2000 - 2003:	Studium der Physik an der Universität zu Köln, Vordiplom September 2002
2002 - 2003:	Studium der Physik an der University of Edinburgh, Großbritannien
2003 - 2006:	Studium der Physik an der Universität Heidelberg, Diplom Mai 2006
seit 2006:	Wissenschaftlicher Mitarbeiter am Institut für Kernphysik der Technischen Universität Darmstadt

Veröffentlichungen:

1. J. Berges, S. Scheffler and D. Sexty, *"Bottom-up iostropisation in classical-statistical lattice gauge theory"*, Physical Review D **77** (2008), p. 034504, arXiv:0712.3514 [hep-ph].

2. S. Scheffler, R. Hofmann and I. O. Stamatescu, *"Scalar field theory with a non-standard potential"*, Physical Review D **77** (2008), p. 065015, arXiv:0712.3683 [hep-lat].

3. J. Berges, D. Gelfand, S. Scheffler and D. Sexty, *"Simulating plasma instabilities in SU(3) gauge theory"*, Physics Letters B **677** (2009), p. 210 - 213, arXiv:0812.3859 [hep-ph].

4. J. Berges, S. Scheffler and D. Sexty, *"Turbulence in nonabelian gauge theory"*, Physics Letters B **681** (2009), p. 362 - 366, arXiv:0811.4293 [hep-ph].

Eidesstattliche Erklärung

Hiermit erkläre ich eidesstattlich, dass ich die vorliegende Dissertation selbständig verfasst, keine anderen als die angegebenen Hilfsmittel verwendet und noch keinen Promotionsversuch unternommen habe.

Darmstadt, den 26. Januar 2010,

. . . . . gez. Sebastian Scheffler

Unterschrift